

**Micromechanical Mass Correlation Spectroscopy
for the Characterization of Nanoparticles and
Biomolecular Complexes in Fluid**

Dissertation
for the award of the degree
“Doctor of Philosophy”
Division of Mathematics and Natural Sciences

within the doctoral program
“Physics of Biological and Complex Systems”
of the Georg-August University School of Science (GAUSS)

submitted by
Mario Matteo Modena
from Pinerolo, Italy

Göttingen, 2015

Thesis Committee

Dr. Thomas P. Burg, *Biological Micro- and Nanotechnologies*, Max Planck Institute for Biophysical Chemistry

Prof. Jörg Enderlein, *III Institute of Physics*, Georg August University Göttingen

Prof. Bert de Groot, *Computational Biomolecular Dynamics*, Max Planck Institute for Biophysical Chemistry

Members of the Examination Board

Referee: Dr. Thomas P. Burg, *Biological Micro- and Nanotechnologies*, Max Planck Institute for Biophysical Chemistry

2nd Referee: Prof. Jörg Enderlein, *III Institute of Physics*, Georg August University Göttingen

Further Members of the Examination Board

Dr. Gopalakrishnan Balasubramanian, *Spin Imaging*, Max Planck Institute for Biophysical Chemistry

Prof. Bert de Groot, *Computational Biomolecular Dynamics*, Max Planck Institute for Biophysical Chemistry

Prof. Sarah Köster, *Institute for X-Ray Physics*, Georg August University Göttingen

Dr. Iwan A. T. Schaap, *III Institute of Physics*, Georg August University Göttingen

Abstract

Despite the wide range of techniques for the analysis of sub-micrometer objects, label-free characterization of nanoparticles in solution still remains a challenge. Micromechanical resonators with embedded fluidic channels have recently emerged as an enabling new technology for the mass characterization of suspended particles. However, technological limitations have prevented their application to particles and biomolecular complexes less than ~ 1 attogram (0.6 MDa) in mass.

In this thesis, correlation analysis of the time-domain mass signal is introduced as a novel method to extend the application of microfluidic resonators to samples in sub-MDa mass range. This method, called mass correlation spectroscopy (MCS), allows the detection of suspended particles even when their signatures in the time-trace cannot be individually recognized.

The analysis is formally derived and the limits of detection for resonators of different dimensions are discussed. It is shown that the resolution of the analysis is not limited by the measurement noise, and the signal-to-noise ratio can be improved by increasing particle concentration and acquisition time. Measurements on validated samples prove that resolution enhancement of over five orders of magnitude can be obtained in usual experimental conditions.

After derivation of an approximate model for the transport of particles in the embedded channel, particle size is inferred from the shape of the correlation curve, enabling the microfluidic resonators to detect mass, size and density of particles in solution in a single experiment. Limitations on the detection of samples composed of a heterogeneous population of particles are discussed.

Proof-of-principle application of the MCS method for the mass characterization of samples of biological interest is presented. The time course of amyloid formation is monitored from the early state of amorphous aggregates to mature fibrils by detecting the increase in average mass of the complexes in solution. As another application, the quantification of surface coatings of nanoparticles is discussed; the detection method is validated by measuring the adsorption of a protein monolayer on the surface of 400 nm polystyrene beads. Finally, proof-of-concept measurements of ribosomes are presented, proving that correlation analysis might find wide application in the characterization of biomolecular complexes in solution.

Acknowledgements

Firstly, I would like to express my sincere gratitude to Dr. Thomas Burg for giving me the opportunity to do my thesis research under his supervision. His guidance and enthusiasm have been a great source of motivation for pursuing this doctoral work throughout the years.

I would like to thank Prof. Bert de Groot and Prof. Jörg Enderlein for being part of my thesis committee, and for the fruitful discussions that occurred during our meetings. I would also like to thank Dr. Gopalakrishnan Balasubramanian, Prof. Sarah Köster and Dr. Iwan Schaap for agreeing to be members of my examination board.

I wish to thank Dr. Frank Peske and Prof. Wolfgang Wintermeyer for their interest in this work and its potential applications, and also for generously supporting it by providing the ribosome samples.

A special mention goes to my colleagues, Foelke Jürgens, Gianmarco Nocera, Hélène Foussard, Margherita Bassu, Rachel Lowe, Raffaele Faoro, Yara Mejia and Yu Wang, for creating both a stimulating and pleasant working environment. The combination of the different expertises in the lab, and the high-quality coffee, have often lead to inspiring discussions that have greatly facilitated the progresses of the project. Your input on the most disparate topics, ranging from setup improvements to road bikes, has been an immense help. In particular, I would like to thank Dr. Yara Mejia and Dr. Rachel Lowe for their patience in proof-reading parts of this thesis.

I would have never been able to gather all the necessary credits and fulfill all the requirements if it had not been for the help of the IMPRS-PBCS program coordinators Frauke Bergmann, Antje Erdmann and Tina Trost. Thank you for being always so kind and patient, regardless of the hundreds of questions I always had.

Additionally, this thesis would have been much more difficult without the help

of a sincere group of friends, both within the institute and outside. Their support, patience, and presence have been essential to my survival during these years. Working at the institute would have not been the same without so many friends creating a fun environment and always being a good excuse for taking a break. Thank you Aldo Alcaparra, Luis Fonseca, Michael Ratz, Mirko Lukovic, Raffaella Garofalo, Riccardo Belardinelli and Roberto Rizzato. A special thanks goes also to all those friends that traveled hundreds of kilometers just for a weekend (and a schnitzel) together: Antonio Vetrò, Diego Dupouy, Giovanna Lella, Matteo Cornaglia, Ombretta Cesca and Sergio Allegri from Lausanne, (Prof.) Ilaria Testa from Stockholm, Davide Giorcelli and Elena Berruto from Ciriè.

To conclude, I would like to express my gratitude to my family. Special thanks goes to my father Giulio, to my sister Chiara, and to my brothers Andrea and Paolo, for their love and for always encouraging me to pursue my dreams. Finally, I wish to thank my partner Alessandra. This thesis would have never been possible without her enduring support.

Contents

Abstract	III
Acknowledgements	v
1 Introduction	1
1.1 Scope of the thesis	3
1.2 Nanoparticle characterization techniques	4
2 Suspended Microchannel Resonators	13
2.1 Mass measurements with mechanical resonators	13
2.2 Suspended Microchannel Resonators	14
2.3 Experimental setup	15
2.3.1 Double-paddle cantilever SMR	19
2.3.2 50 μm SNR device	22
2.4 Detection modes	24
2.4.1 Mass accumulation	24
2.4.2 Flow-through mode	26
2.5 Experimental method	29
2.5.1 Mass measurements	29
2.5.2 Data analysis	30
2.5.3 Mass conversion calibration	33
3 Resolution enhancement of SMR	35
3.1 Mass Correlation Spectroscopy	36
3.1.1 MCS - definition	38

3.1.2	MCS - amplitude	40
3.2	Signal-to-noise ratio	43
3.3	Validation of the MCS method	45
3.3.1	SMR resolution enhancement	45
3.3.2	SNR resolution enhancement	46
4	Size characterization by MCS	49
4.1	Theory	49
4.1.1	Taylor regime	54
4.1.2	Advection regime	57
4.1.3	Concentration dispersion model	60
4.1.4	Effect of aspect ratio on MCS signal	61
4.2	Monte Carlo simulations	61
4.2.1	Method	62
4.2.2	Results	63
4.3	Experimental validation	64
4.3.1	Materials and methods	64
4.3.2	Monodisperse populations	67
4.3.3	Heterogeneous samples	72
5	Applications of the MCS method	75
5.1	Insulin aggregation kinetics	76
5.1.1	Protein aggregation	76
5.1.2	Mass characterization of insulin aggregates	79
5.1.3	Materials and methods	83
5.2	Quantification of bead protein coatings	85
5.2.1	Theoretical calculations	86
5.2.2	Quantification of surface coating of polystyrene beads	91
5.3	Label-free detection of ribosomes	95
5.3.1	Density characterization	95
5.3.2	Results and discussion	97
5.4	Flow velocity detection in SMR channel	101

6 Conclusions	107
Appendices	111
A Computer scripts	113
B List of scientific contributions	117
Bibliography	119
Curriculum Vitæ	133

List of Figures

2.1	Suspended Microchannel Resonator	14
2.2	SMR setup	16
2.3	Double-paddle resonator - dimensions and frequency response	19
2.4	Schematic and frequency response of the SNR cantilever resonator	22
2.5	Mass accumulation detection mode	25
2.6	Resonant mode and sensitivity profile	27
2.7	Linear approximation of the sensitivity profile	27
2.8	Single-particle frequency signature	29
2.9	Measurement procedure	30
2.10	Time-domain frequency measurement	31
2.11	Reference particle identification and separation	32
2.12	Quantification of single-particle induced frequency shift	33
2.13	SMR mass/frequency response calibration	34
2.14	SNR50 mass/frequency response calibration	34
3.1	Superposition of individual particle signatures	37
3.2	Mass Correlation Spectroscopy: concept	39
3.3	Compartment approximation of the velocity profile	43
3.4	Signal-to-noise ratio of the correlation analysis	44
3.5	Characterization of 85 nm polystyrene beads in SMR	45
3.6	Characterization of 43 nm polystyrene beads in SNR	47
4.1	MCS theoretical curves of finite-size particles	50
4.2	Assumptions for the derivation of particle dispersion model	54
4.3	Effective dispersion and velocity for finite-size particles	56

4.4	Taylor axial dispersion of finite-size particles	57
4.5	Velocity profile approximation as sum of Plane Couette flows	58
4.6	Sample axial dispersion in advection regime	59
4.7	Transition coefficient from the advection to the Taylor regime	61
4.8	Effect of channel aspect ratio on the autocorrelation of finite-size particles	62
4.9	Monte Carlo simulation of point-like particles	63
4.10	Autocorrelation analysis for size determination	65
4.11	Data treatment procedure for size analysis	66
4.12	Bootstrap analysis for uncertainty estimation	68
4.13	Fit of experimental autocorrelation curves	68
4.14	Buoyant mass and size of the particles measured by MCS. The manufacturer specifications are reported for comparison. Size estimations with the MCS method shows a deviation of approximately 25 nm from the manufacturer reported values, however relative size differences between particles can be detected by the analysis. The non monotonic behavior of the mass with particle size clearly shows that the samples under examinations where composed of different materials, with a large difference in density. Reprinted from Modena and Burg [21].	70
4.15	Heterogeneous sample autocorrelation	73
5.1	Protein aggregation pathway	77
5.2	ThT detection of amyloid formation	78
5.3	Aggregation kinetics of insulin protein detected by MCS	79
5.4	Comparison between average aggregate mass and ThT-intensity	80
5.5	Ultrasonication of amyloid fibrils	82
5.6	Bead concentration and detection range	88
5.7	Effective concentration of primary antibodies in solution	89
5.8	Bead assay detection range	91
5.9	Quantification of surface coating of suspended beads by BSA	93
5.10	Ribosome density characterization	97
5.11	Ribosome interactions with channel walls	99
5.12	Frequency shifts of reference beads in different density solutions	100

5.13 Label-free detection of fibril elongation	103
--	-----

List of Tables

1.1	Comparison of techniques for the characterization of nanoparticles . . .	12
2.2	SMR device dimensions	19
2.3	SNR device dimensions	22
5.1	Fibril length estimation from average mass values	83
5.2	Bead-based assay - List of symbols	87
5.3	Estimations of ribosome mass	98

Chapter 1

Introduction

The understanding of the composition and function of samples in the sub-micrometer scale, such as macromolecular complexes or synthetic nanoparticles, requires thorough characterization of their physical and chemical properties, and of their interactions with the environment. For this purpose, several techniques have been devised to analyze samples of interest in conditions that mimic the sample's native environment. Although optical characterization is limited by light diffraction, visual inspection can be obtained by using microscopy techniques with resolutions in the low tens of nanometers, such as electron microscopy [1], atomic force microscopy [2] and optical nanoscopy [3]. These techniques provide unique information on the shape and surface topology of the sample, however they are affected by various limitations, including low throughput, extensive sample preparation, and, often, insufficient spatial and temporal resolution for the study of reaction kinetics. Complementary methods have been developed for the measurement of reaction kinetics and for the detection of free particles in solution, not possible with high resolution microscopy techniques. As an example, assays based on fluorescence labeling are commonly used for the characterization of reaction kinetics. Fluorescence labeling enables high analysis specificity and sub-millisecond temporal resolution, and, furthermore, the technique can be used to characterize kinetics in several conditions, such as in free solutions or in cellular environments [4, 5, 6]. However, labeling can potentially interfere with the reaction of interest and label-free methods are used, when possible, to circumvent this limitation. Surface-based techniques such as surface plasmon resonance (SPR) and quartz crystal microbalance (QCM) are

commercial examples of label-free detection methods. Biomolecular interactions are measured by detecting variations of bound analyte on the sensor surface via refractive index measurements, or detection of mass deposition and surface stress [7, 8, 9]. These techniques enable real-time characterization of the reaction and high specificity, ensured by the functionalization of the sensor surface. However, the analysis is limited to surface bound samples and receptor immobilization can potentially affect the reaction, as discussed for the labeling strategy. To enable detection of samples in solutions, methods based on intensity measurements of light scattered by free particles in solution can be used. Scattered light intensity varies with particle size, mass and concentration, hence providing information on the physical properties of the sample [10, 11, 12]. The wide dynamic range (from \sim nanometer to \sim micrometer particles) and the detection in free solution allow these methods to be used for the characterization of molecular complexes and of their association, such as protein aggregation kinetics [13]. However, temporal resolution is limited by the acquisition time of the analysis, corresponding to few tens of seconds, and characterization of heterogeneous samples is strongly biased by the largest species in solution. Finally, the method can only be performed on optically clear solutions.

Recently, characterization of samples in solution by mass and density measurements has been demonstrated by using nanomechanical resonators with embedded microfluidic channels [14, 15, 16]. Similar to QCM measurements, these devices can be used for quantifying the amount of analyte binding to the functionalized surface of the embedded channel, using only microliters of sample and with high efficiency, as a consequence of the high surface to volume ratio of the embedded channel [14, 17, 18]. Furthermore, detection of free particles in solution is possible, and mass measurements with resolution approaching the attogram (\sim MDa) level have already been shown [19, 20, 21]. Characterization of biomolecular interactions is obtained by detecting mass and density variations of the particles in solution, without interfering with their conditions. Finally, the use of a microfluidic platform also provides the possibility of modifying sampling conditions *in situ*, enabling kinetic studies with minimum lag time.

1.1 Scope of the thesis

Despite the wide range of techniques for the analysis of sub-micrometer objects, the characterization of mass and size of particles in solution still remains a challenge. Nanomechanical resonators with embedded microfluidic channels enable the mass and density measurement of free particles in solution with minimum sample preparation and with a label-free approach. Currently, these devices have mostly found application in the characterization of cell samples [22, 23, 24]. Although devices with higher sensitivity have already been presented [16, 20], complications in operating them due to the small device dimensions and the relatively narrow detection ranges have so far precluded their wide use for the analysis of nanoparticles and biomolecular complexes.

Here, a novel method of analysis of the time-domain mass signal recorded by embedded channel resonators is presented. This method, called mass correlation spectroscopy (MCS), allows the detection of suspended particles with buoyant masses of more than five orders of magnitude below the single-particle detection limit. Resolution enhancement is obtained by using correlation analysis of the mass trace. This enables an increase of the sample contributions in the signal with respect to the background noise, even when particle signatures cannot be individually detected. The analysis does not require any modification of the devices and, therefore, can be used to extend their application to previously inaccessible fields, namely nanometer/sub-micrometer biological samples. Finally, the analysis of the MCS signal also provides information on the size of the particles, enabling the embedded channel resonators to provide characterization of mass, density and size.

Thesis outline

Firstly, current methods for the detection and characterization of nanoparticles in the 1-1000 nm range will be presented for comparison. Then, in Chapter 2, the embedded channel resonator devices will be introduced, with a focus on the current detection modes and limits of resolution. Following, in Chapter 3, the MCS analysis will be formally derived. The calculations will be carried out for a particular

class of nanomechanical resonator devices, namely the suspended microchannel resonators. Experimental proofs of the mass resolution enhancement are shown on synthetic nanoparticles. Subsequently, in Chapter 4, a detection method to infer particle size by MCS analysis will be described. Validation of the method by Monte Carlo simulations and experimental measurements are presented. In Chapter 5, samples of biological interest are analyzed with the MCS method. Four examples of application are presented: first, amyloid aggregation of insulin protein is detected by measuring the increase in average mass of the aggregates; then, adsorption of protein on the surface of nanoparticles in solution is quantified; as another application, the density of ribosomes is estimated, by detecting the change in buoyant mass as a function of the density of the suspending solution; at last, correlation analysis is used as a tool to estimate the mass transport of analytes in the embedded channel during surface-based measurements.

1.2 Nanoparticle characterization techniques

A brief overview of the main analysis methods currently used for the characterization of sub-micrometer particles is reported. This overview focuses on methods to measure mass or size of nanoparticles, with particular interest on techniques that can be performed on samples in solution. A summary table is shown on page 12 for a rapid comparison of the application ranges and main limitations of the available methods.

Transmission electron microscopy

Transmission electron microscopy (TEM) produces images of ultrathin (below 1000 nm) samples by detecting the transmitted intensity of an electron beam through the sample of interest [25]. The image obtained from the spatial intensity variations of the beam corresponds to a projection of the sample onto the detector plane. Interacting with the specimen, electrons might undergo large-angle scattering or energy loss, which cause local reductions in beam intensity. For this reason, image contrast is usually interpreted as representative of sample “mass thickness” [1]. To avoid scattering of the electron beam before interacting with the sample, electron microscopy is operated in high-vacuum. Therefore, samples must withstand these working conditions to allow imaging.

Extensive sample preparation is usually required when dealing with biological samples. Common sample preparation techniques are negative staining by heavy metal salt solutions (e.g. uranyl acetate), chemical fixation or rapid freezing of the sample, either followed by freeze-substitution to allow subsequent room-temperature characterization or by imaging at cryo temperatures [25]. Although TEM enables visual inspection of single-particles with nanometer resolution [26], the complex sample preparation and the low throughput of the analysis render this technique extremely labor intensive [27]. Furthermore, great care has to be taken during sample preparation, as the fixation and staining steps might cause sample alteration [25].

Analytical ultracentrifugation

Analytical ultracentrifugation (AUC) is often used as gold standard in particle size determination. The instrument essentially consists of a high-speed centrifuge and a detection system to measure the gradient of the sample concentration during centrifugation [28]. The concentration gradient along the centrifuge cell is measured by optical methods, such as absorbance, refractive index detection or, for fluorescent samples, fluorescence intensity [29]. AUC characterization can be performed in two main analysis modes: sedimentation velocity and sedimentation equilibrium. Sedimentation velocity detects the temporal evolution of the sample concentration distribution, providing hydrodynamic information, such as particle size and shape [29, 30]. Samples of different sizes sediment at different velocities and multi-modal sample distributions can be separated and identified. In contrast, sedimentation equilibrium detects the final thermodynamic concentration distribution. The sample reaches an equilibrium concentration gradient in the analysis cell, given by the opposing effects of centrifugal force and particle diffusion. The equilibrium concentration gradient can be used to detect molecular weight or, in the case of interacting samples, stoichiometry of the reaction, association energy and binding affinity [28, 29]. In addition to the high resolving power of AUC, the analysis has the advantage of being performed in solution and in label-free mode. The dynamic range can be adjusted by properly selecting rotor speed and it can be used to characterize samples of molecular weight ranging from 100 g/mol to 10^8 g/mol [31]. However, data interpretation and experimental procedures are complex, as several experimental factors, such as sample concentration or electrostatic interactions,

affects the sedimentation velocity or the final concentration gradient [30]. Furthermore, the technique requires long analysis time (hours) and expensive instrumentation [28]. For these reasons, AUC is used for the characterization of calibration samples, although interest for applications on biological samples is increasing [30].

Static light scattering

Static light scattering techniques measure the time-averaged intensity of light scattered by a sample of suspended particles at various angles θ [11]. According to the position of the detector with respect to the incident light, different types of techniques can be differentiated [32]. The most versatile technique is multi-angle light scattering (MALS): the intensity of the scattered light is measured at various angles to extrapolate the 0 degree intercept, which cannot be detected directly because of the overwhelming intensity of the transmitted beam. From the derivative of the light intensity for $\theta \rightarrow 0$ and the extrapolated 0 degree scattered intensity, MALS can be used to measure the radius of gyration and the molecular weight of particles in solution [12]. The radius of gyration (R_g) is a measure of the mass distribution of the particle around its center of mass, and it corresponds to its root mean square radius [33]. MALS is usually combined with separation/fractionation techniques so that precise characterization of monodisperse samples is obtained. However, in case of heterogeneous samples, the analysis returns the weighted average values of mass and size of the particles in solution [12].

MALS characterization is usually performed on samples ranging from ~ 20 to ~ 500 nm; as the size of the particles becomes comparable to the incident wavelength, particular care has to be taken in interpreting the data as fit models might not be applicable [12]. Furthermore, the effect of sample concentration on the refractive index of the solution has to be known for the analysis to return correct characterization values. This is usually obtained by working with very dilute samples or measuring, when possible, the variation of refractive index with concentration [12].

Dynamic Light Scattering

Dynamic light scattering (DLS) determines the diffusion coefficient of suspended particles. The measurement is obtained by looking at the time fluctuations of scattered

light caused by the random Brownian motion of particles in solution. By use of the Stokes-Einstein equation, the hydrodynamic radius (R_h) of the particles can be calculated from the diffusion coefficient [10]. R_h corresponds to the radius of an object with equal diffusivity in the suspending solution, hence can be relatively different from the actual particle size for elongated objects. DLS has a very wide dynamic range, extending from particles of sub-nanometer size to $\sim 1 - 10 \mu\text{m}$. Measurements can be performed in any optically clear buffer and sample volumes as low as $\sim 10 - 20 \mu\text{L}$ are necessary for detection [34]. DLS is an ensemble-based technique, therefore providing average size information for polydisperse samples. To mitigate this limitation, the analysis can be performed after sample separation or population distribution can be estimated by use of data fitting algorithms [35, 36, 37, 38]. As a consequence of the light intensity dependence on the sixth power of the particle diameter, large particles in solution strongly dominates the signal intensity, even at very low concentrations. For wide size distributions, overestimation of the average size of the particles is likely to occur [27].

Atomic Force Microscopy

Atomic force microscopy (AFM) can be used to visually inspect the shape of particles of interest at nanometer resolution, and to characterize their surface topology [2, 39]. However, unlike electron microscopy, AFM can be operated in liquid environments, reducing the possibility of alterations caused by sample preparation and providing real-time characterization of sample interactions [40, 41]. Furthermore, AFM can also be used to apply direct force stimulation to the sample and subsequently measure its response [40]. Despite these unique features, sample alteration might still occur, as free particles in solution cannot be characterized and immobilization on a surface is required for the detection [39]. As a single-particle characterization technique, AFM can be used to obtain very precise information on sample size distribution. However, the technique presents a relatively low throughput. Therefore, obtaining a statistical representation of the sample might be extremely labor intensive.

Fluorescence Correlation Spectroscopy

Fluorescence Correlation Spectroscopy (FCS) is a fluorescence-based technique that can provide characterization of reaction kinetics, and of the diffusion coefficients and concentrations of the samples under examination [42]. Similar to DLS, FCS measures spontaneous concentration fluctuations in the detection volume, manifesting as fluorescence intensity fluctuations. The use of fluorescence intensity for detection present numerous advantages with respect to scattered light. First, fluorescence labeling allows high-specificity characterization, even for heterogeneous samples. Furthermore, a confocal approach or a two-photon excitation scheme can be used to enhance the sensitivity of the measurement and suppress background noise [43, 44]. Another key difference with respect to DLS is that detection of diffusion coefficients is not limited to molecules in free solutions. Sample diffusion in different environments, such as in cells or lipid membranes, can also be measured [45, 46]. Finally, the flexibility given by the fluorescent labeling can be used to realize a wide variety of correlation experiments, such as multi-color [47] or dual-focus fluorescence cross correlation spectroscopy [6].

Nanoparticle Tracking Analysis

Nanoparticle tracking analysis (NTA) measures the free diffusion of particles in solution and, via the Stokes-Einstein relation, estimates their hydrodynamic radius. On the contrary to DLS, NTA relies on the analysis of single-particle trajectories, acquired by high temporal resolution videos in enhanced contrast microscopy [48]. Particles ranging between 30 nm to 1 μm can be detected, with a detection limit depending on the particle refractive index (for protein samples, the actual detection limit is 40-50 nm) [49]. Although NTA presents a narrower detection range compared to DLS, the ability of tracking single particles reduces the influence of large objects in solution and improves the detection of multimodal population distributions. NTA requires higher sample volumes ($\sim 300 \mu\text{L}$) than DLS and estimation bias is possible as a consequence of the contrast imaging conditions selected by the user during acquisition [49].

Tunable resistive pulse sensor

Tunable resistive pulse sensors (TRPS) measure the increase in electric resistance caused by the passage of a particle through a pore filled with a conductive fluid. TRPS

differs from conventional resistive pulse measurements, known as Coulter counters, in that the pore is realized in an elastomeric membrane, where pore size can be adjusted by stretching of the membrane [50, 51]. Adjustment of the pore size increases the dynamic range of the TRPS, allowing detection of particles ranging from ~ 50 nm to micrometer size [52]. By measuring the relative changes in electric resistance caused by the passage of the particles through the pore, particle size and surface charge can be estimated by use of theoretical models [53]. Detection of the sample distribution is enabled by the single-particle approach of the measurement technique. However, particular care has to be taken in sample preparation to avoid pore blockage during measurement and to avoid unwanted sample aggregation, as salt concentrations in the ~ 100 mM range are required for detection [52].

Embedded channel resonators

These devices will be presented in details in the next chapter, however a short introduction is reported here for comparison with the other detection techniques.

Nanomechanical resonators with embedded microfluidic channels enable the characterization of buoyant mass and density of particles in solution [14, 15]. Buoyant mass defines the difference in mass between the particle and the suspending solution, considering equal volumes. Particles flowing through the embedded microfluidic channel induce variations to the effective mass of the resonator, causing a shift in the resonance frequency of the device. The magnitude of this shift depends on the ratio between the induced mass variation and the resonator effective mass [14]. Therefore, the limit of detection is intrinsically linked to the resolution in the measurement of the resonance frequency and to the effective mass of the resonator: single-particle attogram resolution ($1 \text{ ag} = 10^{-18} \text{ g}$) has been demonstrated for devices with channels of cross-section dimensions of $0.4 \times 1 \mu\text{m}^2$ [20]. For comparison, a buoyant mass of 1 ag corresponds, approximately, to a protein aggregate of 20 nm in diameter or a polystyrene bead of 30 nm. Cross-section dimensions directly limit the detection range of the devices, posing an upper boundary to the size of samples that can be characterized without clogging the microfluidic embedded channel. These devices have typical mass detection ranges of ~ 2 -3 orders of magnitude.

Size Exclusion Chromatography

Size exclusion chromatography (SEC) is a technique for separating biomolecules by hydrodynamic radius differences. The main components are identified in the instrument: a stationary phase, composed of a porous material packed into a container (separation column) presenting a fluid inlet and outlet, and the sample mobile phase [54]. Separation is obtained by driving the mobile phase through the stationary phase by pressure or gravity. While flowing, molecules diffuse through the stationary phase and the extent of diffusion is controlled by the pore size and geometry. As large molecules are excluded from the pores, they elute first from the separation column, while smaller particles elute at later times [55]. To determine molecular weight, calibration samples can be used to estimate the elution times for different size molecules [54]. However, this method is prone to errors: samples might have similar molecular weights but different sizes or interact with the stationary phase, hence eluting at different times. To overcome these problems, SEC is usually combined with detectors able to independently characterize the eluted sample fractions, avoiding the use of calibration curves. Common characterization methods include, but are not limited to, UV-absorbance, light scattering methods and mass spectrometry [56].

SEC presents a very high resolving power in the separation of proteins and is routinely used for sample preparation and purification. However, it usually presents a narrow separation range (few tens of nm) dependent on the stationary phase employed and it can cause dilution of the sample in the elution separation. Furthermore, high pressures (~ 100 -500 bars) are sometimes required for driving the solution through micrometer pore size matrices and care has to be taken to avoid shear degradation of the sample [54].

Mass spectrometry

Initially developed for the study of chemical compounds, mass spectrometry (MS) has become a wide spread technique in proteomics [57]. The introduction of soft-ionization techniques, namely matrix-assisted laser desorption ionization (MALDI) and electrospray ionization (ESI), has allowed mass characterization of peptides and proteins

without causing degradation in the ionization process [58]. Recently, intact macromolecular complexes with molecular weights up to ~ 20 MDa could be analyzed by MS [59, 60]. Besides mass detection of individual analytes, MS also provides information on sample composition. Ligand binding and stoichiometry of reactions can be detected by MS in the presence of interacting samples [61]. The analysis is performed in gas phase, and great care has to be taken into the conversion of the sample from the solid/liquid state into the ionized gas condition. Furthermore, the ionization and the analysis of high molecular weight complexes remains challenging [61]. MS also finds application in the characterization of nanoparticles, however limited to the detection of elemental composition [62].

Technique	Characterization	Detection range	Advantages	Limitations
Analytical ultracentrifugation	Mass and size characterization	< 1 nm to $\sim \mu\text{m}$	High resolving power; label-free; in solution	Long analysis time, complex experiment
Atomic force microscopy	Surface topology of the sample	$\sim \text{nm}$ to μm	Visual inspection of the sample	Sample on a surface, low throughput
Dynamic light scattering	Hydrodynamic radius of the sample	< 1 nm to $\sim \mu\text{m}$	Label-free, in solution, integration after fractionation	Ensemble measurement; large particles dominate the signal
Embedded channel resonators	Buoyant mass and density	$\sim \text{ag}$ (MDa) to fg	Label free, in solution	Dynamic range is limited by the channel dimensions and device sensitivity
Fluorescence correlation spectroscopy	Hydrodynamic radius, sample diffusion, reaction kinetics	nm to μm	Sample diffusion not limited to free solution, high specificity	Labeling-based technique, low sample concentration
Mass spectrometry	Mass/charge ratio, stoichiometry	Da to MDa	High resolution, sample composition	Ionization of the sample, measurement in gas phase
Nanoparticle tracking analysis	Hydrodynamic radius	40 nm to μm	Single-particle detection	High sample volume (300 μL), possible user bias
Size exclusion chromatography	Separates particles by hydrodynamic radius	< 1 nm to ~ 100 nm	Very high separation power	Need of orthogonal methods for size/mass detection
Static light scattering	Radius of gyration and molecular weight	~ 20 to ~ 500 nm	In solution, label-free, easy integration after fractionation	Dilute samples, requires knowledge of refractive index changes to the solutions
Transmission electron microscopy	2D projection of the sample	nm to μm	Very high resolution, visual inspection of sample shape	Vacuum environment, need of extensive sample preparation
Tunable resistive pulse sensor	Particle size, surface charge	50 nm to μm	In solution, label-free, single-particle	Electrolyte solutions, possible pore blockage

Table 1.1: Comparison of techniques for the characterization of nanoparticles

Chapter 2

Suspended Microchannel Resonators

2.1 Mass measurements with mechanical resonators

Nanomechanical resonators have found a number of applications in the field of mass characterization, due to the high resolution attainable for samples in both vacuum and liquid environments [63, 14, 64, 65, 19, 20, 21]. The detection method is based on the relation between the resonator effective mass and resonance frequency, and mass measurements are obtained by quantifying the variations in the oscillation frequency upon interaction with the sample of interest. Therefore, mass resolution is intimately linked to the sharpness of the resonance frequency [66], represented by the device quality factor Q

$$Q = \frac{f_0}{\Delta f_0} \quad (2.1)$$

where f_0 defines the resonance frequency and Δf_0 the full width at half maximum of the resonance peak. Devices operated in a low-pressure atmosphere can have Q -factors exceeding 10^5 [67], while resonators operated in liquid environments usually have Q -values below ~ 100 due to high viscous damping, presenting low mass resolution for samples in solution. To overcome this limitation, resonators with an embedded fluidic channel were developed [68]. These devices have enabled measurements of samples

in solution using resonators with Q-factors of $\sim 10^4$, as the oscillation occurs in a low-pressure environment [14]. Different designs have been proposed for the embedded microfluidic resonators [14, 15, 17]; however, cantilever resonators, named suspended microchannel resonators (SMRs), are by far the most used class of devices [14, 16, 20, 22, 23, 24].

2.2 Suspended Microchannel Resonators

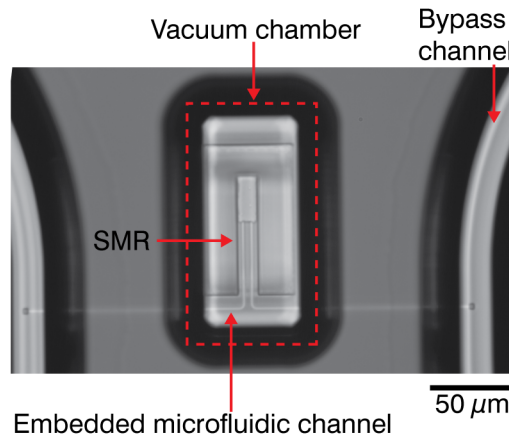


Figure 2.1: A suspended microchannel resonator of $75 \mu\text{m}$ length and $10 \mu\text{m}$ width. The cantilever is contained in a vacuum chamber to reduce damping. Due to the thin silicon layer (300 nm), the embedded microfluidic channel is visible in the picture. Bypass channels of $\sim 50 \mu\text{m}$ dimensions, on the left and right side, are used for rapid fluid delivery and exchange in the chip.

Suspended microchannel resonators are micromechanical resonators with a microfluidic channel embedded in the oscillating structure. The shape of the SMRs is that of a cantilever beam, containing a U-shaped channel where the sample of interest is introduced. This design allows the resonator to vibrate in a vacuum environment, while being sensitive to fluid density and suspended particles (Fig. 2.1).

The resonance frequency of the SMR is dependent on the effective mass m^* of the cantilever, which comprises both the silicon structure and the fluid in the embedded channel. Introducing particles with density different from that of the suspending fluid changes the effective mass of the resonator, causing a variation in the resonance

frequency of the device. The resonance f varies according to [14]

$$f = \frac{1}{2\pi} \sqrt{\frac{k}{m^* + \alpha \Delta m_p}} \quad (2.2)$$

where k is the resonator spring constant and α is a parameter that depends on the particle position. For a particle at the tip of the cantilever, $\alpha \approx 1$, while for uniformly distributed samples, such as liquid solutions or particles adsorbed on the channel walls, $\alpha \approx 0.24$. Δm_p denotes the buoyant mass of the particle, and it is defined as

$$\Delta m_p = m_p \left(1 - \frac{\rho_b}{\rho_p} \right) \quad (2.3)$$

with m_p the dry mass of the particle, ρ_p and ρ_b the particle and buffer densities. Assuming $\Delta m_p/m^* \ll 1$, Eq. 2.2 can be approximated as:

$$f \approx f_0 - \frac{1}{2} \frac{\alpha \Delta m_p}{m^*} f_0 \quad (2.4)$$

where f_0 is the resonance frequency when the device is filled with pure buffer.

Mass characterization of suspended objects by SMR can be obtained in two modes: analyte accumulation on the channel walls, which causes static shifts in resonance frequency, or detection of particles flowing through the resonator, which induce transient shifts in resonance frequency. These modes are presented in section 2.4.

2.3 Experimental setup

The SMR setup is composed of three main parts, namely the resonator, the electronic circuits for excitation and detection, and the fluidic system (Fig. 2.2).

Cantilever resonator

The cantilever is made of silicon and sealed between two pyrex wafers to create a vacuum environment for oscillation. Device vibration is achieved by electrostatic actuation, obtained with an electrode deposited below the resonator. To ensure temperature stability during measurement and reduce resonance frequency variations caused

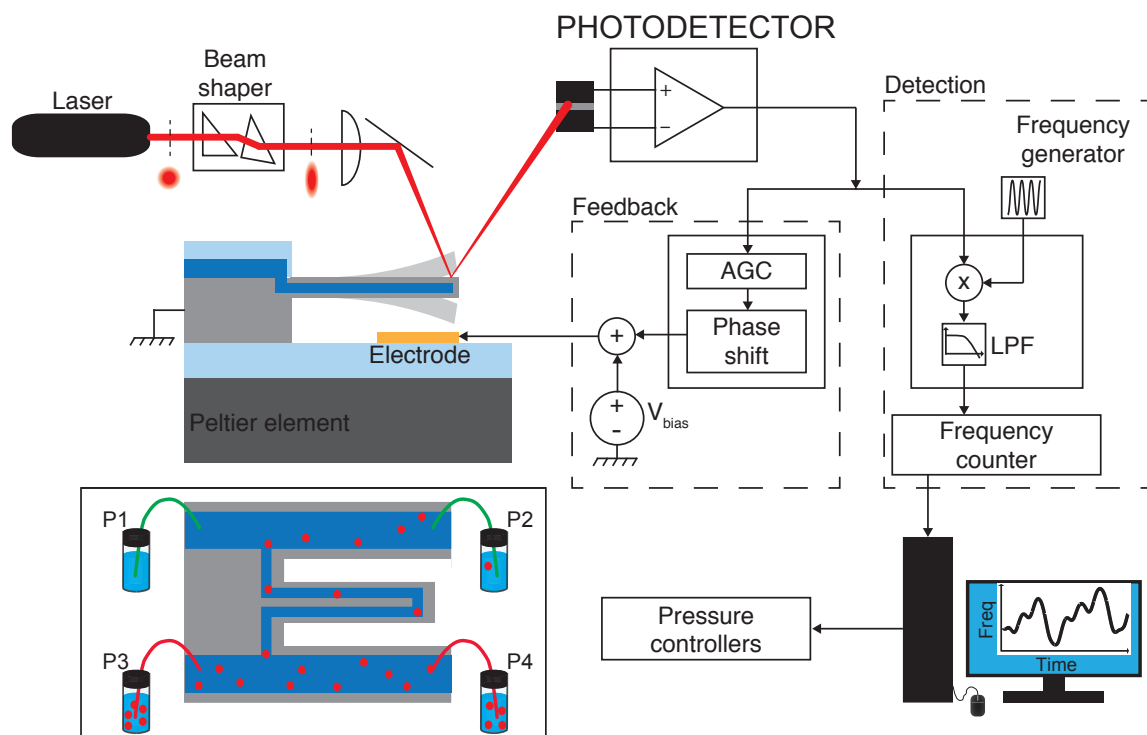
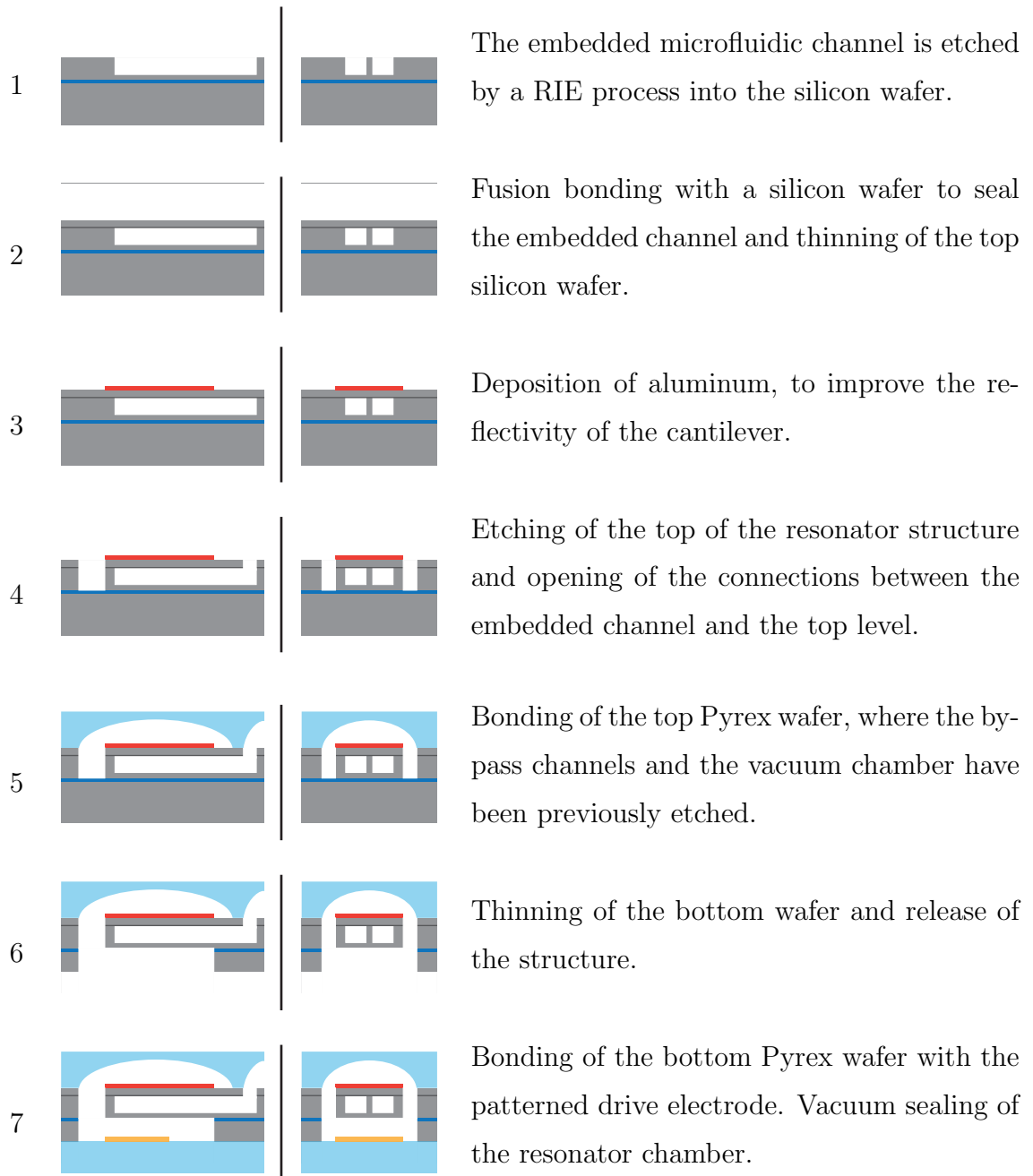


Figure 2.2: Schematic of the SMR setup. Detection of the resonator oscillation is obtained with an optical lever, impinging on a split photodiode. The converted electric signal is then amplified and phase shifted. After adding a bias voltage, the electric signal is applied to the drive electrode for electrostatic actuation. Resonance frequency variations are measured using a heterodyne detection method, to record only low frequency variations of the resonance frequency. In the inset, the fluidic component of the SMR device is depicted. The chip features two bypass channels for rapid delivery of the solutions to the embedded microfluidic channel. Computer controlled pressurized inlets and outlets allow fine tuning of the flow rates in the device.

by thermal drifts, the device is positioned on a Peltier element [69].

Fabrication

The SMR devices used in this work were fabricated at Innovative Micro Technology (Santa Barbara, CA) and generously provided by the laboratory of Prof. Scott Manalis (MIT, Cambridge, MA). Detailed information on the device fabrication can be found in Burg *et al.* [14]. The main steps are summarized here:



Oscillation detection

The detection of the cantilever oscillation is achieved by an optical lever method. A laser beam is focused on the cantilever tip and the displacement of the reflected beam is used to detect the motion of the resonator. The beam is shaped as an ellipsoid, as this configuration helps in the positioning of the laser spot along the main dimension

of the resonator. A split photodiode then converts the beam oscillation into an electric signal that is subsequently amplified and phase shifted, before feeding it back to the drive electrode. This generates a feedback loop that maintains the cantilever oscillating at its resonance frequency. An automatic gain control (AGC) circuit is also present to ensure a constant amplitude oscillation of the cantilever.

The resonance frequency of the device is measured by a heterodyne detection scheme. The oscillating electric signal coming from the photodiode is multiplied with a reference signal, with oscillating frequency $f_R = (f_0 - f_s)$, where f_0 is the resonance frequency of the device and f_s corresponds to the sampling rate of the acquisition. This gives rise to a signal presenting two frequency components: $f_0 + f_R$ and $f_0 - f_R$. By using a lowpass filter, the lower frequency beat is selected and the period of oscillation is measured. For further information, a detailed description of the feedback circuit is presented in [69].

Fluid control and delivery

The fluidic component of the SMR consists of two “wide” ($\sim 50 \mu\text{m}$) bypass channels etched in the top Pyrex wafer for rapid fluid delivery to the microfluidic channel embedded in the resonator (see inset in Fig. 2.2). By controlling the pressure at the inlets and outlets of the bypass channels, the flow in the detection channel can be tuned with high precision. The use of computer controlled pressure controllers provides good repeatability of flow rates between experiments and ensures a smooth pulse-free flow. Only FEP tubing directly fitted to the silicon/glass SMR chip are used to avoid adsorption of the sample to the external fluidics and to ensure high chemical resistance.

2.3.1 Double-paddle cantilever SMR

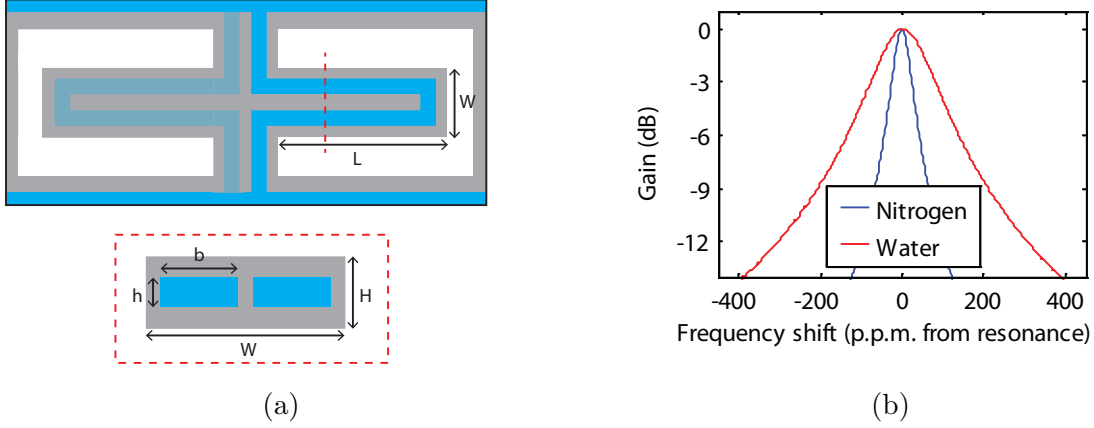


Figure 2.3: a) Schematic of the double-paddle SMR used for mass measurements (on top) and a cross-section of the device (bottom). The dimensions are reported in Table 2.2; b) frequency response of the SMR when filled with nitrogen gas ($f_{0d} \sim 1.33$ MHz, $Q_d \sim 22000$) and with milli-Q water ($f_{0w} \sim 1.26$ MHz, $Q_w \sim 6300$). Viscous damping causes a reduction in quality factor, as it can be observed by the widening of the resonance peak.

Device	$L[\mu\text{m}]$	$W[\mu\text{m}]$	$H[\mu\text{m}]$	$b[\mu\text{m}]$	$h[\mu\text{m}]$	$f_{0d}[\text{MHz}]$	Q_d	$f_{0w}[\text{MHz}]$	Q_w
SMR	60	36	7	8	3	1.33	22,000	1.26	6300

Table 2.2: Dimensions of the SMR device used for mass measurements of suspended particles. The symbols refer to Fig. 2.3a. The subscripts d and w refer to the device dry and filled with water, respectively.

The SMR is a double-paddle resonator made of silicon and containing an embedded microfluidic channel of $3 \times 8 \mu\text{m}^2$ (height \times width) cross-section dimensions in each of the cantilevers (Fig. 2.3a). Each side of the double-paddle resonators consists of a free standing beam measuring $60 \mu\text{m}$ in length, $36 \mu\text{m}$ in width and $7 \mu\text{m}$ in thickness (nominal dimensions from mask design and manufacturing parameters). When vibrating in the first resonant mode, the two cantilevers oscillate at the same frequency and with opposite deflection (i.e. with a phase difference of π). The device has a resonance frequency of ~ 1.3 MHz and quality factor Q of ~ 20000 when operated dry. Upon filling with water, the resonance frequency drops by ~ 0.1 MHz as a result of the added water mass (~ 10 ng). Furthermore, the quality factor of the devices is reduced to a Q value of ~ 6000 due to the viscous damping of the liquid inside the embedded channel

[70] (Fig. 2.3b). Small variations in resonance values are expected between devices because of small dimensional differences among the resonators, caused by manufacturing tolerances. Device oscillation is obtained with electrostatic actuation by two electrodes positioned on the bottom pyrex wafer, below the cantilevers. The electrodes have a bias voltage of ~ 100 V, while the AC signal has a 5 V amplitude peak-to-peak.

Mass resolution

The SMR devices used here have mass responsivities of ~ 20 mHz/fg ($1 \text{ fg} = 10^{-15} \text{ g}$) and typical readout noise is 0.2 Hz at a 1 kHz sampling rate. This value can be compared to the thermomechanical noise of the resonator, calculated as [71]

$$\frac{\delta f_{th}}{f_0} \approx \frac{\sqrt{S_x B_w}}{2Q\Delta z} \quad (2.5)$$

where B_w is the acquisition bandwidth, S_x the noise spectral density, Δz the cantilever deflection, f_0 the resonance frequency and δf_{th} the resulting frequency uncertainty. Firstly, the cantilever deflection is calculated from the resonator spring constant and the force exerted by the electrostatic actuation. To estimate it, the resonator/electrode structure can be approximated as a parallel plate capacitor, so that the force on each plate can be readily calculated as [71]

$$F = \epsilon_0 \frac{V_{act}^2 A}{2d^2} \quad (2.6)$$

where ϵ_0 is the dielectric constant of vacuum, $A \sim 2500 \mu\text{m}^2$ the electrode/resonator capacitor area, $d \sim 50 \mu\text{m}$ the distance between the two plates and $V_{act} = V_{bias} + V_{osc}$ the actuation voltage. However, V_{bias}^2 produces a static force on the cantilever and does not contribute to the oscillation excitation, therefore it is neglected here; only $V_{act}^2 = V_{osc}^2 + 2V_{osc}V_{bias} \approx 1000 \text{ V}^2$ is considered for the estimation. The calculation returns a force of 4 nN that, considering a spring constant $K \sim 30 \text{ N/m}$ [71] and a Q-factor ~ 6000 , causes a displacement $\Delta z \sim 800 \text{ nm}$ at resonance frequency. Then, the power spectral density of the thermomechanical noise can be calculated [71]

$$S_x \approx \frac{4k_B T Q}{2\pi f_0 K} \quad (2.7)$$

with k_B denoting the Boltzmann constant and T the temperature. It is now possible to estimate the vibration displacement uncertainty caused by the thermomechanical noise using Eq. 2.5, obtaining an estimation of the thermomechanical noise of 2 ppb (part per billion). This value is about two orders of magnitude smaller than the experimental acquisition noise. Although the frequency readout noise can be lowered by reducing the signal bandwidth, the thermomechanical noise level cannot be reached as thermal and mechanical drifts, as well as noise introduced by the excitation/detection scheme, ultimately limit the acquisition resolution.

Limit of detection

According to the readout frequency noise and requiring a signal-to-noise ratio of 3 to be able to detect single-particle events, the mass detection limit results in ~ 30 fg at 1 kHz sampling frequency. Reducing the signal acquisition rate effectively increases the resolution at the expense of lowering the throughput of the flow-through measurements: a sufficient number of points has to be acquired to monitor the particle flowing through the resonator, hence posing a limit on the maximum applicable flow rates. Considering a minimum of 20 points per particle needed for proper detection, measuring in a 1 Hz bandwidth would limit the even count to a maximum of ~ 2 particles per minute, and a flow velocity of $\sim 6 \mu\text{m/s}$. Such a low flow rate cannot be obtained experimentally, as it would require maintaining a pressure drop across the embedded channel of ~ 0.05 mBar, considering a solution with viscosity similar to water. Experimentally, a pressure difference of ~ 5 mBar (particle average residence time ~ 200 ms) was the limit before obtaining flow instabilities during the measurement. Measurements were acquired predominantly at sampling rates of 500 Hz or 1 kHz, and typical readout noise corresponded to ~ 100 mHz and ~ 200 mHz, respectively.

2.3.2 50 μm SNR device

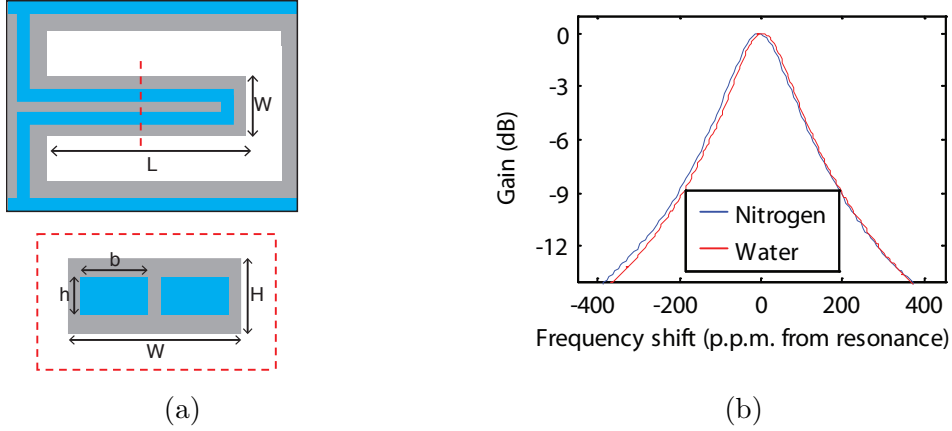


Figure 2.4: a) Schematics of the SNR cantilever resonator structure (top) and embedded microfluidic channel (bottom). The resonator dimensions are reported in Table 2.3; frequency response of the SNR50 device when filled with nitrogen gas and with milli-Q water. Because of the small dimensions of the cross-section, the device does not show a reduction in quality factor upon filling with water.

Device	$L[\mu\text{m}]$	$W[\mu\text{m}]$	$H[\mu\text{m}]$	$b[\mu\text{m}]$	$h[\mu\text{m}]$	$f_{0d}[\text{kHz}]$	Q_d	$f_{0w}[\text{kHz}]$	Q_w
SNR50	50	10	1	2	0.4	740	7000	700	7000

Table 2.3: Dimensions of the SNR device used for mass measurements of suspended particles. The symbols refer to Fig. 2.4a. The subscripts d and w refer to the device dry and filled with water, respectively.

A cantilever resonator with sub-micron cross-section dimensions was also used for mass characterization of suspended particles (Fig. 2.4a). Because of the scaling in resonator and embedded channel dimensions, these second generation devices will be referred to as suspended nanochannel resonators (SNRs) [16]. However, the notation SMRs will be employed when referring to the general class of resonators with embedded microfluidic channels, unless otherwise specified to identify a particular device.

The SNR used for mass detection is a 50 μm silicon cantilever resonator with an embedded microfluidic channel of $2 \times 0.4 \mu\text{m}^2$ cross-section dimensions. The resonator dimensions are reported in Table 2.3. The cantilever has a dry mass of $\sim 1 \text{ ng}$, i.e. ~ 100 times lighter than the SMR presented in the previous section. The resonance frequency is 741 kHz when filled with nitrogen gas and 700 kHz when filled with water. Due to the small dimensions of the cross-section, the increase in fluid viscosity caused by the water

in the embedded channel does not lead to a measurable decrease in device quality factor [70], corresponding to ~ 7000 under both fluid conditions (Fig. 2.4b). The reduction in resonator thickness corresponds to a reduction in spring constant to ~ 6.5 N/m [16]. However, the maximum deflection does not increase accordingly ($\Delta z \sim 800$ nm), as a consequence of the smaller capacitor dimensions. The thermomechanical noise corresponds to ~ 5 ppb for a 1 kHz sampling frequency, as estimated from Eq. 2.5. As for the double-paddle cantilever presented before, the theoretical limitation in frequency detection cannot be reached, and the readout noise is about two orders of magnitude larger than the thermomechanical level.

Experimental setup

Due to the reduction in cantilever dimensions, the experimental setup was modified to allow a more precise focusing of the laser on the SNR cantilever tip. A 5X beam expander was positioned between the laser and the setup lenses to widen the beam waist prior to focusing. Further focusing of the beam, to improve the laser placement and reduce laser drift effects, was not feasible without major modifications to the setup, as it would have resulted in a too high divergence of the beam before reaching the photodetector. Excitation of the device oscillation was obtained by electrostatic actuation using an electrode positioned below the cantilever, under conditions similar to the SMR actuation.

Mass resolution and detection limit

Measurements with this device presented a ~ 200 mHz readout frequency noise at a 500 Hz sampling frequency, that, according to a mass/frequency responsivity of 1 fg/Hz, limits the single-particle resolution to ~ 200 ag ($1 \text{ ag} = 10^{-18}$ g). Lower sampling frequencies can be used more easily because of the increase in fluid resistance of the channel: a flow of ~ 0.5 mm/s (corresponding to an average transit time of ~ 200 ms) in the embedded channel requires a pressure drop of ~ 10 mBar, that can be maintained with good stability.

2.4 Detection modes

Mass-induced frequency shifts in the device resonance frequency can be of two types: permanent shifts, as a consequence of accumulation of analyte in the resonator, or temporary, caused by the flow of particles in the embedded channel. This thesis presents an analysis method for the resolution enhancement of flow-through measurements; nevertheless, an overview of the mass accumulation method is included here for completeness.

2.4.1 Mass accumulation

Mass accumulation on the walls of the embedded microfluidic channel affects the effective mass of the resonator, causing a variation in resonance frequency (Eq. 2.2). Functionalization the inner surfaces of the resonator renders the device specific to sensing the captured amount of a particular analyte in solution, similar to mass detection obtained by quartz crystal microbalances (QCM) and surface plasmon resonance (SPR) devices [14]. However, QCMs and SPR devices usually present flow cells of $\sim 50 \mu\text{m}$ in height, and, as a consequence, measurements of kinetic rates can be affected by mass transport of the analyte to the surface. To overcome this limitation, high flow rates (mL/min) can be employed, at the expense of large sample consumption. On the contrary, SMR devices present channel dimensions of a few micrometers and an internal volume of $\sim 10 \text{ pL}$. Due to the small dimensions and internal volume, reaction-limited regimes can be obtained with minimal sample consumption: analytes of nanometer size diffuse through the whole cross-section in $\sim 10 \text{ ms}$, avoiding the formation of a depletion layer close to the channel walls; furthermore, flow rates of $< 1 \mu\text{L}/\text{min}$ would be sufficient for refreshing the solution in the resonator every $\sim 0.5 \text{ ms}$ [18].

As an example of accumulation detection mode, Fig. 2.5 shows the measurement of goat anti-mouse immunoglobulin G (IgG) molecules binding on anti-goat IgG antibodies, that were previously immobilized on the resonator surface. Both the surface functionalization process (Fig. 2.5a) and the binding of the analyte molecules (Fig. 2.5b) can be detected in real time by continuously monitoring the resonance frequency. Mass accumulation on the resonator surface causes a decrease in resonance frequency, as a result of the increase in the resonator effective mass. Therefore, quantification of the

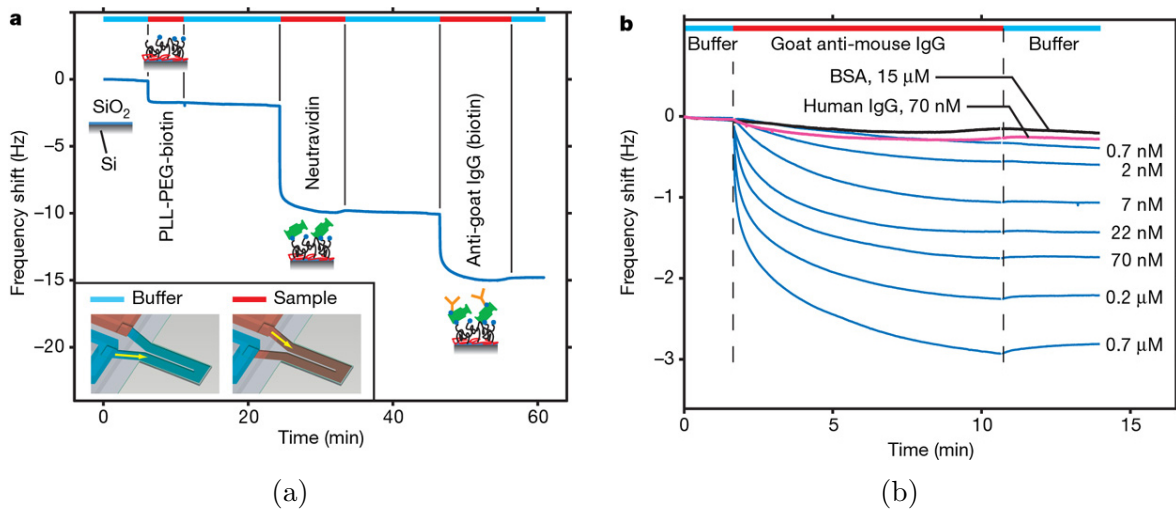


Figure 2.5: a) The inner surface of the SMR is functionalized to enable capturing of the analyte in solution. In the example presented here, anti-goat IgG are immobilized on the SMR surface by a three step process. Flowing of the functionalization solutions is highlighted in red, while the rinsing with phosphate buffer saline is in blue. As a result of the functionalization of the surface, the effective mass of the resonator increases, causing a permanent shift in resonance frequency. In the specific case shown here, a shift of ~ 15 Hz was caused by the immobilization of the antibodies; b) binding of the analyte on the functionalized surface of the SMR induces a decrease in resonance frequency, as a result of the mass accumulation. The binding can be monitored in real time by detecting the resonance frequency decrease. The figure shows frequency variations caused by the injection of goat anti-mouse IgG at different concentrations (blue curves) and of control solutions (black and red curves). These figures have been reprinted with permission from Burg *et al.* [14]. Copyright 2007 Nature Publishing Group.

induced frequency shift provides a direct measurement of the added mass.

The acquisition bandwidth can be decreased to improve mass resolution, because signal detection is based on static variations of the resonance frequency. However, bandwidths below ~ 1 Hz are usually ineffective in resolution improvements, as resonance variations caused by thermal and mechanical drifts ultimately limit the frequency stability. Nevertheless, SMRs can be used for real-time monitoring of binding event and for the characterization of biomolecular interaction kinetics, with a potential mass resolution of ~ 0.01 ng/cm² for devices with micrometer size channel dimensions [14]. Finally, the use of devices with a lower effective mass, such as the SNR presented before, would provide a proportional resolution enhancement. However, limitations on the maximum size of the analyte would be more stringent due to the reduction in channel dimensions.

2.4.2 Flow-through mode

Sensitivity profile

Particles in the resonator induce position-dependent frequency shifts in the resonance frequency. The magnitude of the shift is proportional to the relative vibration amplitude of the resonator at the particle location [72]. Figure 2.6 shows the first three resonant modes for a cantilever resonator and the associated sensitivity profiles. The mode shapes are described by [72]

$$U_n(x) = C_1 (\cos(k_n x) - \cosh(k_n x)) + C_2 (\sin(k_n x) - \sinh(k_n x)) \quad (2.8)$$

where the subscript n denotes the oscillation mode, k_n is the mode wave number, C_1 and C_2 are the mode coefficients that fulfill $C_1/C_2 = (\cos(k_n L) + \cosh(k_n L))/(\sin(k_n L) - \sinh(k_n L))$. For the modes reported in Fig. 2.6, $k_n L = 1.875, 4.694$ and 7.855 . Denoting as Δf_{pn} the maximum frequency shift induced by the particle flowing in a resonator oscillating at the n -th mode, the position-dependent response of the cantilever is shown in Fig. 2.6c. The curves are calculated as [72]

$$\frac{\delta f_p(x)}{\Delta f_{pn}} = \left(\frac{U_n(x)}{U_{n0}} \right)^2 \quad (2.9)$$

where $\delta f_p(x)$ is the induced frequency shift for a particle at position x and U_{n0} the maximum oscillation amplitude at the n -th mode. Nodes in the resonant mode shape represent points of zero mass sensitivity, while maximum response occurs at points of maximum vibration. SMR devices operated at the second resonant mode have already been presented [73], however SMRs are most commonly used in the first mode for the ease of operation and oscillation detection [14, 16, 20, 22, 23]. For this reason, the calculations will only focus on the first oscillation mode and Δf_{p1} will be simply referred to as Δf_p .

To simplify the expression of the sensitivity profile in the first resonant mode, the cantilever deflection function can be approximated by a first order polynomial. The

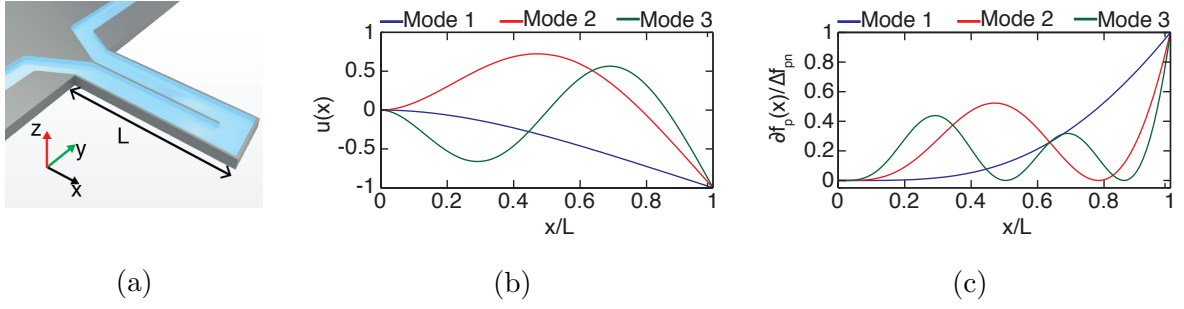


Figure 2.6: a) Schematics of a SMR device, with cantilever length L along the x -axis. The embedded channel length is approximated to $2L$; b) first three resonant modes for a cantilever resonator; c) sensitivity profile of the resonator according to the oscillation mode. The induced frequency shift varies with the particle axial position.

position-dependent induced frequency shift can be described as

$$\delta f_p(x) = \Delta f_p \left(\frac{x}{L} \right)^2 \quad (2.10)$$

and Δf_p can be derived from Eq. 2.4

$$\frac{\Delta f_p}{f_0} = -\frac{1}{2} \frac{\Delta m_p}{m^*} \quad (2.11)$$

Δf_p corresponds to the induced frequency shift when the particle is at the tip of the cantilever resonator. The linear approximation of the deflection function and the resulting quadratic sensitivity profile (Eq. 2.10) are shown in Fig. 2.7.

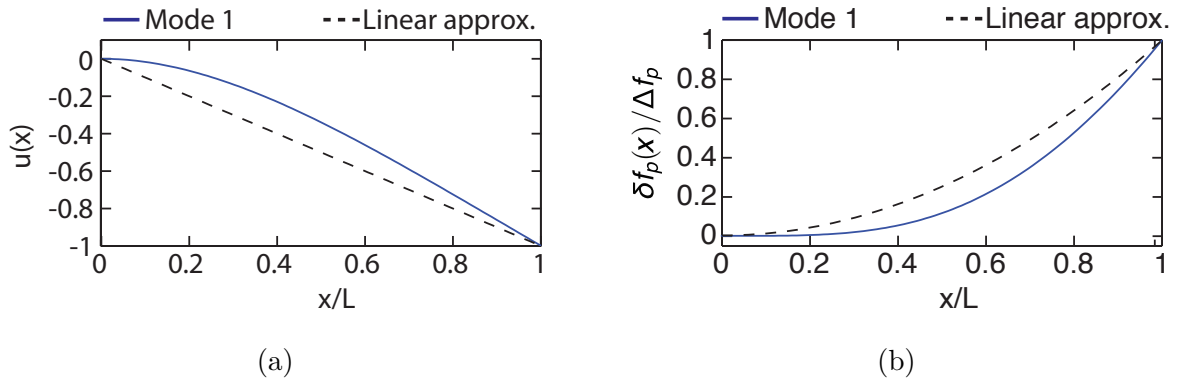


Figure 2.7: a) The first oscillation mode is approximated with a linear function for simplifying the calculations; b) comparison between the approximated and the analytical sensitivity profile.

Transient particle signature

Particles flowing through the embedded channel in the resonator present a characteristic transient frequency shift as a result of their motion. For simplicity, the embedded channel can be mapped to a linear geometry of length $2L$, where the point of maximum deflection is $x = L$. Defining t_p the time spent by the particle in the resonator, the axial position of the particle is given by

$$x(t) = \frac{2L}{t_p}t \quad (2.12)$$

and $0 \leq t \leq t_p$. Inserting Eq. 2.12 in Eq. 2.10, the characteristic frequency shift for a flowing particle is

$$\delta f(t) = \Delta f_p \begin{cases} \left(\frac{x(t)}{L}\right)^2 & \text{for } 0 \leq t \leq t_p/2 \\ \left(\frac{2L-x(t)}{L}\right)^2 & \text{for } t_p/2 < t \leq t_p \\ 0 & \text{otherwise} \end{cases} \quad (2.13)$$

From Eq. 2.13 and Eq. 2.11, it can be noticed that the buoyant mass of the particle Δm_p defines the magnitude of the induced frequency shift, while the duration of the transient depends on the time t_p spent by the particle in the channel. Figure 2.8 shows a typical particle-induced transient frequency shift. Because of the non-negligible width of the channel at the resonator tip, the maximum induced shift suffers of an intrinsic position-dependent uncertainty. For a $60 \mu\text{m}$ cantilever and a $8 \mu\text{m}$ channel width, the uncertainty is $\sim 8\%$. However, this corresponds to an uncertainty of less than 3% when converted to an uncertainty in particle radius.

Noise in the resonance frequency detection sets a clear limit on the mass of the objects that can be characterized by the SMRs in flow-through mode. In this work, an ensemble based method was developed to detect particle signatures, even when these are orders of magnitude smaller than the readout frequency noise. This is achieved by correlation analysis of the time-domain mass signal. The method is presented in detail in Chapter 3 and 4.

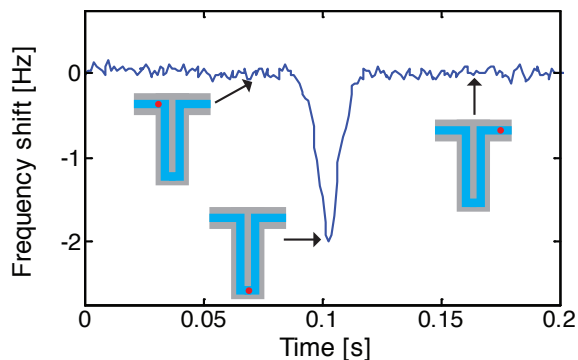


Figure 2.8: Transient frequency shift of a $1.54 \mu\text{m}$ polystyrene bead suspended in water (buoyant mass 95 fg). The signature shape is a function of the resonator sensitivity profile and the time extension equals the time spent by the particle in the resonator. The maximum shift occurs when the particle passes the apex of the cantilever. The induced frequency shift scales with the buoyant mass of the particle. For clarity, the trace has been smoothed with a Savitzky-Golay filter.

2.5 Experimental method

2.5.1 Mass measurements

To begin, the sample is introduced into one of the two bypass channel and the remaining bypass channel is filled with a wash solution, i.e. a solution that slightly differs from the suspending buffer of the particles. This has the double advantage of avoiding drastic changes in sample conditions upon mixing with the wash solution and, at the same time, clearly identifying what solution is in the resonator at any time of the measurement, by looking at the resonance frequency variation caused by slight differences in solution densities.

When the sample bypass is filled, the measurement is ready to begin (Fig. 2.9) and the solution can be pushed through the embedded channel by varying the externally applied pressures ($P1 \approx P2$ and $P3 \approx P4$, with $P1 > P3$). For flow-through measurements, it is important that the pressure drop across the resonator channel is low enough so that particle signatures are visible in the time-trace. As particles might interact with the walls, every $30 \text{ s} \sim 1 \text{ minute}$ the flow is reversed to rinse the channel with wash solution (Fig. 2.9, steps II and III). This looping is performed several times to increase the statistics of the measurement. The typical sample flow rate within the measurement channel is $\sim 20 \text{ nL/min}$, however $\sim 15 \mu\text{L}$ are required to fill the connecting tubes and

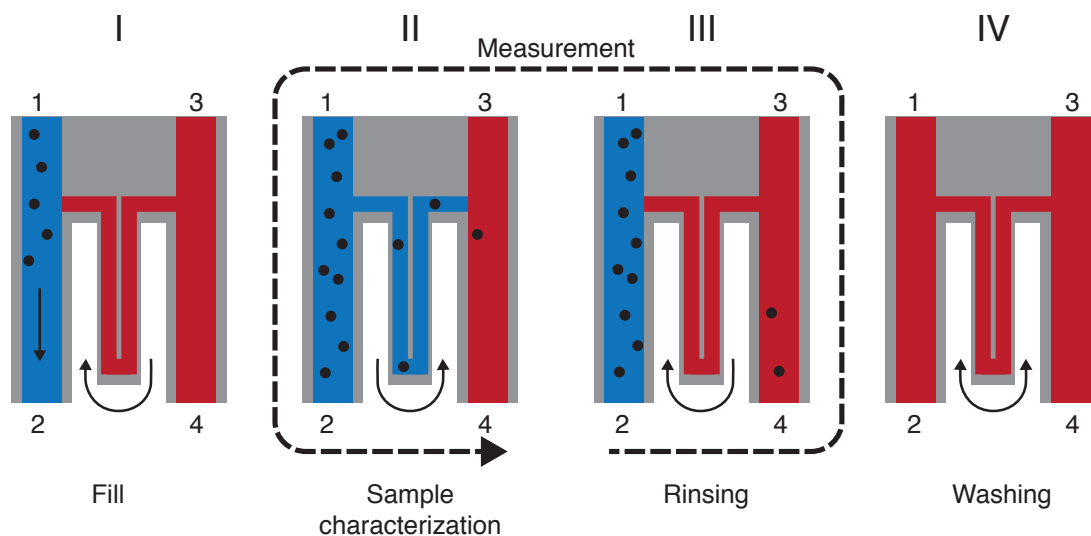


Figure 2.9: I) The sample is inserted in the bypass channel while the resonator is filled with wash solution. The measurement is then started, and (II) the sample is flown through the embedded channel. After ~ 1 minute, (III) the flow is reversed to rinse the channel and remove particles weakly interacting with the walls. The procedure is repeated several times. IV) End of the measurement; the sample is removed from the bypass channel and the whole chip is rinsed with wash solution.

bypass channel. When the measurement is concluded, the chip is rinsed with wash solution (Fig. 2.9, step IV).

Cleaning of the device is accomplished by flowing $10 \mu\text{L}$ of a mixture of sulfuric acid and hydrogen peroxide (piranha solution) throughout the two bypass channels and the resonator embedded channel. The cleaning procedure is performed after each measurement.

Precise control of the flow conditions and continuous monitoring of the resonance frequency is done via a custom-designed Labview interface. The resonance frequency is acquired using a heterodyne measurement scheme, as described before (see page 18).

2.5.2 Data analysis

Slow-varying noise terms

Mass characterization of particles flowing through the embedded channel is based on the quantification of the transient induced frequency shift. After calibration of the

mass/frequency response of the resonator, relative frequency variations are sufficient to obtain the mass characterization of the particles, and absolute resonance frequency values can be discarded without loss of information. Under normal experimental conditions, particles flow through the resonator in <200 ms, therefore the particle signatures can be safely separated from the static frequency baseline applying a high pass filter (cutoff frequency 1 Hz) to the recorded signal (Fig. 2.10). This also removes slow-varying noise terms, such as fluctuations due to thermal and mechanical drifts during measurement. The analysis of the time-domain frequency measurement is performed in MATLAB (Mathworks Inc.), using customized data analysis scripts (see Appendix A).

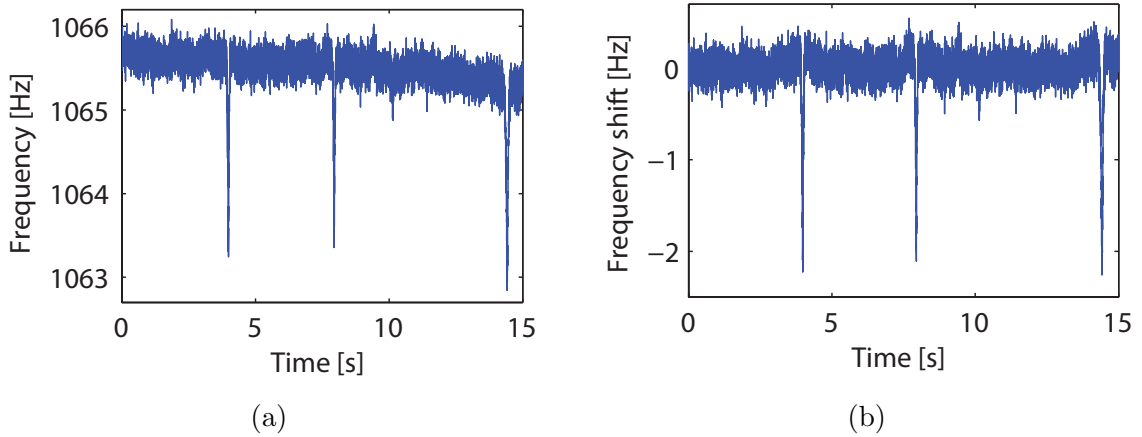


Figure 2.10: a) Frequency measurement, as recorded by the frequency counter. The sampling frequency (~ 1 kHz) corresponds to the difference between the cantilever resonance and the reference frequency; b) time-trace after high-pass filtering (1 Hz cutoff frequency).

Signal preparation for correlation analysis

The zeroed frequency trace is autocorrelated to extract preliminary information on the average time t_{avg} spent by the particles in the resonator. t_{avg} can be inferred by looking at the non-zero correlation amplitude around lag zero, corresponding to the sum of all particle signature autocorrelations¹ (see Fig. 2.11a). Particle signature locations in the frequency trace are identified using a matched filter and their position is stored for further analysis. The signatures are then deleted from the zeroed trace, removing

¹More information on the autocorrelation and the calculation procedure is presented in Sec. 3.1.

a number of points corresponding to $t > t_{avg}$. Finally, the remaining trace can be analyzed with the correlation analysis to characterize particles whose signatures are buried in the noise background.

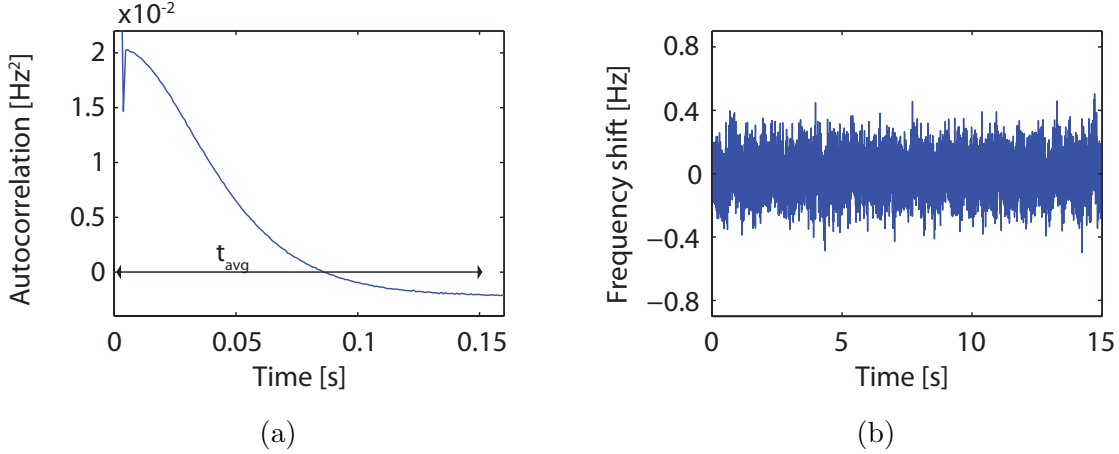


Figure 2.11: a) Autocorrelation of the zeroed time-trace. The non-zero correlation amplitude is caused by the particle signatures in the time-trace. The average time spent by the particles in the channel can be calculated from the curve extension; b) clear single-particle signatures are identified and their signatures are removed from the time-trace. The remaining portions of the trace are then analyzed with the correlation analysis, for characterizing particles whose mass falls below the resolution limit.

Single-particle characterization

The characterization of the particle-induced frequency shifts visible in the measurement trace is done from the raw frequency trace (Fig. 2.10a), as baseline removal by high-pass filtering might affect the transient signature amplitude². From the locations identified in the zeroed trace, particle signatures are extracted from the raw frequency measurement and the baseline is estimated by looking at the trace before and after the induced characteristic signature. As the portion of analyzed signal is short ($\approx t_{avg}$), the baseline drift can be safely approximated with a linear function. Finally, a Savitzky-Golay filter is applied to the particle signatures to improve the resolution on the frequency shift estimation (Fig. 2.12). Frequency/mass conversion is then calculated after calibration of the device responsivity with particles of known mass.

²While the high pass filtering also affects the “small” particle signatures, the effect is usually negligible because frequency fluctuations already present an average value ≈ 0 .

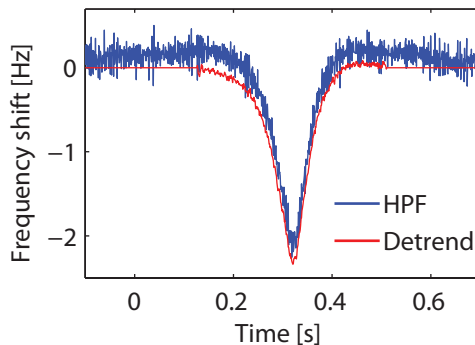


Figure 2.12: Quantification of single-particle induced frequency shift. The figure compares a single-particle characteristic signature after baseline removal by high-pass filtering (blue) and by linear detrending (red). To improve the frequency shift quantification, a shape preserving Savitzky-Golay filter is also applied to the red curve.

2.5.3 Mass conversion calibration

Particles of known diameter and mass are added to each sample to serve as mass/frequency conversion calibration and to monitor the flow conditions during measurement.

Double-paddle resonator

NIST quality polystyrene beads of $1.54 \pm 0.04 \mu\text{m}$ size (Polysciences Inc., Cat# 64040) are used as calibration beads for the double-paddle SMR device. With a buoyant mass of $\sim 96 \text{ fg}$, the beads induce clear frequency shifts of $\sim -2 \text{ Hz}$ in normal experimental conditions (see Fig. 2.12). Furthermore, the high monodispersivity of the particle population makes them an ideal sample for calibration purposes. Fig. 2.13 shows the measured frequency shifts induced by the reference beads suspended in milli-Q water. The standard deviation of the distribution includes both the intrinsic sample distribution and the variation caused by the particle position uncertainty at the tip of the resonator. Particles with diameter comparable to the cross-section dimensions also act as precise references for the estimation of the flow conditions during measurement, as they present a very narrow velocity distribution in the channel (as explained in Chapter 4).

From the measurements in milli-Q water, the mass responsivity of the double-paddle resonators corresponds to $\sim 20 \text{ mHz/fg}$.

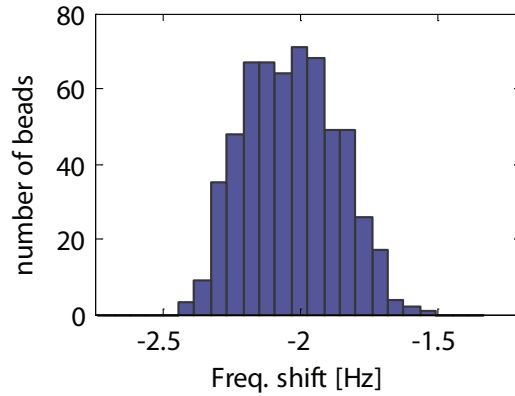


Figure 2.13: Measured induced frequency shifts caused by the $1.54 \mu\text{m}$ polystyrene beads in water when passing the apex of the SMR. 580 beads were measured under different flow conditions. The population distribution variance includes the particle mass distribution and the position dependent uncertainty.

50 μm SNR device

PMMA beads of $222 \pm 38 \text{ nm}$ (Phosphorex Inc., Cat# NR 1109245-085) were used as calibration for the measurements with the $50 \mu\text{m}$ SNR device. With a buoyant mass of 1.09 fg in water, the characterization of the reference particles returns a frequency/mass conversion of $\sim 1 \text{ Hz/fg}$. The frequency shifts induced by the particles flowing through the resonators are shown in Fig. 2.14. With a channel width of $2 \mu\text{m}$ and a resonator length of $\sim 50 \mu\text{m}$, particle position uncertainty at the resonator apex generates a $\sim 2\%$ variation in mass estimation. Therefore, the large frequency shift distribution in Fig. 2.14 is mostly dominated by the particle mass distribution.

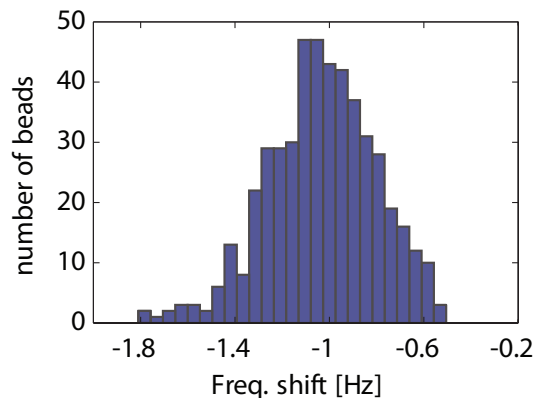


Figure 2.14: Induced frequency shifts caused by the 222 nm PMMA beads in water when passing the apex of the $50 \mu\text{m}$ SNR device. 559 beads were measured under different flow conditions.

Chapter 3

Resolution enhancement of SMR

Suspended microchannel resonators (SMR) have enabled mass measurement of particles in solution with unmatched resolution [14, 15, 16, 20]. In flow-through mode, particles induce a transient frequency shift

$$\Delta f_p = -\frac{1}{2} \frac{f_0}{m^*} \Delta m_p \quad (3.1)$$

where Δm_p is the buoyant mass of the particle, f_0 is the resonance frequency of the device and m^* is the effective mass of the resonator. SMRs of the first generation have resonator masses of ~ 100 ng and resonance frequencies of ~ 1 MHz. With a readout noise level of ~ 0.1 Hz, these devices present resolution limits around the 10 fg mark. This detection capability has allowed SMR application to the mass and density characterization of cells and bacteria in solution, as a result of the single-particle detection capability and the possibility of rapid exchange of buffer conditions inside the embedded channel [22, 23, 24, 74].

Reducing the acquisition sampling rate effectively increase the mass resolution by lowering the readout noise. However, this approach decreases the measurement throughput: slower flow rates would need to be used to reliably detect individual particles crossing the resonator, effectively reducing the particle count rate. Furthermore, because of the extremely small pressure differences applied to control fluid velocity, instabilities in flow conditions would likely occur during the measurement. To circumvent these limitations, devices with higher sensitivity were realized by reducing the effective mass of

the resonators. This solution was pursued with two different strategies, namely scaling the device dimensions [16, 20] and by operating the devices at higher resonance modes [73]. This latter strategy, however, presents limited applicability and resolution enhancement, due to the difficulties in exciting and detecting higher modes of vibration. On the contrary, devices with sub-micrometer cross-section dimensions, the suspended nanochannel resonators (SNRs, page 22), have achieved attogram detection level in single-particle mode [20]. However, the reduction in channel cross-sections imposes a strict limit in particle size, as this cannot exceed the channel smallest dimension.

Here, I present a novel approach for enhancing the resolution of embedded channel resonators. This method extends the measurement range of SMR devices into a regime where single-particle detection is not possible. Using a correlation analysis of the time-domain mass signal, enhancement of particle signal contributions with respect to the uncorrelated noise background is achieved, even when single-particle signatures are several orders of magnitudes below the noise floor [19]. The theoretical explanation of the analysis will be presented here and corroborated by measurements on validated samples. Resolution enhancement of five orders of magnitude was achieved using this approach.

3.1 Mass Correlation Spectroscopy

Particles flowing through the microfluidic channel embedded in the resonator cause transient shifts to the resonance frequency of the device. The magnitude of the shifts depends on the buoyant mass of the particles and on their axial positions (Eq. 2.10). When the sample concentration is such that more than one particle is present in the resonator at any time, the effective mass density of the fluid is altered and this is reflected in a shift of the mean resonance frequency. This static variation in resonance value depends on both the sample total dissolved mass in solution and on its density. However, in typical experimental conditions the shift is too small to be measured with precision¹. This is due to slow varying noise effects, such as thermal drift or non-specific binding. Additionally, frequency changes induced by fluid pressure variations

¹Considering polystyrene beads dissolved in milli-Q water at 1 mg/mL, the average frequency shift would correspond to ~ 1.5 Hz for the SMR presented in Sec. 2.3

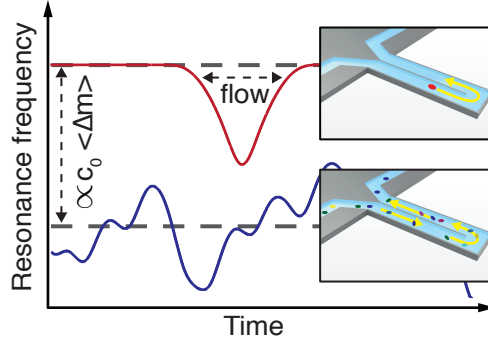


Figure 3.1: A single-particle traveling through the resonator generates a characteristic transient signature in the resonance frequency (red). When several particles are present in the resonator, they give rise to a static shift of the resonance frequency and to oscillations caused by the number density fluctuations in the channel (blue).

are of the same order of magnitude, potentially masking this effect. This problem is not encountered when dealing with number density fluctuations of particles in the embedded channel. As particles are discrete objects, their number in the resonator fluctuates around the average concentration value, causing oscillations in resonance frequency as a consequence of the linear superposition of the individual single-particle signatures (Fig. 3.1). When flow conditions are kept stable, particle signatures present similar temporal extension, generating a repeating pattern in the resonance frequency time-trace. This pattern can be enhanced by using an autocorrelation analysis of the time-domain mass signal, even when single-particle signatures are several orders of magnitude smaller than the detection noise. Assuming a random and uncorrelated measurement noise background, noise contribution in the autocorrelation is confined to $\tau \approx 0$ [75], where τ is the autocorrelation lag time. On the contrary, particles spending on average a time t_p in the resonator would affect the autocorrelation for time lags up to $\tau \approx t_p$. Through the autocorrelation analysis, the sample contribution can be easily separated from the noise due to their temporal extension differences in the correlation signal, at the expense of losing single-particle characterization capability.

3.1.1 MCS - definition

Assuming a sample of identical particles with maximum induced frequency shift Δf_p , the fluctuations of the resonance frequency are described by

$$\delta f(t) = \Delta f_p \cdot \int_V \delta c(x, y, z, t) \cdot u(x)^2 dy dz dx \quad (3.2)$$

where the integral is calculated over the volume V of the embedded microfluidic channel, $\delta c(x, y, z, t)$ denotes the concentration fluctuation at position (x, y, z) . $u(x)$ is the deflection function of the cantilever and $u(x)^2$ corresponds to the sensitivity profile of the resonator. It should be noted that $\delta f(t)$ only describes the frequency fluctuations around the average resonance value, and experimentally corresponds to the high-pass filtered signal, with zero mean and no baseline drift. The autocorrelation analysis² of the signal is defined as

$$C(\tau) = \langle \delta f(t) \delta f(t + \tau) \rangle \quad (3.3)$$

where ' $\langle \bullet \rangle$ ' is the ensemble-based expected value. By inserting Eq. 3.2 in Eq. 3.3, the autocorrelation of the high-pass filtered signal is

$$C(\tau) = \Delta f_p^2 \iint_V \langle \delta c(x, y, z, t) \delta c(x', y', z', t + \tau) \rangle \times u(x)^2 u(x')^2 dy dz dx dy' dz' dx'. \quad (3.4)$$

The correlation signal contains information on both the average mass, concentration and size of the particles. The magnitude of $C(\tau)$ increase with the particle concentration and with the induced frequency shifts Δf_p , proportional to buoyant mass of the particles in solution. The shape of $C(\tau)$, instead, depends on the temporal correlation of the concentration fluctuations, containing information on the size and diffusion of the particles, as well as the interactions with each other and with the flow profile.

The velocity profile in the cross-section is not uniform and particles move at different velocities according to their position in the cross-section. However, the velocity

²The function $C(\tau)$ is called 'autocovariance' in statistics; however, in signal processing it is commonly referred to as 'autocorrelation', despite the missing normalization factor. This latter convention will be used in the text and the normalization factor will be stated explicitly when applied.

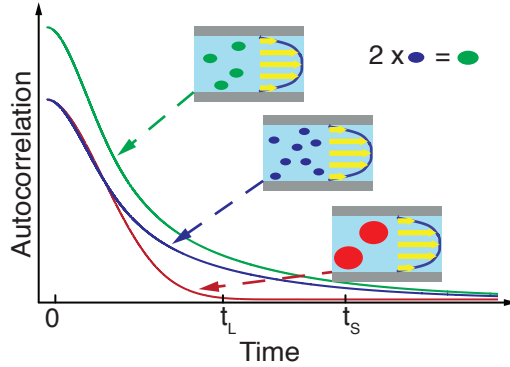


Figure 3.2: Expected autocorrelation signals for different types of particles. The autocorrelation amplitude depends on the sample individual particle mass and concentration: heavier particles present a higher autocorrelation, even if the sample dissolved mass coincides; autocorrelation shape varies with the particle size: in red, particles of diameter comparable to the channel cross-section; in blue and green, small particles, that can closely approach the channel walls. t_L and t_S denotes the average time spent in the resonator by the large and small particles, respectively.

distribution of the sample is not constant, because particles change position in the radial direction as a result of diffusion [76]. Furthermore, the finite size of the particles limits the accessible regions of the velocity profile, as particles are precluded from closely approaching the channel walls [77]. Examples of autocorrelation curves coming from different samples are depicted in Fig. 3.2. Large particles are confined to the center region of the cross-section and only experience the fast portion of the velocity profile. Small particles, instead, present a long-tailed autocorrelation, resulting from the slow moving particles positioned close to the channel walls. Finally, samples with the same dissolved mass in solution, but not individual particle mass, present different autocorrelation amplitudes (green and blue curves in Fig. 3.2).

From here onward, the autocorrelation analysis of the high-pass filtered mass signal will be referred to as Mass Correlation Spectroscopy (MCS). The results presented in this chapter will focus on the study of the autocorrelation magnitude, while the analysis of the autocorrelation shape will be presented in Chapter 4. Here, the calculation of the autocorrelation will be performed using an compartment approximation of the velocity profile in the channel.

3.1.2 MCS - amplitude

To calculate $C(\tau)$ for a sample flowing through an embedded microfluidic channel of rectangular shape, a simplification of the velocity profile can be made by discretizing the cross-section into M compartments of area A_i ($i = 1 \dots M$). Within each compartment, the flow profile is approximated by a plug flow of velocity

$$v_i = \frac{1}{A_i} \iint_{A_i} U(y, z) dy dz. \quad (3.5)$$

where v_i is the average flow velocity in the i -th compartment and $U(y, z)$ is the velocity profile in the cross-section, defined by [76]

$$U(y, z) = U_{max} \left[1 - \frac{y^2}{h^2} - \frac{32}{\pi^3} \sum_{n=0}^{\infty} \frac{(-1)^n}{(2n+1)^3} \right. \\ \left. \times \frac{\cosh\left(\frac{(2n+1)\pi y}{2h}\right)}{\cosh\left(\frac{(2n+1)\pi}{2\beta}\right)} \cos\left(\frac{(2n+1)\pi z}{2h}\right) \right] \quad (3.6)$$

with $U_{max} = U(0, 0)$ the maximum flow velocity at the center of the cross-section, $\beta = h/b$ the channel aspect ratio, $-h \leq y \leq h$ and $-b \leq z \leq b$.

Assuming that concentration fluctuations in different regions of the cross-sections are uncorrelated and particle diffusion between compartments can be neglected, the autocorrelation can be expressed as

$$C(\tau) = \sum_{i=1}^M C_i(\tau) \quad (3.7)$$

where

$$C_i(\tau) = \Delta f_p^2 \iint_{V_i} \langle \delta c(x, y, z, t) \delta c(x', y', z', t + \tau) \rangle \\ \times u(x)^2 u(x')^2 dy dz dx dy' dz' dx'. \quad (3.8)$$

Here, the integral is calculated over the compartment volume $V_i = A_i \times 2L$. As the flow velocity in each compartment is assumed constant, the concentration correlation

function simplifies to

$$\langle \delta c(x, y, z, t) \delta c(x', y', z', t + \tau) \rangle = c_0 \delta(x - x' - v_i \tau) \delta(y - y') \delta(z - z') \quad (3.9)$$

with $\delta(x)$ the Dirac delta function and c_0 corresponding to the average sample concentration. The scaling factor c_0 derives from the assumption that the fluctuations of particle number in the channel are uncorrelated and follow a Poisson distribution [42]. Substituting Eq. 3.9 in Eq. 3.8 yields

$$C_i(\tau) = \Delta f_p^2 c_0 A_i \int_0^{2L} u(x)^2 u(x - v_i \tau)^2 dx. \quad (3.10)$$

For a cantilever resonator vibrating at the first resonant mode, the deflection function can be approximated as (see section 2.4.2)

$$u(x) = \begin{cases} \frac{x}{L} & \text{for } 0 \leq x \leq L \\ \frac{2L-x}{L} & \text{for } L < x \leq 2L \\ 0 & \text{otherwise} \end{cases} \quad (3.11)$$

Therefore, the integral can be readily calculated

$$\begin{aligned} g(s) &\equiv \int_0^{2L} u(x)^2 u(x - s)^2 dx \\ &= \begin{cases} L \cdot \left(\frac{1}{30} \left(2 - \frac{|s|}{L} \right)^5 - \frac{2}{3} \left(1 - \frac{|s|}{L} \right)^4 \right) & \text{for } |s| \leq L \\ L \cdot \frac{1}{30} \left(2 - \frac{|s|}{L} \right)^5 & \text{for } L < |s| \leq 2L \\ 0 & \text{otherwise} \end{cases} \end{aligned} \quad (3.12)$$

and the autocorrelation for the i -th compartment of size A_i is

$$C_i(\tau) = \Delta f_p^2 c_0 A_i g(v_i \tau). \quad (3.13)$$

It is now possible to describe the complete autocorrelation as the sum of $C_i(\tau)$ over all the compartments in the cross-section. However, to fit the experimental data, it is

advantageous to define the normalized autocorrelation

$$G(\tau) = \frac{\sum_{i=1}^M C_i(\tau)}{\sum_{i=1}^M C_i(0)} \quad (3.14)$$

such that $G(0) = 1$. This function is then used as the basis for a two-parameter model $\beta_1 \cdot G(\beta_2 \frac{k}{f_s})$ used to fit experimental mass-signal autocorrelations, calculated as

$$\hat{C}[k] = \frac{1}{N-k} \sum_{i=1}^{N-k} \delta f_i \cdot \delta f_{i+k}. \quad (3.15)$$

Here δf_i denotes the discrete and high-pass filtered signal, with sampling frequency f_s and $i = 1 \dots N, N = T_{meas} \cdot f_s$. The fit parameter $\hat{\beta}_1$, representing the magnitude of the curve, corresponds to

$$\langle \hat{\beta}_1 \rangle = \frac{1}{5} \Delta f_p^2 c_0 V \quad (3.16)$$

where V is the embedded channel volume. Importantly, the MCS amplitude dependence on particle concentration and mass is not equal. Two samples, which have dissolved mass in solution that coincide the same density, would generate an equal static shift in resonance frequency, but different MCS amplitudes. Finally, for a sample composed of a polydisperse distribution of particles, the factor Δf_p^2 has to be replaced by the population mean square value $\langle \Delta f_p^2 \rangle$.

Compartment approximation

A simple compartment model of the flow profile in the cross-section is used to fit the experimental curves. Despite the qualitative description of the particle flow, the approximation follows the experimental data with sufficient precision to obtain reliable estimations of the MCS amplitude.

As reference beads and particles of interest usually present large differences in size, two separate compartment approximations are needed, to account for the flow differences. Figure 3.3 shows the comparison between the flow profile in the channel and the division in compartments for the reference and the small particles. The size of the compartments is calculated as the sum of both the particle size and the mean average diffusion during the crossing of the embedded channel. For the small particles'

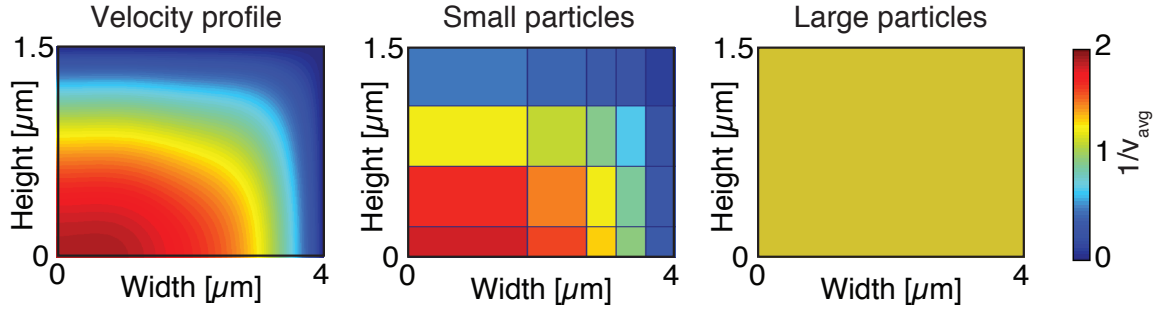


Figure 3.3: Comparison between the fluid velocity profile (left) and the compartment approximation for particles of different sizes (in center, for particles of ~ 100 nm; on the right, for particles larger than $1 \mu\text{m}$). The values are normalized to the average fluid velocity. Only one quarter of the cross-section is shown, as the flow profile presents two planes of symmetry, in the vertical and horizontal directions. Consistent with the notation used in the text, position $(0,0)$ corresponds to the center of the cross-section.

situation, the compartments are based on a 100 nm particle crossing the resonator in 50 ms, resulting in a bin size of $450 \times 450 \text{ nm}^2$. Since the velocity profile is almost constant along the horizontal dimension in the vicinity of the channel center, it is possible to reduce the number of compartments by merging adjacent streams with similar velocities, obtaining a total number of 20 streams. When dealing with particles of size comparable to the channel cross-section, such as the $1.54 \mu\text{m}$ polystyrene beads used here as frequency/mass calibration beads, one compartment is sufficient to describe their flow through the channel.

3.2 Signal-to-noise ratio

To estimate to what extent the detection limit of the suspended micro- and nanochannel resonators can be enhanced with correlation analysis, the signal-to-noise (S/N) ratio can be calculated as a function of concentration and measurement time. The S/N can be approximated as the ratio between the autocorrelation amplitude and the residual noise in $\hat{C}[k]$, which has variance $\sigma_C^2 \approx \frac{\sigma_n^4}{N}$ for $0 < k \ll N$. Here σ_n^2 denotes the variance of the readout noise, which depends on the sampling frequency f_s for an adequately band limited signal. Therefore, the S/N corresponds to

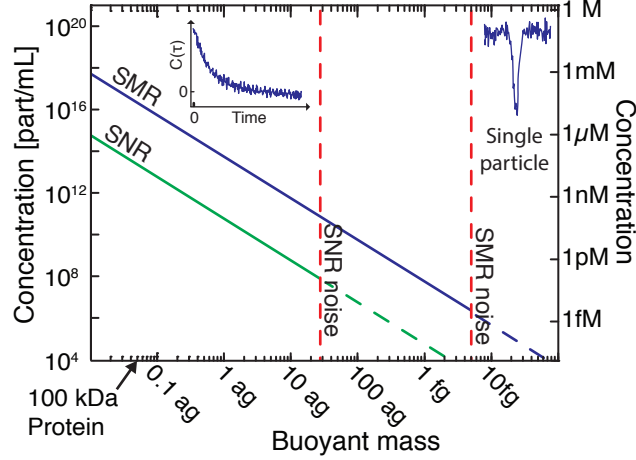


Figure 3.4: Signal-to-noise ratio of the MCS for suspended micro- and nanochannel resonators (SMRs and SNRs) as a function of particle concentration. The red dashed line shows the current single-particle measurement limit of the devices. The parameters considered are $\sigma_n=5$ fg for the SMRs and $\sigma_n=27$ ag, 1 kHz sampling frequency and $T_{meas}=200$ s. Reprinted from Modena *et al.* [19].

$$S/N \geq \frac{1}{5} \frac{\Delta f_p^2}{\sigma_n^2} c_0 V \sqrt{T_{meas} f_s} \quad (3.17)$$

Figure 3.4 shows the minimum required sample concentrations for having a S/N ratio greater than 1 for different generation devices as a function of buoyant mass of the particles and considering typical experimental conditions.

Interestingly, the MCS method does not present a limit in terms of detectable mass, but the limit of detection is defined by the sample concentration and measurement time. Resolution can be enhanced by increasing the acquisition time and the sample concentration within practical experimental limitations: sample volume and flow stability ultimately defines the maximum acquisition time, and concentration is limited by the sample solubility. Furthermore, Eq. 3.17 also shows that shrinking the internal volume V of the resonator would cause a decrease in S/N ratio. However, the effect of volume reduction would be compensated by the higher mass responsivity and lower fluid damping of resonators with smaller dimensions [70].

3.3 Validation of the MCS method

To validate the resolution enhancement obtained using correlation analysis, mass measurements of polystyrene nanoparticles suspended in aqueous solutions are presented. Polystyrene beads of known size were characterized with devices of different cross-section dimensions to demonstrate the capability of the analysis in extending the detection range of difference generation devices.

3.3.1 SMR resolution enhancement

A sample containing 85 nm polystyrene beads suspended in an aqueous buffer was characterized by using a double-paddle SMR. To characterize measurement repeatability and concentration dependence of the autocorrelation signal, the beads were measured under different flow conditions, ranging from ~ 0.6 to ~ 6.5 mm/s average flow velocity, and at concentrations of 0.38% solid and 0.25% solid content in solution.

The autocorrelations of the two bead solutions are shown in Fig. 3.5, compared to the correlation curve of pure buffer with no particles. As expected, the magnitude of the curves scales linearly with the sample concentration and oscillates around zero for

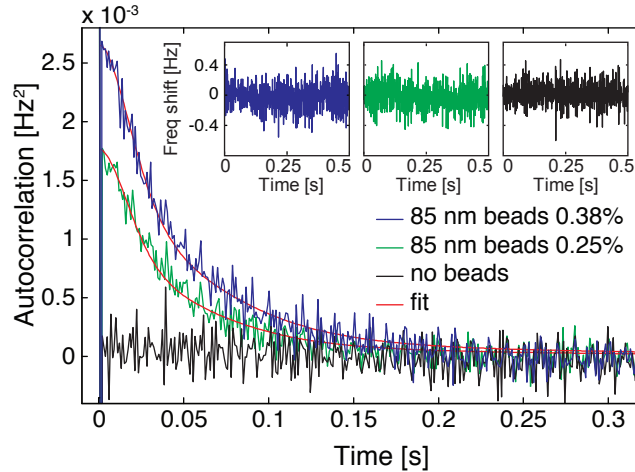


Figure 3.5: MCS signals for a sample of 85 nm polystyrene nanoparticles measured at different concentrations and pure solution correlation curve. The fit curves used for interpreting the data are shown in red. In the insets, short excerpts of the 1 Hz high-pass filtered time domain traces for the three measurements are shown. Reprinted from Modena *et al.* [19].

the case of no beads in solution. The insets in Fig. 3.5 show short segments of the time-domain mass traces for the three cases. Due to the low buoyant mass of the beads, no single-particle event and no systematic frequency fluctuations can be identified. The average buoyant mass of the particles can be calculated by fitting the autocorrelation curves with the model described before. From the curve amplitude and knowing the particle concentration, a single bead induces an average frequency shift of $467 \pm 16 \mu\text{Hz}$. The error reported here corresponds to the reproducibility error calculated from the measurements taken at different concentrations and flow conditions. With a frequency/mass conversion of $-21.7 \pm 1.7 \text{ mHz/fg}$ calculated from the reference particles in solution, the average mass of the individual bead translates to $21.5 \pm 0.7 \text{ ag}$ (statistical error $\sim 0.3 \text{ ag}$) that corresponds to a diameter of $97 \pm 1 \text{ nm}$, assuming a bead density of 1.05 g/cm^3 . The average values found here are in agreement with the manufacturer specification of $85.4 \pm 6.4 \text{ nm}$, considering possible systematic uncertainties in calibration, geometry manufacturing tolerances or the presence of a low amount of aggregated beads in solution.

Finally, the readout frequency noise in the measurements was $\sim 200 \text{ mHz}$, corresponding to a resolution limit of $\sim 30 \text{ fg}$ in single-particle detection mode for a signal-to-noise ratio of 3. Therefore, correlation analysis of the time-traces allowed an increase in mass resolution of about five orders of magnitude.

3.3.2 SNR resolution enhancement

Measurements were also taken with a SNR device with cross-section dimensions of $2 \times 0.4 \mu\text{m}^2$ (width \times height). The resonator has a mass sensitivity of $-1.0 \pm 0.1 \text{ Hz/fg}$, limiting single-particle detection to objects above $\sim 200 \text{ ag}$. Here, 43 nm polystyrene beads suspended in water (expected buoyant mass of $\sim 2 \text{ ag}$) were successfully characterized using the MCS method.

As a result of the change in cross-section dimensions and aspect ratio, a different compartment approximation of the velocity profile was calculated. Considering a sample of 50 nm transiting through the embedded microfluidic channel in 100 ms , the compartments take a characteristic dimension of $\sim 700 \text{ nm}$. Three compartments in the wide dimension are sufficient to accurately fit the autocorrelation curve of the beads.

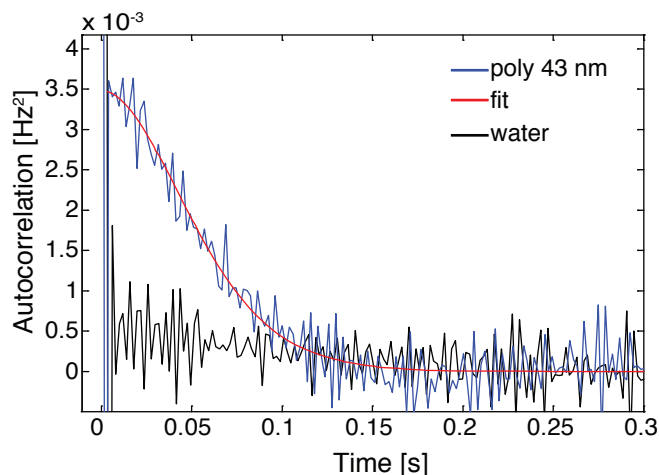


Figure 3.6: MCS signal for a sample of 43 nm polystyrene beads in milli-Q water. For comparison, the pure water correlation signal is shown.

The MCS signal and the relative fit are presented in Fig. 3.6. From the fit parameters, the average particle buoyant mass corresponds to 2.4 ± 0.3 ag. The error reported here includes the calibration error in frequency/mass conversion, while the statistical error in the autocorrelation fit reduces to $\sim 2\%$. According to the manufacturer specifications, the expected bead mass corresponds to 2.1 ag, in good agreement with the measured value.

The measurement of the 43 nm polystyrene beads shows that the resolution enhancement obtained via correlation analysis would enable these devices to characterize samples of biological interest, at relatively low concentrations. As a comparison, a human 80S ribosome has a mass of 4.2 MDa [78], corresponding to an expected buoyant mass of ~ 2.5 ag in an aqueous buffer. Considering similar working conditions to the polystyrene bead measurement, human ribosomes could be detected by SNR using a sub- μM sample concentration with mass resolution exceeding the attogram level.

3.3.3 Materials and Methods

Sample preparation

85 nm carboxylated polystyrene beads (Polysciences Inc., P/N 16688) were suspended in an aqueous buffer containing 100 mM NaCl, 350 μM SDS and 0.01% solid (w/v) NaN_3 . The buffer was selected to minimize the risk of clogging of the channel during

measurement and avoid particle aggregation. The beads were suspended at two final concentrations, namely 1.15×10^{13} and 7.67×10^{12} bead mL^{-1} (0.38% solid and 0.25% solid content in solution, respectively). Both samples were mixed with a small volume of $1.54 \mu\text{m}$ polystyrene beads (NIST certified size, Polysciences Inc., P/N 64060). These beads were used as standards for frequency/mass conversion calibration and to monitor the flow conditions of the sample during measurement. The final concentration of the reference beads was 5×10^6 particle mL^{-1} .

43 nm carboxylated polystyrene beads (Polysciences Inc., P/N 15913) were suspended in pure Milli-Q water at a concentration of 9×10^{13} beads mL^{-1} (0.4% solid content in solution). A value of 1.05 g/cm^3 was considered for polystyrene density. As reference particles, 222 nm carboxylated PMMA nanoparticles (Phosphorex Inc., P/N MMA220) were added to the bead solution, at a final concentration of 1.5×10^9 beads mL^{-1} . These particles were used for mass/frequency calibration, considering a PMMA density of 1.19 g/cm^3 .

Before measuring, the solutions were ultrasonicated for ~ 1 minute to separate possible bead aggregates and to obtain a homogeneous distribution of particles in the volume.

MCS measurements

Mass measurements of the 86 nm polystyrene beads were taken with a double-paddle resonator with geometrical dimensions as reported in Sec. 2.3.1. The traces were recorded in a 750 Hz and 1 kHz bandwidth, and the average flow velocity varied between $\sim 0.6 \text{ mm/s}$ and $\sim 6 \text{ mm/s}$, which allowed reliable detection of the reference particle signatures. Experimental autocorrelation curves were fitted using the 20-compartment approximation presented before.

The 43 nm polystyrene beads were measured with a SNR device with cross-section dimensions $2 \times 0.4 \mu\text{m}^2$, presented in Sec. 2.3.2. The time-domain mass measurements were taken in a 500 Hz bandwidth, to reduce the frequency noise to $\sim 200 \text{ mHz}$, while retaining enough data points for particle detection. Average sample flow velocity was $\sim 1 \text{ mm/s}$. The autocorrelation curves were calculated using a 3-compartment approximation.

Data treatment followed the procedure presented in Sec. 2.5.2.

Chapter 4

Size characterization by MCS

In the previous chapter, correlation analysis of the time-domain mass signal was used to extend the detection range of the SMR devices up to five orders of magnitude below the single-particle detection limit. However, the analysis only focused on the amplitude of the MCS signal. Information contained in the temporal behavior of the curve could not be analyzed using the compartment approximation of the fit function. In this chapter, a model that includes finite size effects and diffusion of the particles in the channel is derived and integrated in the MCS fit function to extract particle size information [21].

4.1 Theory

Pressure driven laminar flows present a non-uniform velocity profile in the cross-section and particles move at different velocities according to their radial positions [79, 80]. This generates a distribution of residence times of the particles in the resonator, which manifests as a distribution of temporal extensions of the particle signatures in the resonance frequency trace (see Eq. 2.13 for the description of particle signature).

The residence time distribution (RTD) of the sample in the resonator has a strong dependence on flow velocity: faster flows result in smaller average times in the resonator. Furthermore, particle size influences the shape and the width of the RTD by two mechanisms: first, particles diffuse in the cross-section while flowing in the embedded channel and vary their advection velocity as a result of changes in radial position.

Second, their finite size also precludes the particles from closely approaching the channel walls, effectively excluding the particles from the slowest regions of the velocity profile [77]. Therefore, measuring the RTD of a sample flowing in a channel of known dimensions can be used for the characterization of particle size [81]. Figure 4.1 shows the expected MCS signals for particles of different diameters. Samples with compact RTDs, such as large particles with size comparable to the channel cross-section or particles with high diffusivity, have correlation signals corresponding to, approximately, a flat flow profile in the channel; on the contrary, for samples with wide RTDs, the MCS curve is a long-tailed function due to the slow moving particles near the channel walls. Finally, the interplay of convection and diffusion affects the MCS shape, as particles have more time to diffuse in the cross-section when the average flow speed is slow.

A model describing the particle transport in the resonator at different flow velocities

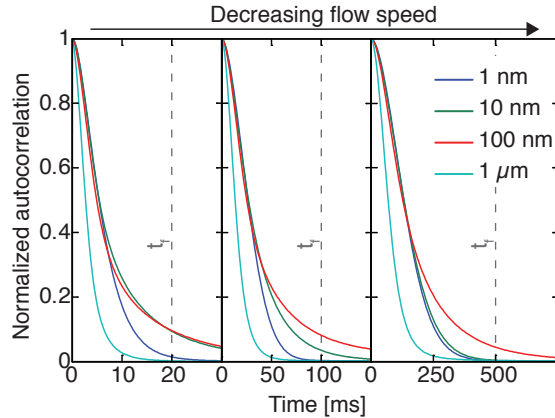


Figure 4.1: Expected mass correlation signals for particles of various sizes subjected to three different flow rates in a SMR with cross-section dimensions of $3 \times 8 \mu\text{m}^2$. The average time spent by the fluid in the embedded channel is shown with the gray dashed line. Particles of 1 nm rapidly diffuse in the whole cross-section, hence sampling the whole velocity profile; they present a narrow velocity distribution as they tend to move at the average flow velocity. On the contrary, 10 and 100 nm particles diffuse more slowly, therefore presenting a wider velocity distribution. This results in long tails (long correlation times) in the autocorrelation because of the slow moving particles. However, as particles have more time to diffuse, i.e. flow velocity decreases, the slow moving objects diffuse towards regions of higher velocities and the tails in the autocorrelation reduce. Particles of size comparable to the cross-section (i.e. the $1 \mu\text{m}$ particles) are excluded from the slowest regions of the velocity profile and all move at similar velocities, because of the confinement in the center region of the channel. Reprinted from Modena and Burg [21].

is therefore of paramount importance for the correct interpretation of the autocorrelation shape.

Concentration fluctuations

The autocorrelation¹ of the time-domain mass signal is defined as

$$C(\tau) = \Delta f_p^2 \iiint_V \langle \delta c(x, y, z, t) \delta c(x', y', z', t + \tau) \rangle \times u(x)^2 u(x')^2 dx dy dz dx' dy' dz' \quad (4.1)$$

where Δf_p is the maximum frequency shift induced by a particle at the apex of the cantilever resonator, $u(x)$ is the deflection function of the cantilever (Eq. 3.11) and $\langle \delta c(x, y, z, t) \delta c(x', y', z', t + \tau) \rangle$ is the correlation function of the concentration fluctuations. Assuming that the correlation of the concentration fluctuations only depends on the time difference τ , Eq. 4.1 can be rewritten as

$$C(\tau) = \Delta f_p^2 \iiint_V \langle \delta c(x, y, z, 0) \delta c(x', y', z', \tau) \rangle \times u(x)^2 u(x')^2 dx dy dz dx' dy' dz'. \quad (4.2)$$

To calculate $C(\tau)$, it is necessary to describe the time evolution of the concentration fluctuations according to the convection diffusion equation

$$\frac{\partial \delta c}{\partial t} = D \left[\frac{\partial^2 \delta c}{\partial x^2} + \frac{\partial^2 \delta c}{\partial y^2} + \frac{\partial^2 \delta c}{\partial z^2} \right] - U(y, z) \frac{\partial \delta c}{\partial x} \quad (4.3)$$

¹The function $C(\tau)$ is called ‘autocovariance’ in statistics; however, in signal processing it is commonly referred to as ‘autocorrelation’, despite the missing normalization factor. This latter convention will be used in the text, as stated previously on page 38.

where D is the diffusion coefficient of the particles and $U(y, z)$ the velocity profile defined in Eq. 3.6. The initial and boundary conditions are [76]

$$\delta c(x, y, z, 0) = \delta(x)\Phi(y, z) \quad (4.4)$$

$$\left. \frac{\partial \delta c}{\partial y} \right|_{y=-b, b} = 0 \quad (4.5)$$

$$\left. \frac{\partial \delta c}{\partial z} \right|_{z=-h, h} = 0 \quad (4.6)$$

$$\lim_{x \rightarrow \infty} \delta c = \lim_{x \rightarrow \infty} \frac{\partial \delta c}{\partial x} = 0 \quad (4.7)$$

where $\Phi(y, z) = c_0$ (for $|y| < (b - r_p)$ and $|z| < (h - r_p)$, with r_p the particle radius) is the initial uniform distribution over the cross-section and c_0 the average concentration of particles.

Following the procedure of Doshi *et al.* [76], it is convenient to construct a solution for the concentration integrated over the cross-section

$$\delta c_m(x, t) = \iint_A \delta c(x, y, z, t) dy dz \quad (4.8)$$

where A is the cross-section area. Eq. 4.8 can be easily integrated in the correlation function, since the sensitivity profile of the cantilever only depends on the axial direction. Eq. 4.2 thus becomes

$$C(\tau) = \Delta f_p^2 \iint_0^{2L} \langle \delta c_m(x, 0) \delta c_m(x', \tau) \rangle u(x)^2 u(x')^2 dx dx'. \quad (4.9)$$

Although there is no complete analytical solution for the problem described in Eq. 4.3-4.7, approximate solutions for $\delta c_m(x, t)$ valid for different regimes can be constructed. In the literature, the special case of point-like particles in channels of circular cross-sections has been discussed extensively [82]. This situation, however, is seldom encountered in microfluidics, as rectangular cross-sections are more easily obtained by micro-fabrication techniques and particle size can be comparable to the channel dimensions. The remainder of this section will describe an approximation for $\delta c_m(x, t)$ that covers, for the first time, the entire range of experimental conditions relevant for correlation measurements in micrometer and sub-micrometer fluidic channels.

As diffusion in the radial direction affects the sample dispersion, it is useful to define a dimensionless time parameter

$$\tau_D = \frac{D t}{a^2} \quad (4.10)$$

to quantify the radial average diffusion of the particles. Here, t is the dimensional time and a is the characteristic channel dimension (e.g. the channel radius or, for high aspect ratio rectangular channels, the minimum cross-section dimension).

Different regimes for the dispersion of the particles in the channel can be identified: for $\tau_D \ll 1$, particles do not diffuse considerably and follow their streamline. This situation will be defined as “advection regime”; for $\tau_D > 1$, the radial diffusion of the particles is larger than the cross-section, i.e. particles have sampled the entire flow profile. As this regime was first investigated by Taylor for channels of circular cross-section [79], it is usually referred to as “Taylor regime”; for $0 < \tau_D < 1$, the intermediate transition from the advection to the Taylor regime, diffusion is not negligible, however it is yet not sufficient to narrow the sample velocity distribution.

Once the particle behavior for $\tau_D \ll 1$ and $\tau_D > 1$ is known, the concentration profile at any time can be interpolated by a weighted sum of the limiting cases [83] as

$$\delta c_m(x, t) = A(t) \cdot \delta c_{mA}(x, t) + (1 - A(t)) \cdot \delta c_{mT}(x, t) \quad (4.11)$$

where $\delta c_{mA}(x, t)$ and $\delta c_{mT}(x, t)$ denote the concentration profile in the advection and Taylor regime respectively, and $A(t)$ is a time-dependent amplitude factor.

Assumptions

The following assumptions are made for the derivation of the model:

- particles move at the velocity of their center of mass (Fig.4.2a);
- the flow is a fully-developed laminar flow and particles do not affect the velocity profile in the channel;
- the embedded channel is approximated as a straight channel with cross-sectional area $2b \times 2h$ and length $2L$ (Fig.4.2b).

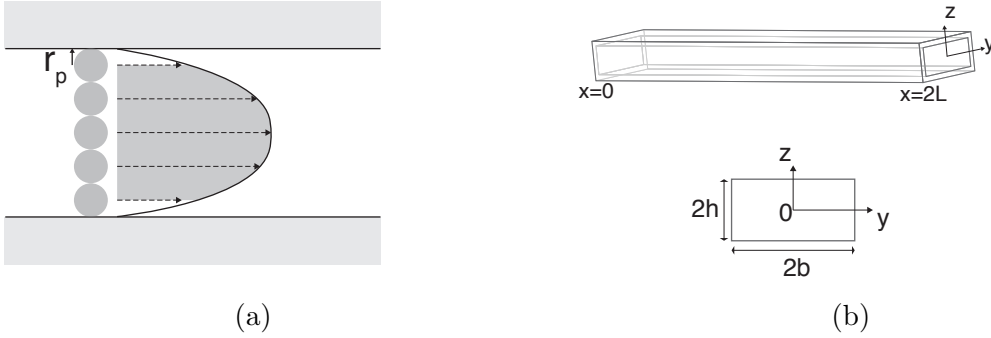


Figure 4.2: Assumptions for the derivation of the axial dispersion model: a) the solid black line represents the laminar flow profile in the channel. Particles move at the fluid velocity at their center of mass (dashed lines). The finite-size of the particles precludes them from approaching the channel walls at a distance smaller than the particle radius r_p . The gray area shows the accessible portion of the velocity profile; b) the embedded channel is approximated by a linear geometry. The channel is parallel to the x -axis and measures $2L$, with the position $x = L$ corresponding to the point of greatest deflection of the resonator. The cross-section has dimensions $2b \times 2h$ and lies in the yz -plane. Reprinted from Modena and Burg [21].

4.1.1 Taylor regime

This regime occurs for $\tau_D > 1$, when particles have sampled, on average, the entire velocity profile. This situation was first described by Taylor [79] and Aris [80] for round cross-section channels, showing that a plug of particles assumes a Gaussian distribution in the axial direction with a time-dependent variance. This axial concentration profile occurs regardless of the original radial distribution [80]. It was later demonstrated that this solution applies to channels of arbitrary cross section shape, and that channel geometry directly affects the variance of the particle axial distribution [84].

For point-like particles flowing in a channel of rectangular cross-section, a solution for $\delta c_m(x, t)$ was derived by Doshi *et al.* [76] and is given by

$$\delta c_{mT}(x, t) = c_0 V \frac{\exp \left[-\frac{(x - U_{avg}t)^2}{4\bar{k}(t)t} \right]}{\sqrt{4\pi\bar{k}(t)t}}. \quad (4.12)$$

The profile follows a Gaussian distribution, moving at the average flow velocity U_{avg} . The parameter $\bar{k}(t)$, controlling the variance of the distribution, is the time-averaged

dispersion coefficient and is defined as

$$\bar{k}(t) = \frac{1}{t} \int_0^t k(t') dt'. \quad (4.13)$$

This parameter contains information on the particle diffusion coefficient D and channel dimensions. The dispersion coefficient, $k(t)$, can be approximated as the sum of the dispersion caused by the velocity variations in the horizontal and vertical directions. Considering a channel of aspect ratio $\beta = h/b$, it is defined as [76]

$$k(t) = D \left[1 + \left(\frac{U_{max}h}{D} \right)^2 (K_{horiz}(t) + K_{vert}(t)) \right] \quad (4.14)$$

where

$$K_{horiz}(t) = \sum_{m=1}^{\infty} B_m^2 \left(1 - e^{-\frac{m^2 \pi^2 t D}{b^2}} \right) \quad (4.15a)$$

$$K_{vert}(t) = \sum_{n=1}^{\infty} B_n^2 \left(1 - e^{-\frac{n^2 \pi^2 t D}{h^2}} \right) \quad (4.15b)$$

and

$$B_m = \frac{256(-1)^m}{\pi^6 m} \sum_{j=1,3,5}^{\infty} \frac{\tanh\left(\frac{j\pi}{2\beta}\right)}{j^3[j^2 + 4m^2\beta^2]} \quad (4.16a)$$

$$B_n = \frac{4(-1)^n}{\pi^3 n^3} + \frac{256(-1)^{n+1}\beta}{\pi^6 n} \times \sum_{j=1,3,5}^{\infty} \frac{\tanh\left(\frac{j\pi}{2\beta}\right)}{j^3(2n+j)(2n-j)}.$$

Corrections for particles of finite size

Because of their finite size, particles are excluded from the slowest regions of the velocity profile. The reduction in velocity distribution experienced by the particles affects both the average velocity of the sample and its dispersion [77]. Defining the particle radius r_p , the effective sample velocity can be calculated as

$$U_{eff} = \frac{1}{b'} \frac{1}{h'} \int_0^{b'} \int_0^{h'} U(y, z) dz dy \quad (4.17)$$

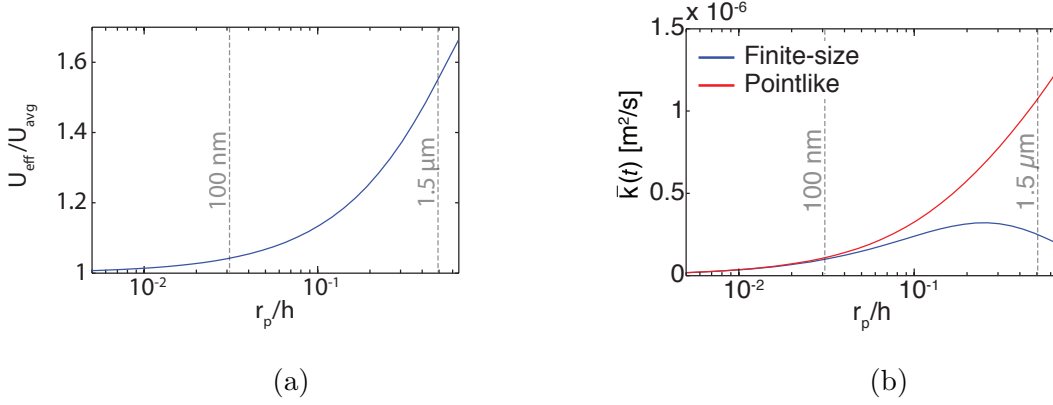


Figure 4.3: Comparison between the average velocity and dispersivity for pointlike and finite-size particles. a) Ratio between the average particle velocity and the average fluid velocity. Channel dimensions are $3 \times 8 \text{ }\mu\text{m}^2$; b) $\bar{k}(t)$ for pointlike and finite-size particles. The parameters considered for the plots are: $t = 1 \text{ s}$, cross-section dimensions $3 \times 8 \text{ }\mu\text{m}^2$ and flow velocity 1.3 mm/s . As the particle size becomes comparable with the channel dimension, the dispersion decreases as a consequence of the narrowing of the velocity profile experienced.

where $U(y, z)$ is the velocity profile described in Eq. 3.6, and $h' = h - r_p$ and $b' = b - r_p$ are the effective dimensions of the channel. From Eq. 4.17 it can be noticed that particles of finite size move, on average, at a velocity higher than the suspending fluid (Fig. 4.3a). This result follows from the assumption that particles move at the velocity of their center of mass (Fig. 4.2a). Despite the simplicity of the assumption, this approach approximates well the behavior of particles of different dimensions, as it is shown by the validation measurements taken on beads of different sizes (Sec. 4.3). Finally, excluding particles from the slowest regions of the velocity profile causes a reduction in the sample dispersion coefficient, as particles are subjected to a narrower velocity distribution. Following the results of James *et al.* for particles flowing in parallel plate conduits [77], the dispersion coefficient $k(t)$ for particles of finite size is calculated by modifying the horizontal and vertical contributions as

$$K'_{\text{horiz}}(t) = \sum_{m=1}^{\infty} B_m^2 \left(1 - e^{\left(-\frac{m^2 \pi^2 t D}{b'^2}\right)}\right) \cdot \left(1 - \frac{r_p}{b}\right)^6 \quad (4.18a)$$

$$K'_{\text{vert}}(t) = \sum_{n=1}^{\infty} B_n^2 \left(1 - e^{\left(-\frac{n^2 \pi^2 t D}{h'^2}\right)}\right) \cdot \left(1 - \frac{r_p}{h}\right)^6. \quad (4.18b)$$

The comparison between the time-averaged dispersion coefficient calculated for pointlike and finite-size particles is shown in Fig. 4.3b. Figure 4.4 shows the axial concentration profiles for particles of different diameters. The increase of sample velocity with particle size and the reduction in axial dispersion are clearly visible.

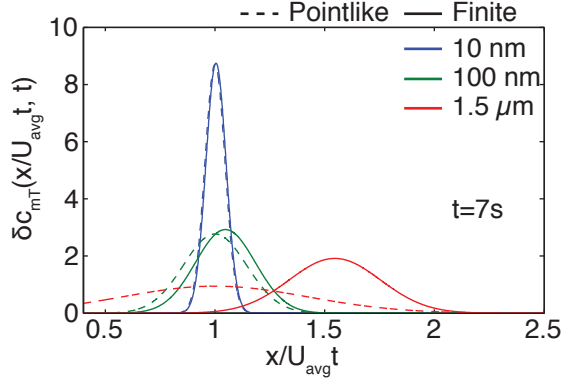


Figure 4.4: Comparison between the axial concentration profile of pointlike and finite-size particles of different diffusivity injected as a concentrated plug at $t = 0$. The channel dimensions are $3 \times 8 \mu\text{m}^2$, flow velocity is $\sim 1.3 \text{ mm/s}$ and the profiles have been calculated for $t = 7 \text{ s}$ ($\tau \approx 1$ for the $1.5 \mu\text{m}$ particles). The solid curves show the distribution for finite-size particles calculated with the corrections derived for U_{avg} and $k(t)$; the dashed curves depict the concentration distribution for pointlike particles with equal diffusivity. While the average sample velocity increases with the particle size, the variance follows a non-monotonic behavior, caused by the narrowing of the sample velocity distribution due to the increase of the particle diameter. The results are normalized with normalization factor $U_{\text{avg}} \cdot t$.

4.1.2 Advection regime

For $\tau_D \ll 1$, particles present small diffusion lengths and a uniformly distributed sheet of particles disperses according to the velocity profile in the channel. To describe this situation, a compartment approximation similar to the solution presented in the previous chapter (page 42) can be used. However, the model derived here is more general and becomes asymptotically more accurate with increasing number of compartments.

Plane Couette flow approximation

By approximating the velocity profile as composed of M regions of linearly varying flows, each compartment can be approximated by plane Couette flow. The dispersion

coefficient for each stream can be calculated as [85]

$$k_{Ai} = D \left[1 + \frac{1}{30} Pe_i^2 \right] \quad (4.19)$$

where $Pe_i = \Delta U_i w / D$ is the Péclet number in the compartment $i = 1, 2 \dots M$ and $w = \sqrt{4bh/M}$ is the effective size of the compartment. The size w is chosen such that the velocity profile in the compartment can be approximated by a linear function. ΔU_i represents the velocity variation with respect to the average speed U_i in the compartment, causing sample dispersion. Using this approximation, the axial concentration profile can be expressed by a mathematical description similar to the solution obtained for $\tau > 1$. Here,

$$\delta c_{mA}(x, t) = \frac{c_0 V}{M} \sum_{i=1}^M \frac{\exp \left[-\frac{(x-U_i t)^2}{4k_{Ai} t} \right]}{\sqrt{4\pi k_{Ai} t}} \quad (4.20)$$

where the distribution in each stream is described by a Gaussian function moving at the velocity U_i and variance proportional to k_{Ai} . Fig. 4.5 shows the mean velocities and the respective distribution variances in each compartment. At the center of the cross-section, the dispersion coefficients present a minimum as the velocity profile is almost flat; moving toward the channel walls corresponds to steep variations of the velocity

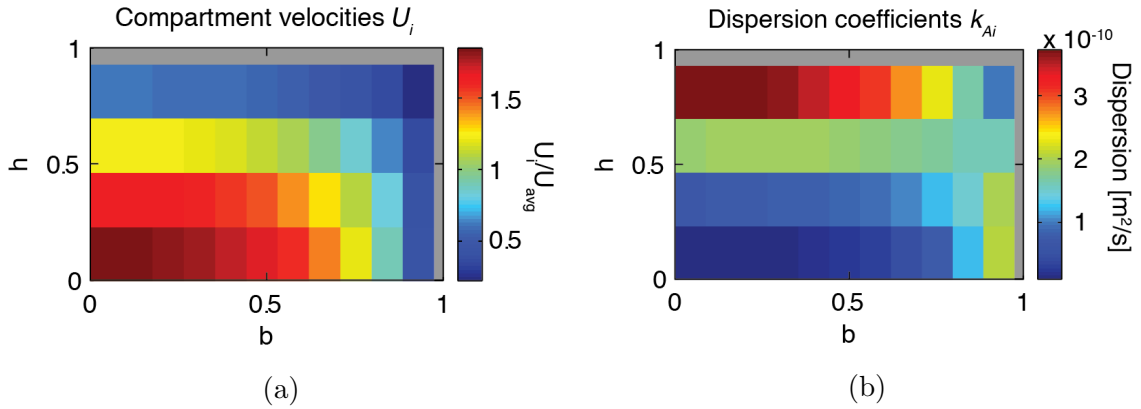


Figure 4.5: The color maps show the average velocity U_i (a) and the dispersion coefficient k_{Ai} (b) per compartment. The calculations are done for a sample of 200 nm particles flowing in a $3 \times 8 \mu\text{m}^2$ channel, at an average fluid velocity of 1.3 mm/s. The dispersion coefficient shows a minimum at the center of the channel, where the velocity profile is almost flat. The gray regions show the excluded portion of the profile because of the finite size of the particles. Because of the symmetry of the profile, one quarter of the cross-section is represented. The position (0, 0) identifies the center of the channel.

profile, as shown by the large differences in mean velocities of the compartments and by the increase in k_{Ai} .

Corrections for particles of finite size

The finite size of the particles is taken into account by excluding particles from the portions of the cross-section not accessible to them. The compartment approximation is then applied over the region

$$-b' \leq y \leq b' \quad (4.21a)$$

$$-h' \leq z \leq h' \quad (4.21b)$$

where b' and h' are the effective channel dimensions. Fig. 4.6 shows the approximated axial distribution obtained by Eq. 4.20 and Eq. 4.21.

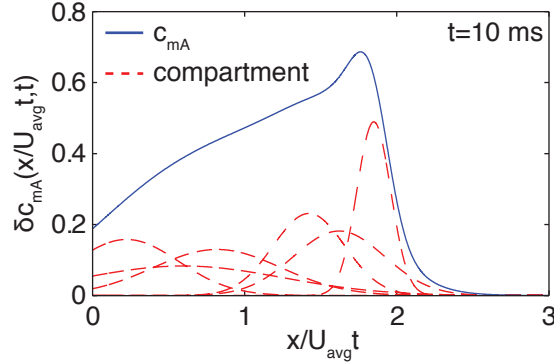


Figure 4.6: The plot shows the axial concentration profile of a plug of 200 nm particles flowing in a channel of $3 \times 8 \mu\text{m}^2$ cross-section at $t = 10 \text{ ms}$ ($\tau \approx 0.003$), flow velocity 1.3 mm/s. The results are normalized by $U_{avg} \cdot t$. The blue line corresponds to the concentration profile, the red dashed curves show six of the compartment contributions. For clarity of presentation, the compartment distributions have been rescaled so that $\sum_i \delta c_{mi}(x/U_{avg}t, t) = 1$. Fast moving streams at the center of the channel present a lower dispersion compared to the slower streams close to the channel walls, as shown in Fig. 4.5.

4.1.3 Concentration dispersion model

A combination of the solutions for $\tau_D \ll 1$ and $\tau_D > 1$ can be used for the description of the axial concentration profile at any time [83] by using an expression of the form

$$\delta c_m(x, t) = A(t) \cdot \delta c_{mA}(x, t) + (1 - A(t)) \cdot \delta c_{mT}(x, t) \quad (4.22)$$

with δc_{mA} defined in Eq. 4.20 and δc_{mT} in Eq. 4.12. $A(t)$ is a time-dependent weighing factor enabling the transition from the advection to the Taylor regime. Defining

$$A_h(t) = \frac{1 - \exp[-9Dt/b'^2]}{9Dt/b'^2} \quad (4.23a)$$

$$A_v(t) = \frac{1 - \exp[-9Dt/h'^2]}{9Dt/h'^2}, \quad (4.23b)$$

the dispersion coefficients in the horizontal and vertical dimensions (see Eq. 4.15) tend to their steady state values as, approximately, $1 - A_h(t)$ and $1 - A_v(t)$, respectively. The factor 9 in the equation derives from the symmetry planes in the velocity distribution for a rectangular cross-section channel [86]. b' and h' correspond to the effective channel dimensions, defined before.

Additionally, $A(t)$ depends on the aspect ratio β of the channel, since the velocity profile does not vary uniformly along the two dimensions. Considering these requirements, the transition coefficient is defined as follows:

$$A(t) = \beta \cdot A_h(t) + (1 - \beta) \cdot A_v(t) \quad (4.24)$$

The variation of the transition coefficient with channel aspect ratio and particle size is shown in Fig. 4.7. It can be noted that, as $\beta \rightarrow 0$, the transition factor only depends on the smaller cross-section dimension.

With Eq. 4.24, Eq. 4.22 can be used to describe the axial concentration profile of a plug of finite-size particles flowing in a channel of rectangular cross-section at any time.

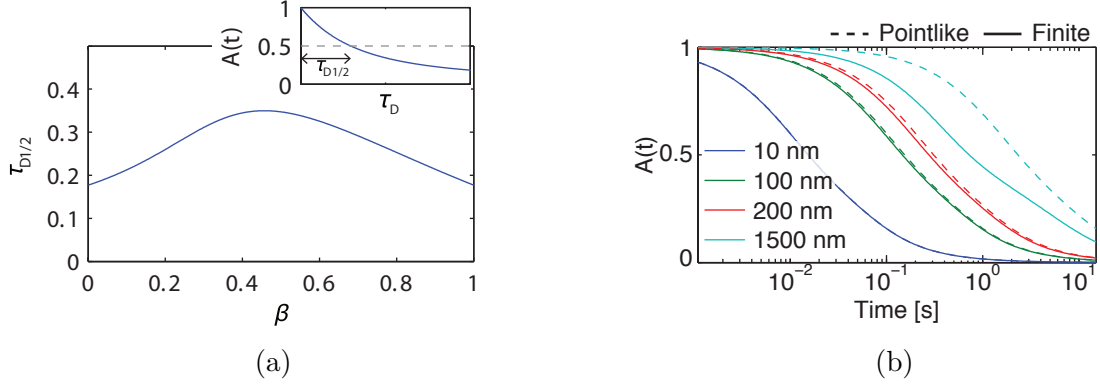


Figure 4.7: a) Time to reach $A(t) = 1/2$ as a function of the channel aspect ratio β . The inset shows how $\tau_{D1/2}$ is calculated. As $\beta \rightarrow 0$, the minimum channel dimension dominates and the behavior resembles that of a square channel. Time is normalized as $\tau_D = Dt/h^2$; b) transition coefficient for particles of different sizes flowing in a SMR channel ($3 \times 8 \mu\text{m}^2$). In normal experimental conditions (particle average time in the channel $t \sim 100$ ms), τ_D is in the transition from the advection to the Taylor regime. In contrast, SNR measurements are taken under Taylor dispersion behavior, due to the reduction in particle size and channel dimensions.

4.1.4 Effect of aspect ratio on MCS signal

Expected correlation curves for particles of different size flowing in rectangular microfluidic channels can be generated by inserting Eq. 4.22 in Eq. 4.9. Fig. 4.8 shows the effect of the channel aspect ratio on the MCS curves. The curves are calculated by keeping the channel height constant and varying the channel width. Square channels ($\beta = 1$) have the widest velocity distribution in the cross-section, with the maximum velocity being approximately twice the fluid average velocity; in parallel plate channels, instead, the velocity distribution extends from 0 to approximately 1.5 times the fluid average velocity. Because of the larger velocity distribution, channels with $\beta \rightarrow 1$ should be favored for particle size identification, while channels with $\beta \rightarrow 0$ should be chosen when sample dispersion is to be minimized.

4.2 Monte Carlo simulations

The model describing $\delta c_m(x, t)$ (Eq. 4.22) was tested using Monte Carlo (MC) simulations, to study the concentration dispersion under different flow velocities and to validate the goodness of the transition factor $A(t)$. Since finite-size effects can mask the

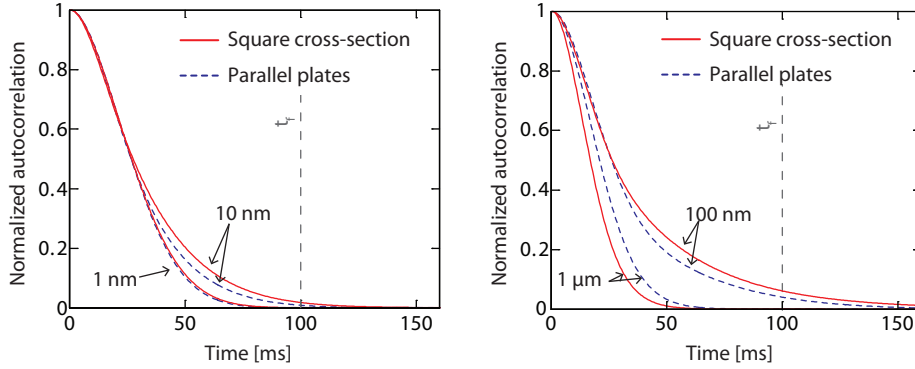


Figure 4.8: Channel aspect ratio effects on the autocorrelation signals from particles of different sizes. The expected curves are generated for channels of $3 \mu\text{m}$ height and with square and parallel plate cross-sections. The dashed vertical lines show the average residence time of the fluid in the channel. Square channels present larger velocity differences between portions in the cross-section, as the velocity distribution extends from 0 to approximately $2U_{avg}$, with U_{avg} the average velocity of the fluid. This corresponds to larger differences in sample average velocities according to the particle size and, in turn, to larger variations in autocorrelation shape and time extension. Channels with low aspect ratios ($\beta \rightarrow 1$) are therefore preferred for size identification by correlation analysis. Reprinted from Modena and Burg [21].

axial dispersion caused by particle diffusion and affect the transition between the advection and the Taylor regime, the simulations were performed in the limit of point-like particles. MC simulations are presented in terms of normalized time τ_D and distance

$$\chi = Dx/(U_{avg}a^2) \quad (4.25)$$

where the characteristic dimension a corresponds to the effective channel radius $a^2 = 4bh/\pi^2$. U_{avg} denotes the average fluid velocity and, following the point-like assumption, coincides with the average velocity of the particle plug.

4.2.1 Method

The MC simulation consist of 5000 non-interacting particles released at the entrance of a microfluidic channel and subjected to advection and diffusion. The magnitude of the advection per time step is $U(y_i, z_i) \cdot \Delta t$, where $U(y_i, z_i)$ is the fluid velocity at the particle center position and Δt the simulation time increment. Particles are free to diffuse in three dimensions, and the length of the diffusion vector per time step is

equal to $\sqrt{D\Delta t}$. The time increment Δt is chosen such that particles need, on average, more than 200 steps to transit through the simulated channel. MC simulations were calculated using a custom MATLAB script.

4.2.2 Results

Dispersion of point-like particles

The MC simulation at different time points for a channel of aspect ratio $\beta = 3/8$, as the one employed for the mass measurements, is shown in Fig. 4.9. In terms of dimensional units, the simulation corresponds to following the dispersion of a 50 nm particles in a $3 \times 8 \mu\text{m}^2$ channel, subjected to a flow of average velocity 1.4 mm/s, $Pe \approx 400$ (where $Pe = U_{avg}h/D$ is the Péclet number). As expected, Eq. 4.22 matches the simulation precisely only for $\tau_D \ll 1$ and $\tau_D > 1$, where models describing the axial concentration profile exist. However, also for values of $0.1 \leq \tau_D \leq 1$ the approximation developed here describes the behavior of the sample plug adequately, following its evolution from the early convective regime to the final Gaussian form.

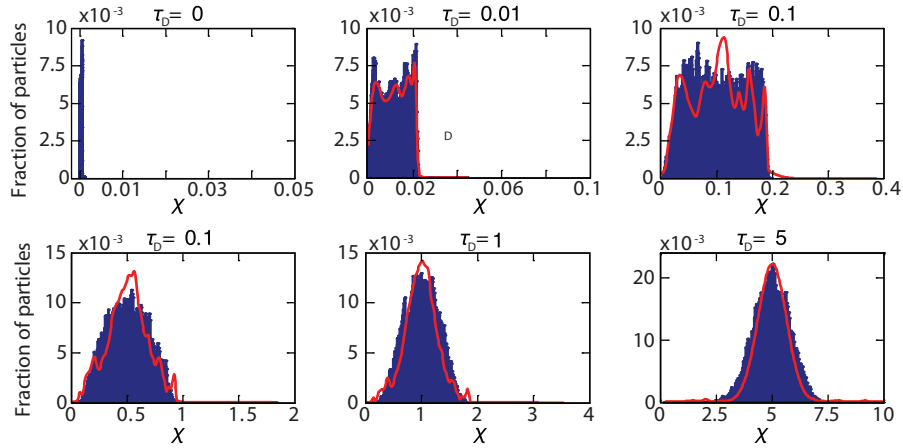


Figure 4.9: Monte Carlo simulation for a plug of 5000 point-like particles. At $\tau_D=0$, the particles are uniformly distributed in the cross-section at the entrance of the channel, $\chi = 0$. The particles are then subjected to an advection transport mechanism that follows the velocity profile in the cross-section. Particles are free to diffuse in three dimensions. The blue bars indicate the simulation results, while the red solid lines show the distributions obtained with the approximated model. For short times ($\tau_D \leq 0.1$) particles disperse according to the velocity profile; as time increases and particles change their velocities because of radial diffusion in the cross-section, the concentration profile tends to a normal distribution function moving at the average velocity of the fluid. Reprinted from Modena and Burg [21].

4.3 Experimental validation

Five monodisperse solutions of nanoparticles were characterized by MCS to test the validity of the sample dispersion model[21]. The nanoparticle diameters were 15 ± 1.5 nm (gold), 30 ± 3 nm (gold), 85 ± 6 nm (polystyrene), 210 ± 10 nm (polystyrene) and 490 ± 10 nm (polystyrene). A heterogeneous sample, composed of two populations of nanoparticles with different sizes, was also characterized with the MCS analysis. Each sample was measured at different flow velocity to detect the particle dispersion at different time scales and increase the resolution on size determination.

4.3.1 Materials and methods

Sample preparation

15 nm gold nanoparticles (0.005% w/v stock solution, Nanopartz Inc., P/N A11-15) suspended in pure DI water were measured with no dilution, at a concentration of 1.6×10^{12} part mL⁻¹; 30 nm gold nanoparticles (0.005% w/v stock solution, Nanopartz Inc., P/N A11-30) were suspended in pure milli-Q water at a final concentration of 1.02×10^{11} part mL⁻¹; 85 nm polystyrene (2.6% w/v stock solution, Polysciences Inc., P/N 16688) and 210 nm polystyrene beads (2% w/v stock solution, Invitrogen, P/N F8809) were suspended in an aqueous buffer containing 100 mM NaCl, 350 μ M SDS and 0.01% w/v NaN₃ and were measured at final concentrations of 2.28×10^{12} and 1.18×10^{11} part mL⁻¹, respectively. The purpose of the buffer was to minimize the risk of particle aggregation and interaction with the channel walls; 490 nm polystyrene beads (2.6% w/v stock solution, Polysciences Inc., P/N 18720) were suspended in pure milli-Q water at a final concentration of 4×10^8 part mL⁻¹.

A sample composed of a mixture of 93 nm polystyrene nanoparticles (1% w/v stock solution, Phosphorex Inc., P/N 105) and 490 nm polystyrene beads was prepared by diluting the stock solutions in pure milli-Q water. The final concentrations of the two populations were 5.7×10^{12} and 5.4×10^8 part mL⁻¹, respectively.

All samples were prepared fresh before each experiment and ultrasonicated for ~ 1 minute to reduce possible aggregation of the beads. To characterize the frequency/mass response of the device and monitor the flow velocity, 1.54 μ m NIST polystyrene beads

(Polysciences Inc., P/N 64040) were added to the solutions as reference particles, at a final concentration of 5×10^6 part mL^{-1} .

MCS measurements

Each sample was measured using a minimum of four different flow velocities to detect the dispersion behavior of the particles at different time scales. The average residence times in the resonator ranged from ~ 20 ms to ~ 200 ms and each mass trace was acquired for ~ 30 s to a few minutes, the acquisition time being limited by the stability of the flow during the detection. Figure 4.10 shows an example of a measurement taken at different flow velocities. The fit function of the MCS curves present two free parameters, namely particle size and curve amplitude. All curves taken at different flow velocities are fitted using a single size parameter to monitor the goodness of the dispersion prediction at different time scales. The magnitude of the fit curve, instead, is free to vary as small amplitude differences are expected between measurements.

Measurements were acquired using sampling rates of 1 kHz and 2 kHz.

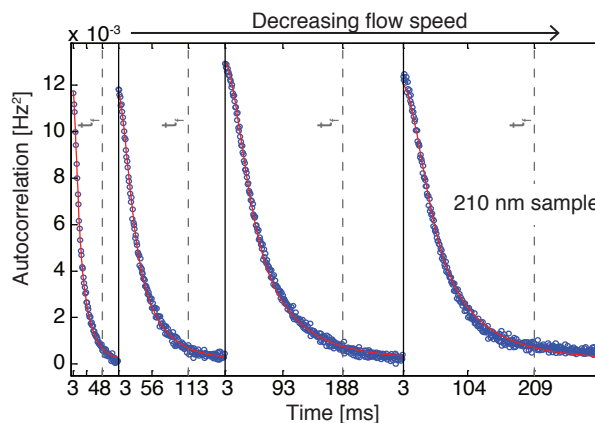


Figure 4.10: MCS signals for a 210 nm polystyrene sample (in blue) and best fit curves (in red), obtained by constraining the fitted particle size to be identical for all four curves. The average residence time of the fluid in the resonator is shown by the gray dashed lines, estimated from the reference particle signatures. The correlation curves change their shape according to the flow velocity, as particles have different time to diffuse in the cross-section. Reprinted from Modena and Burg [21].

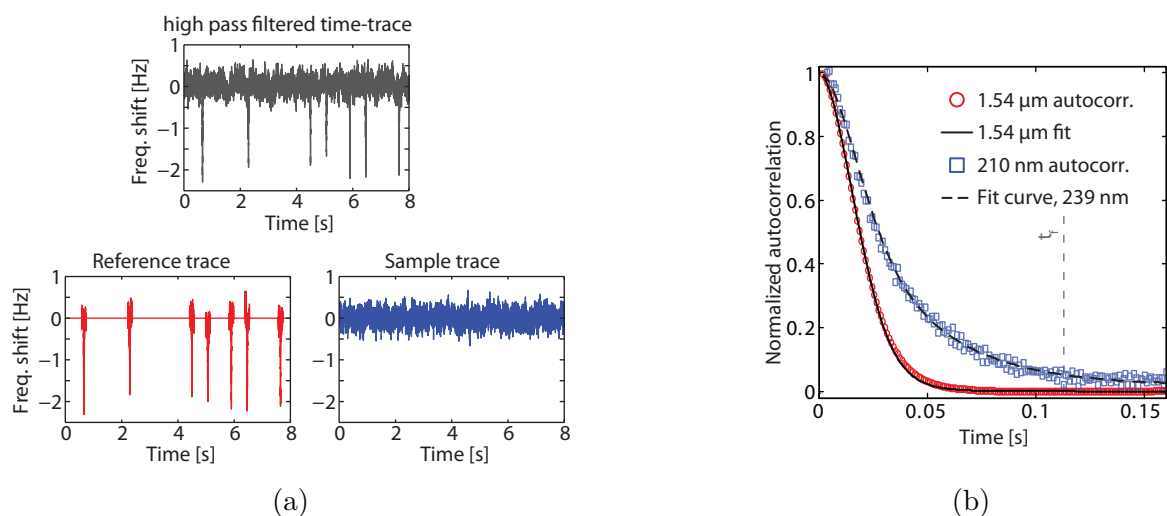


Figure 4.11: a) The high-pass filtered signal (top) is separated into two traces: a trace composed of only reference particles (in red) and a trace without detectable individual particle signatures (in blue), as presented on page 33. The reference trace is used both for mass/frequency conversion calibration and for estimating the flow velocity during the measurement; b) as the size of the reference particles is known, the fit of the autocorrelation curve (in red) can be used to measure the flow velocity during the acquisition. This information is then used to fit the sample curve (in blue), to estimate the particle size. The figures show a short excerpt of the time-trace and autocorrelation curves for a sample of 210 nm polystyrene beads, average flow velocity 1.2 mm/s.

Data analysis

Each measurement trace is separated in two signals: one composed exclusively of reference particle signatures and a second trace with the portions of the time-domain mass signal only containing fluctuations caused by the unknown sample (Fig. 4.11a). The reference signal is used for mass/frequency conversion calibration, as explained in Sec. 2.5.3, and for the estimation of the flow velocity, by fitting the autocorrelation curve for particles of known size. The flow velocity is then used during the correlation analysis of the unknown sample trace for estimating the particle size (Fig. 4.11b). Knowledge of the flow velocity is a fundamental prerequisite in the estimation of particle size from the MCS curve, as particles of different size may present similar dispersion behavior at different time scales.

Error estimation

A bootstrap algorithm [87] is used to estimate the uncertainty on the autocorrelation fit parameters. From the experimental time-domain mass trace, a pool of 500 pseudo time-traces are generated and their autocorrelations are independently analyzed, following the procedure described before. The uncertainties in particle size and curve amplitude estimation are calculated from the fit parameters found for the autocorrelation curves generated from the pseudo time-traces: the means of the respective fit values are taken as best fit parameters; the uncertainties on these estimations correspond to the standard deviations of the fit values found.

Due to the time correlation present in the data, the pseudo time-traces are generated according to a Stationary Bootstrap method [88], described as follows (Fig. 4.12): each pseudo time-trace is constructed by selecting blocks of random length from the original time-trace and combining them to generate a trace with a number of points equal to or higher than the original trace. The number of points per block is based on a geometric distribution. The average block length was set at ~ 10 s to avoid the disruption of the time correlation of the data. A uniform block length strategy could have been applied for the generation of the pseudo time-traces; however, the results obtained by using this simpler strategy may show a dependency on the block length. This situation is avoided by the geometric distribution of the block lengths[88].

4.3.2 Monodisperse populations

The analysis was tested on nanoparticles of different size and materials, namely gold nanoparticles of 15 ± 1.5 and 30 ± 3 nm in diameter and polystyrene beads of 85 ± 6 , 210 ± 10 and 490 ± 10 nm size. The 15, 30 and 490 nm samples were measured in pure milli-Q water, while the 85 and 210 nm beads were suspended in an aqueous buffer containing a small concentration of salt and surfactant, to reduce unwanted sample aggregation.

Size detection

The fits of the experimental autocorrelations show minimum residual errors for diameters of 37 ± 1 , 51 ± 2 , 109 ± 24 , 245 ± 40 and 537 ± 32 nm for the 15, 30, 93, 210

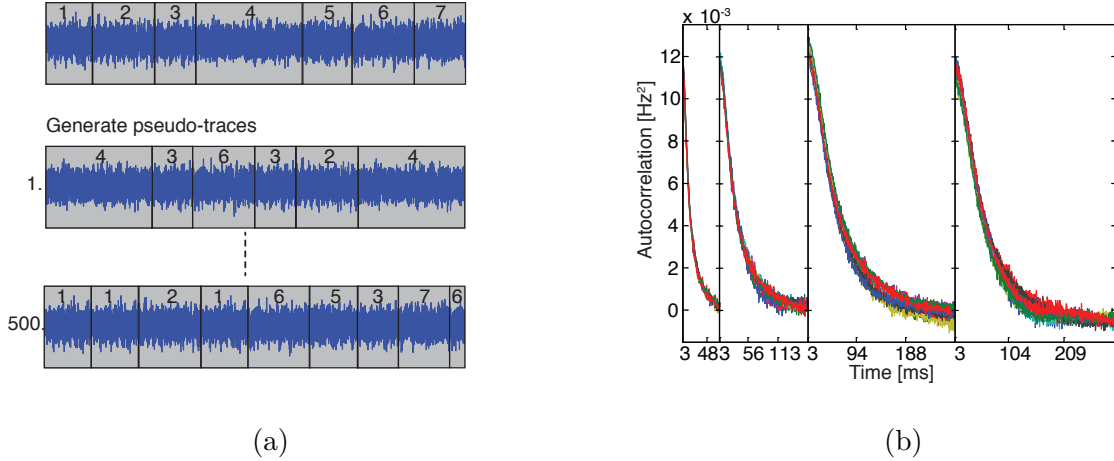


Figure 4.12: The bootstrap algorithm used for uncertainty calculation of the fit parameters. a) 500 pseudo time-traces are generated by combining blocks of random length of the experimental time-traces (top trace). The average block length corresponds to 10 s, not to disrupt the time correlation of the data within each block. The starting points of the blocks have uniform probability over the whole trace and data repetition is allowed in the pseudo time-traces; b) the pseudo time-traces are autocorrelated and independently analyzed. The figure shows 10 autocorrelations generated from the pseudo time-traces.

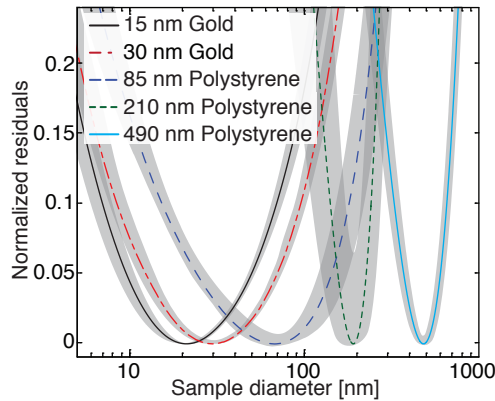


Figure 4.13: Normalized residuals after fitting the experimental data with test autocorrelation curves of different diameters. The residuals were offset to their minimum values, with 0 corresponding to the best fit obtained. The gray shaded areas shows the variability of the residual fit curve obtained by the bootstrap analysis. The legend reports the manufacturer reported sizes. Reprinted from Modena and Burg [21].

and 490 nm beads, respectively (Fig. 4.13). The uncertainties are calculated using the bootstrap method presented before. The estimation intervals account for different sources of measurement uncertainties, including the acquisition frequency noise and flow instabilities that might affect the size characterization. The results present

approximately a 25 nm overestimation of the particle sizes, possibly due to the approximation used in the model derivation and to tolerances in device dimensions. However, relative differences between particles can still be inferred from the analysis, showing that the samples under investigation ranged from few tens to hundreds of nanometers. The use of calibration particles for detecting the accuracy of the measurement could provide a solution for obtaining absolute size quantification during mass measurement. It is interesting to note that the model applies correctly for particles whose size is not negligible with respect to the cross-section dimensions, such as the 490 nm beads. Under the experimental conditions employed here, particles of this size do not diffuse considerably and characterization is based on the sample average velocity. Despite the simplistic approximations used for estimating the velocity distribution of finite-size particles, the model correctly predicts the average velocities of the samples. Finally, the largest estimation uncertainty is obtained for the 85 nm beads. Particles of size ranging from ~ 50 to ~ 150 nm present small diffusion lengths under typical measurement conditions, while the average velocity almost coincides with the average velocity of the fluid. Therefore, particle size identification cannot be based on diffusion, nor on sample average velocity, resulting in a large size uncertainty.

Comparison with DLS characterization

The beads were also characterized by Dynamic Light Scattering (DLS) at the same conditions. DLS measurements provide the average hydrodynamic radius of the particles and information on the polydispersity (Pd) of the sample.

The characterization returned average particle diameters of 17.2 nm (Pd 26%), 37.6 nm (Pd 14%), 66 nm (Pd 19%), 248 nm (Pd 23%) and 473 nm (Pd 10%) for the 15, 30, 85, 210 and 490 nm nanoparticles, respectively. Pd reports the percent polydispersity of the sample: for $Pd \leq 15\%$ the sample is considered monomodal and monodisperse, $15 < Pd \leq 30$ the sample is monomodal polydisperse (i.e. it might present low percentages of dimeric-trimeric species), while higher values corresponds to heterogeneous populations [89]. High values of polydispersity, likely corresponding to the presence of small aggregates of particles in solution, might be the cause of the relatively large uncertainties obtained in size determination with the MCS analysis. However, no direct correspondence between MCS and sample distribution can currently be inferred.

Mass characterization

Average information on particle mass can be estimated from the amplitude of the correlation analysis, as presented in Chapter 3. Inserting Eq. 3.1 in Eq. 3.16, the autocorrelation amplitude at $t = 0$ corresponds to

$$C(0) = \frac{1}{5} c_0 V_c \left(\Delta m_p \cdot \frac{\partial f}{\partial m} \right)^2 \quad (4.26)$$

where c_0 is the particle concentration, V_c the embedded channel volume, $\delta f/\delta m$ the mass responsivity of the device and Δm_p the average buoyant mass of the particles. As the sample concentration c_0 is known, the analysis allows the independent and simultaneous measurement of the mass and size of the particles (Fig. 4.14). The buoyant mass estimated from the MCS curve actually corresponds to $\sqrt{\langle \Delta m_p^2 \rangle}$ and it follows that, when dealing with samples presenting a large distribution of sizes, the estimated mass might be considerably different from the arithmetic mean mass. The estimated values of buoyant mass are 32 ± 3 ag, 184 ± 17 ag, 26 ± 2 ag, 0.43 ± 0.05 fg and 3.5 ± 0.3 fg for the 15, 30, 85, 210 and 490 nm particles, respectively. The uncertainty intervals reported include both the statistical error on the fitting of the correlation curves and the experimental uncertainty on the mass/frequency conversion. Systematic errors,

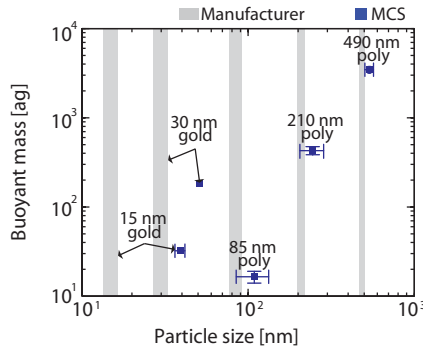


Figure 4.14: Buoyant mass and size of the particles measured by MCS. The manufacturer specifications are reported for comparison. Size estimations with the MCS method shows a deviation of approximately 25 nm from the manufacturer reported values, however relative size differences between particles can be detected by the analysis. The non monotonic behavior of the mass with particle size clearly shows that the samples under examinations were composed of different materials, with a large difference in density. Reprinted from Modena and Burg [21].

due to device tolerances or sample preparation, are not included. As a comparison, the detection limit for single-particle measurements with these devices corresponds to ~ 30 fg, considering a minimum signal-to-noise ratio of 3, a detection limit more than three orders of magnitudes higher than the mass of the 85 nm particles.

Although the absolute quantification of particle density is affected by the accuracy of the measurement, the non-monotonic variation of mass with particle sizes clearly indicates that the samples are composed of materials with a large density difference. The particle densities calculated from the size and mass estimations are 2.04 ± 0.30 g/cm³, 3.65 ± 0.56 g/cm³, 1.02 ± 0.02 g/cm³, 1.06 ± 0.03 g/cm³ and 1.04 ± 0.01 g/cm³ for the 15, 30, 85, 210 and 490 nm samples, respectively. As expected, the gold particles are strongly affected by the accuracy of the measurement, and present a much lower value compared to the theoretical density of bulk gold of 19.3 g/cm³; in contrast, a minor deviation is obtained for the larger polystyrene particles, whose estimated densities present good agreement with the expected density of polystyrene of 1.05-1.06 g/cm³.

Discussion

The uncertainty intervals on the estimated parameters, obtained with the bootstrap analysis technique, are intimately linked to the quality of the acquired data. Therefore, no direct inference on the distribution of particle size and mass can be done starting from the uncertainties of the fit parameters.

Furthermore, the mass values are estimated from the concentration of the sample in solution and from the volume of the microfluidic channel embedded inside the resonator. As a consequence, the analysis can be affected by systematic errors introduced by tolerances in device fabrication or in the estimation of the particle concentration in solution.

Density measurements of suspended particles by SMRs have already been presented in the literature: these measurement consisted in detecting the variations of buoyant mass of the particles when suspended in solutions of different densities [23, 24, 74]. Although this method can achieve very high resolution, this technique is based on the assumption that changes in solution do not alter the sample, a condition that cannot

always be fulfilled. Furthermore, density measurements of particles composed of heavy materials, such as gold nanoparticles, would be equally challenging when performed by buffer density variation: for the method to reach high resolution, the sample needs to be measured in solutions of density both lower and higher than the sample itself, a condition that cannot be met for metallic particles.

To conclude, detection of particle dispersion in the resonator enables the MCS method to characterize suspended particles in terms of mass, density and size, in a single experiment.

4.3.3 Heterogeneous samples

The results presented so far have focused on the analysis of monodisperse sample populations. However, the autocorrelation analysis may also provide more insight into the sample composition. To illustrate how information on size distribution can be inferred, characterization of a sample with a bimodal particle distribution is presented and discussed.

MCS signal and curve fitting

A heterogeneous sample composed of two monodisperse populations of beads, namely 93 nm and 490 nm polystyrene beads (manufacturer values), is analyzed with the correlation analysis method. Figure 4.15 shows the autocorrelation curves of the mass signals acquired at different flow velocities. The experimental curves are compared with the fits calculated for monodisperse samples of 93 and 490 nm and by assuming that both populations are present in the sample. A single population autocorrelation is not sufficient to describe correctly the experimental curves and a bimodal distribution follows better the time dependence of the curves. A least-squares method was used to find the superposition of the two particle autocorrelation functions that could best fit the experimental curves for all flow rates. Similarly to the size estimation procedure, the absolute amplitude of the fit function is free to vary between measurements, while a single value for the ratio of the two particle contributions in the correlation signal is used for all the curves.

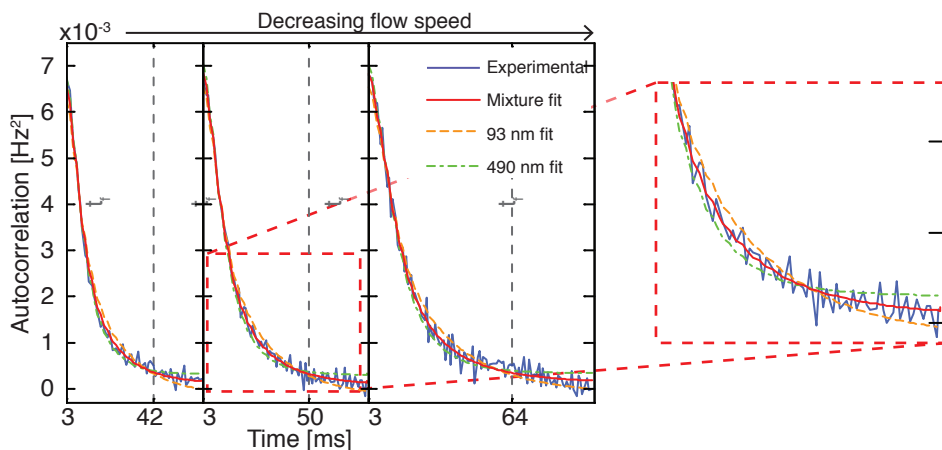


Figure 4.15: Autocorrelation curves for a sample composed of two different monodisperse populations of polystyrene beads, with diameters of 93 and 490 nm. The experimental curves are compared to the fit functions obtained assuming a monodisperse population (dash lines) or bimodal sample composition (solid red). This latter shows a better fit of the experimental curves. For clarity only three measurements are shown, with average flow velocities ranging from ~ 3 to ~ 4.5 mm/s. Reprinted from Modena and Burg [21].

Results and discussion

The fit procedure is applied to the autocorrelation curves of the generated pseudo time-traces to obtain the uncertainty intervals on the parameter estimations. The analysis returns a relative amplitude of the 93 nm sample contribution in the correlation signal of 0.4 ± 0.05 . As the total dissolved mass of the two samples is known (2.5 mg/mL) and assuming that the two particle populations have equal density, the absolute concentrations result in $(5.6 \pm 0.1) \times 10^{12}$ and $(4.1 \pm 0.9) \times 10^8$ particles mL^{-1} for the 93 and 490 nm particles, respectively. According to these results, the estimated particle density corresponds to 1.07 ± 0.01 g/cm³.

As for the analysis of the monodisperse samples, the uncertainty intervals do not take into account systematic errors, such as uncertainties on the particle radius or on the total solid content. These errors can cause large deviations of the calculated quantities and be the source of mismatch between the calculated and the expected values of densities and concentrations of the particles.

The measurement shows how the MCS signal can be an indicator of the polydispersivity of the particle population. However, an absolute quantification of the sample properties can be challenging when no prior knowledge of the sample is available.

Chapter 5

Applications of the MCS method

In this chapter, different applications of the Mass Correlation Spectroscopy method to samples of biological relevance are presented. These systems have been chosen as representative of the wide spectrum of biological questions that mass characterization by MCS method can help addressing. The analysis developed enable the label-free characterization of the sample in free solution, i.e. without requiring surface attachment of the sample as for quartz crystal microbalance (QCM) and surface plasmon resonance (SPR) characterization.

Four examples of applications of the correlation analysis will be shown: firstly, insulin aggregation is monitored from the pre-fibrillar aggregates in solution to the formation of mature fibrils of MDa average mass. Secondly, the correlation analysis is used to quantify the surface coatings of nanoparticles in solution. Both theoretical calculations and proof-of-concepts measurements of polystyrene beads coated by a protein layer are presented. Thirdly, proof-of-principle detection of ribosomes and of ribosome density is presented. The last example shows how the correlation analysis can be used in conjunction with other SMR characterization methods to provide information on flow rates during measurement.

5.1 Insulin aggregation kinetics

Protein aggregation was detected with the MCS method. The formation of aggregates in solution and their growth were characterized by quantifying the variation of correlation amplitude at different time points during the aggregation assay.

Mass characterization was also compared to ThT fluorescence detection of fibrils in solution, a technique commonly used to follow the aggregation kinetics of amyloid aggregates. With respect to the fluorescence indicator, MCS characterization shows superior detection in the early stages of aggregation, when amorphous aggregates are formed in solution. Precise estimates of the average aggregate mass and concentration at different time points can be obtained, proving that MCS can provide valuable insights on the formation of protein aggregates.

5.1.1 Protein aggregation

Over 40 human diseases are associated with protein conversion from their soluble functional state into insoluble fibrillar aggregates, referred to as amyloid fibrils [90, 91]. Despite the wide diversity between the predominant proteins involved in the aggregation process in each disease, the amyloid fibrils formed during the process present similar characteristics, such as extensive β -sheet structures [92].

Globular proteins sample different native-like conformations via thermal fluctuations. The exposition to solvent of hydrophobic residues, normally concealed in the inner part of the folded protein, can greatly increase the chance of intermolecular interactions, leading to the formation of protein aggregates in solution [91, 93]. Furthermore, mutations or modifications of the sample environment can also promote protein aggregation by shifting the population equilibrium towards a higher concentration of unfolded or partially unfolded protein conformations [91]. Figure 5.1 depicts the main steps in the pathway for amyloid fibril formation, showing also the major off-pathway products that can occur during fibrillogenesis [94].

A fibril formation pathway similar to that presented in Fig. 5.1 also applies to intrinsically disordered proteins, but for a main difference: as a consequence of the lack of a naturally stable structure, fibrillogenesis usually begins with the formation of a partially folded protein conformation. This non-native state is then responsible for the

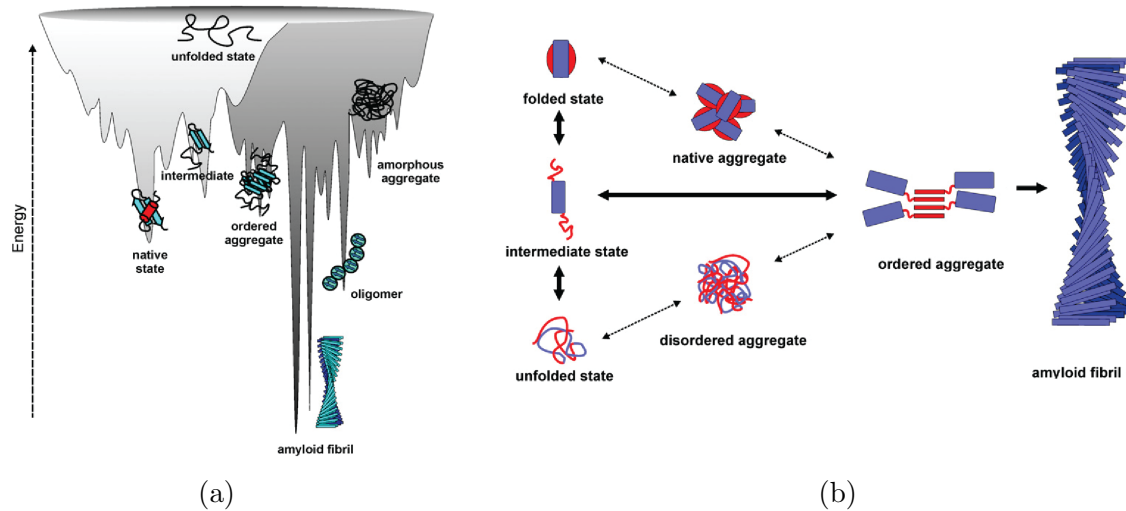


Figure 5.1: a) Protein energy landscape. In light gray, the protein different native-like conformations; in dark gray, the protein aggregates. The intermolecular contacts increases the ruggedness of the protein energy profile; b) protein aggregation pathway, from the folded native state to insoluble amyloid fibrils. Several off-pathway stable conformations can occur during aggregation, as a consequence of the energy landscape. Images are modified from Jahn and Radford [93]

specific intermolecular interactions necessary for the subsequent protein oligomerization and fibrillation [95].

5.1.1.1 Insulin as model protein

Insulin was selected as model protein for the characterization of the aggregation process by MCS. Insulin is a peptide hormone of 51 amino acids, consisting of two chains of 21 and 30 residues linked by two disulphide bridges. The monomer is the active form of the protein. However, insulin is known to associate in dimers, tetramers and hexamers, this latter being the preferred form for storage in the pancreatic vesicles [96].

Insulin aggregation occurs as side effect in the sub-cutaneous treatment of diabetes patients [97]. *In vitro*, aggregation is promoted by exposing the protein to denaturing conditions, including high-temperature, acid environments and high sample concentration [96, 98, 99].

5.1.1.2 Amyloid formation detection by ThT fluorescence

Thioflavin-T (ThT) is a fluorescent dye that specifically binds to stacked β -sheets, therefore presenting high selectivity towards amyloid fibrils [100]. Upon binding, ThT experiences both a shift in excitation (from 385 nm to 450 nm) and emission maxima (from 445 nm to 482), and a dramatic increase in fluorescence intensity, making this dye a very sensitive reporter of fibrillation in solution [101]. Fig. 5.2 shows the ThT emission increase caused by the binding with amyloid fibrils and the typical fluorescence intensity behavior during the aggregation process. ThT fluorescence intensity scales with the amount of fibrils in solution, while being independent of the number or length of the fibrils [102]. The lag phase in the fluorescence intensity increase shows the absence of mature fibrils, although it does not report any information on the presence of amorphous aggregates in solution.

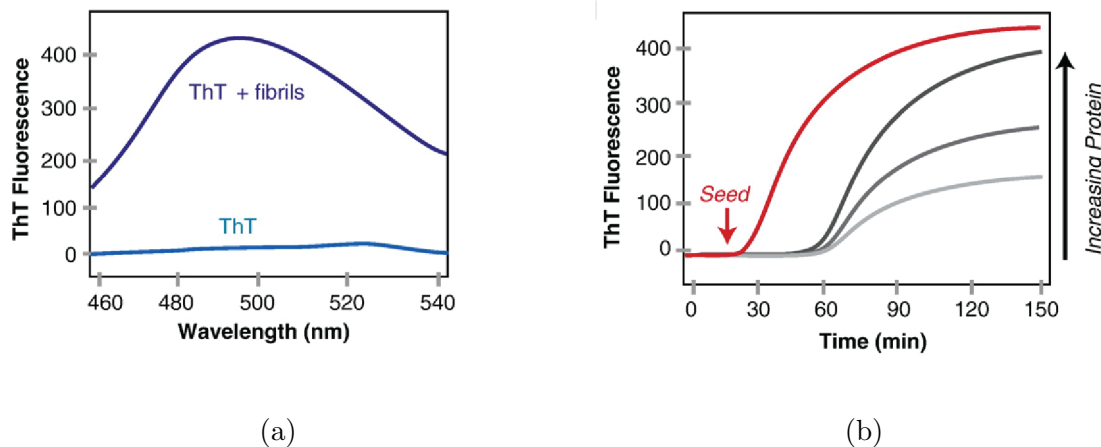


Figure 5.2: a) ThT experiences an increase in fluorescence emission of several orders of magnitude upon binding to amyloid fibrils. The figure shows the emission maximum, centered around 485 nm; b) ThT fluorescence increase during an aggregation assay. Increase in fluorescence emission occurs during amyloid fibril elongation, while the preceding lag phase corresponds to the formation of pre-fibrillar aggregates in solution. Addition of impurities or fibril fragments in solution can generate fibril nucleation centers and dramatically shorten the lag phase. ThT intensity scales with protein concentration. Figures are reprinted with permission from Biancalana and Koide [102]. Copyright 2010 Elsevier B.V.

5.1.2 Mass characterization of insulin aggregates

A solution of 5 mg/mL insulin dissolved in a glycine-HCl buffer (pH=2.3) was monitored for 8¹/₂ hours, to detect the formation of protein aggregates and their conversion into amyloid fibrils. Quantification of the MCS amplitude showed an increase in average mass of the aggregates from ~75 kDa to mature fibrils of ~15 MDa in the course of the aggregation assay.

5.1.2.1 Insulin aggregation

During the 8¹/₂ hours of aggregation, the MCS signal experienced an increase of over two orders of magnitudes, as a result of the conversion of insulin from a mostly dimeric state into mature amyloid fibrils. The increase of the correlation signal is shown in Fig. 5.3, where MCS curves of the insulin solution registered at different time points are compared. The amyloid fibril formation is also confirmed by ThT fluorescence measurements, presented in Fig. 5.4. The fluorescence intensity shows the typical nucleation-polymerization behavior, with an initial lag phase where the fibril nuclei are formed. Here, ThT characterization is blind, because of the absence of fibrils in solution, and no information on the state of aggregation can be inferred [103]. Nucleation is followed by a fibril elongation phase, where the ThT signal shows a rapid increase in intensity. In contrast, the MCS signal directly depends on the average aggregate mass

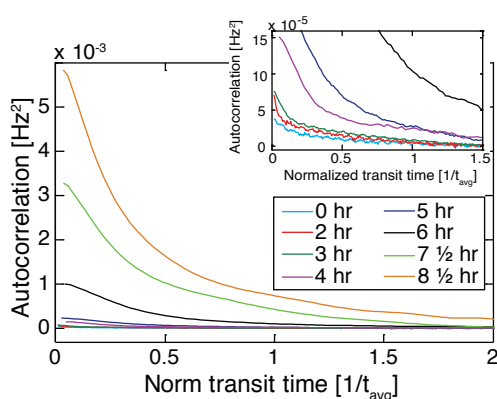


Figure 5.3: The figure shows the MCS signals of the insulin solution measured at different time points. The increase of correlation amplitude with time is a clear indicator of the formation of aggregates in solution. Curves are normalized to the average estimated fluid velocity for comparison. A triangular 5 points smoothing was applied on the curves, to improve figure clarity. Reprinted from Modena *et al.* [19].

and concentration, regardless of the structure of the aggregates. Increase in correlation amplitude can be observed in the lag phase of the reaction, indicating the formation of pre-fibrillar aggregates in solution during the lag-phase. Small oligomers are known to form during the early stages of aggregation, acting as nuclei and building blocks of the subsequent fibril formation [104]. The first aggregate products are of particular interest because of increasing proofs that these species might play an important role in the pathogenesis of amyloid related diseases [90]. Therefore, characterization of the early aggregation stages is of fundamental importance in the study of amyloid kinetics. In contrast to ThT fluorescence characterization, MCS measurements do not present an intrinsic blind phase and lack of resolution at early stages would only depend on the sample mass and concentration.

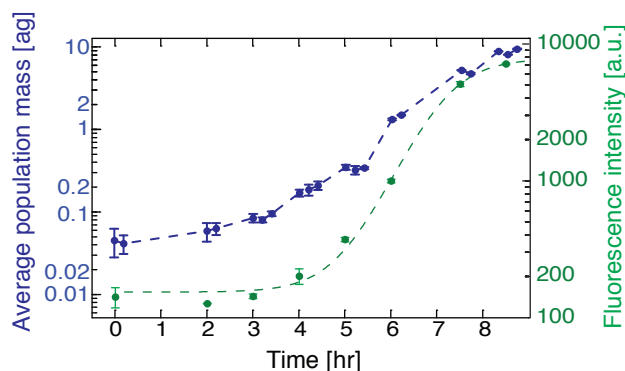


Figure 5.4: Average aggregate mass increase (in blue) during the aggregation process. The blue dashed line is shown to guide the eye. The mass increase is compared to the recorded ThT fluorescence intensity (in green) at the different time points, showing that the formation of first oligomeric aggregates occurred during the blind phase of the fluorescence measurement. The ThT data are fitted with a sigmoidal, showing the typical nucleation-elongation behavior with a lag phase of ~ 3.5 hours. Reprinted from Modena *et al.* [19].

5.1.2.2 Average mass of aggregates in solution

From the MCS signal, it is possible to estimate an average mass of the aggregates for each time point, defined as

$$m_{avg} = \frac{\langle m^2 \rangle}{\langle m \rangle}. \quad (5.1)$$

The average mass values m_{avg} are calculated by solving the system of equations composed of the MCS amplitude $\langle \hat{\beta}_1 \rangle$, the total amount of protein in solution T and the

definition of buoyant mass $\langle \Delta m \rangle$

$$\left\{ \begin{array}{l} \langle \hat{\beta}_1 \rangle = \frac{1}{5} \left(\langle \Delta m_i^2 \rangle \left(\frac{\delta f}{\delta m} \right)^2 \right) c_i V \\ T = c_i \langle m_i \rangle \\ \langle \Delta m_i \rangle = \langle m_i \rangle (1 - \rho_b / \rho_p) \end{array} \right. \quad (5.2)$$

The subscript i indicates the time point and ‘ $\langle \bullet \rangle$ ’ denotes the ensemble-based average; $\langle \Delta m_i \rangle$ and $\langle m_i \rangle$ are the average buoyant and dry mass of the aggregates at the i -th time point, with concentration c_i . V denotes the embedded channel volume, $\delta f / \delta m$ the device mass responsivity, ρ_b and ρ_p the buffer and protein densities, respectively.

Figure 5.4 shows the calculated values during the aggregation reaction. These estimates are obtained considering a protein density of 1.5 g/cm³ [105] for insulin and a solid content of 5 mg/mL. For monomeric insulin (0.01 ag), a concentration of ~ 1 M is needed to generate a detectable signal in the autocorrelation analysis, according to the device responsivity and readout noise. However, at $t=0$ the MCS signal has an amplitude of 4×10^{-5} Hz², corresponding to an average buoyant mass of the aggregates of $\sim 0.04 \pm 0.01$ ag (or a dry mass of $\sim 72 \pm 18$ kDa). This confirms the presence of small aggregates in solution when insulin is dissolved at low pH and high concentrations (mM concentration regimes) [106]. As the aggregation proceeded, the signal presented larger frequency fluctuations, leading to stronger MCS signals. After 8 hours of aggregation, the correlation signal shows an increase of more than two orders of magnitude with respect to the $t = 0$ measurement, corresponding to an average fibril mass of ~ 15 MDa.

5.1.2.3 Sonication of amyloid fibrils

After 8^{1/2} hours of aggregation, the insulin solution was subjected to two cycles of ultrasonication, a common technique used for preparing short fragments of seed fibrils [107] and for generating relatively monodisperse populations of fibrillar aggregates [108]. The ultrasonication was performed in an ice-water bath, to avoid temperature induced fibril formation during the process. The comparison between the signal variation experienced by the mass correlation signal and the ThT fluorescence is shown in Fig. 5.5a. Fluorescence intensity decreased $\sim 20\%$ after sonication, showing that ultrasonication

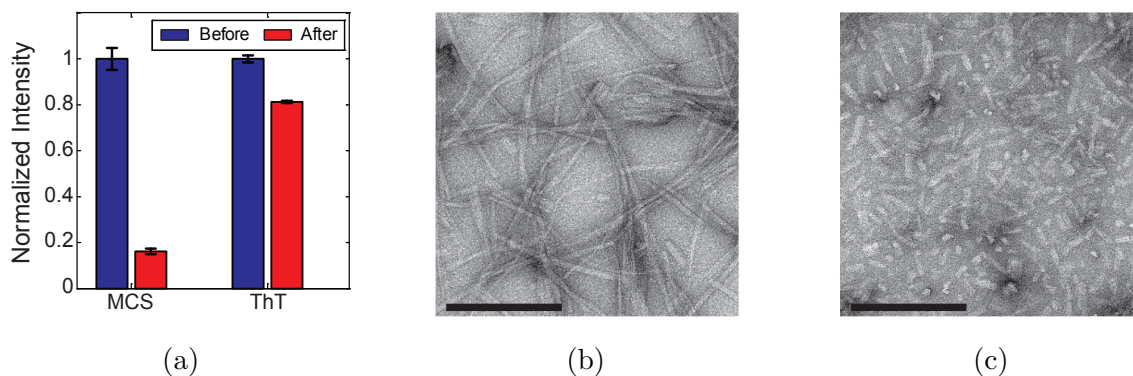


Figure 5.5: a) Variation of MCS and ThT fluorescence intensity upon ultrasonication of the fibril solution. Values are normalized to the average intensity before sonication. ThT only presents a small intensity variation, as the amount of fibrillated material in solution remains almost constant. In contrast, the MCS signal reflects the changes in fibril average mass; b) TEM image of the insulin solution before sonication. Scale bar 200 nm; c) TEM image after sonication. Scale bar 200 nm. The micrographs confirm the large variation in fibril length caused by ultrasonication. TEM images were taken by Dr. Riedel of the facility for Transmission Electron Microscopy, MPI for Biophysical Chemistry, Göttingen. Reprinted from Modena *et al.* [19].

slightly affected the amount of fibrillated material in solution; in contrast, mass measurements by SMR show a reduction of over 80% in correlation amplitude, denoting a large variation in sample average mass (size) and concentration. The average fibril mass corresponds to 25.2 ± 2.0 ag (buoyant mass 8.6 ± 0.6 ag) for the non-sonicated sample and 4.2 ± 0.4 ag (buoyant mass 1.40 ± 0.16) for the sonicated fibrils. Mass values can be converted to fibril length considering an expected insulin fibril mass per length of 2.47 kDa \AA^{-1} [109]. The average calculated length before sonication corresponds to 616 ± 48 nm and 100 ± 8 nm after ultrasonication. These results are in good accordance with the TEM images of the fibrils in the two cases, shown in Fig. 5.5b and 5.5c. Finally, as the correlation amplitude depends on the sample concentration, it is possible to define a fibril concentration in solution from the calculated average mass values: this corresponds to 330 ± 50 nM for the non-sonicated solution and 2.0 ± 0.3 μM after sonication. The results are summarized in Table 5.1.

Sample	Mass [ag]	Length [nm]	Concentration
Before sonication	25.2±2.0	616±48	330±50 nM
After sonication	4.2±0.4	100±8	2.0±0.3 μ M

Table 5.1: Length and concentration of fibrils in solution before and after ultrasonication, estimated from the average mass of the fibrils.

5.1.3 Materials and methods

Insulin aggregation protocol

5 mg/mL recombinant human insulin (Sigma-Aldrich Co.) was dissolved in 50 mM glycine buffer (Calbiochem) adjusted with HCl to obtain a pH value of 2.3. To remove amorphous aggregates that might act as aggregation center, the solution was centrifuged at $30,000\times g$ at 4 °C for 45 minutes. The supernatant was then collected and filtered with a 0.2 μ m filter. A final volume of 1 mL solution in a glass vial was subjected to continuous stirring with a magnetic stirrer, at 37 °C.

After 8 1/2 hours of incubation, the insulin solution was subjected to 2 cycles of 15 minutes ultrasonication in an ice-water bath.

MCS measurements

75 μ L of solution were withdrawn at different time points to measure the sample average mass by MCS. Each aliquot was mixed with a small concentration of 1.54 μ m NIST polystyrene beads (Polysciences Inc., Cat# 64040), to monitor the flow velocity during the measurements. The reference beads were pre-diluted in the same buffer used for the insulin aggregation to avoid changing the pH upon addition. 3 μ L of bead solution were added to the 75 μ L insulin aliquot. Then, the mixture was filtered with a 2 μ m filter, to remove large aggregates or clumps of beads that could block the device channel. The final concentration of reference particles was 5.5×10^6 beads mL⁻¹.

Mass measurements were taken using a double-paddle cantilever SMR (see section 2.3.1) in a 500 Hz and 1 kHz bandwidth. The readout frequency noise was ~ 0.15 Hz, corresponding to ~ 8 fg single-particle detection limit.

Data analysis

Time-domain mass traces were high-pass filtered (cutoff frequency 1 Hz) before applying the correlation analysis. The error bars in Fig. 5.4 and 5.5a are calculated from the statistical errors on the fitting parameters and the uncertainty on the characterization of the resonator sensitivity. Systematic errors caused by tolerances on the device geometry or sample preparations are not included.

ThT fluorescence assay

ThT (Sigma-Aldrich Co.,) was dissolved in 50 mM glycine, pH 8.2, at a concentration of 500 μM and stored at 4 $^{\circ}\text{C}$. At each time point, 3 μL of insulin solution were aliquoted and mixed with 87 μL ThT solution. The fluorescence emission of this mixture was measured with a NanoDrop 3300 fluorospectrometer (Thermo Scientific Inc.). The excitation and emission wavelengths were 470 nm and 506 nm, respectively. Blank measurements were taken before each time point, using ultrapure Milli-Q water. At each time point, three repetitions of fluorescence measurements were performed. The values reported in Fig. 5.4 and Fig. 5.5a correspond to the average fluorescence intensity value and error bars are calculated from the difference between the minimum and maximum values recorded per time point.

5.2 Quantification of bead protein coatings

Particles of nanometer dimensions find application in a large variety of fields, ranging from the medical field, where they are used as drug carriers or imaging contrast enhancer, to the production of solar cells, where they have shown the ability of improving solar energy absorption and conversion [110, 111, 112, 113]. As a result of their high surface-to-volume ratio and accurate control of their surface chemistry, nanoparticles are also widely used in biology for sample fractionation and purification [114, 115], or for the realization of bead-based assays for analyte detection [116, 117, 118, 119, 120, 121]. The quantification of surface coatings is therefore of primary importance for monitoring the correct functionalization of the bead surface and, for bead-based assays, for estimating the amount of captured target molecules. Currently, analyte quantification is obtained using label-based methods [118], such as fluorescence, or by elution and subsequent target analysis [114]. These approaches are usually not applied for quantifying the coating on the bead surface, as labeling might interfere with the capturing mechanism and simpler quantification strategies can be employed. Estimation of the surface coating layer is commonly achieved by measuring the variation of free solute concentration before and after the coupling step [122]. However, this method has the obvious limitation of only indirectly inferring the amount of material on the bead surface. Direct quantification of bead coverage would provide a more reliable detection method.

Here, theoretical calculations and proof-of-concepts measurements of the MCS capability in detecting surface coverage of nanoparticles in aqueous solutions are presented. Firstly, the limit of detection of a bead-based assay for the quantification of protein in solution is calculated theoretically. The detection limit is estimated by considering the minimum amount of mass increase that can be detected by MCS analysis. Subsequently, the adsorption of BSA protein on the surface of untreated polystyrene beads is quantified experimentally, as a proof-of-concept of the ability to detect mass variations caused by surface coatings using MCS. The correlation analysis does not require detection of single-particle signatures, therefore extending the analysis beyond the single-particle limits. In fact, MCS enables the characterization of surface coatings on nanoparticles below the single-particle detection limit; furthermore, it can also be used to quantify the average mass increase of visible particles, allowing the detection

at concentrations exceeding one particle per channel volume.

Application of SMR devices for measuring coatings of nanoparticles have recently been demonstrated [123, 124]. To increase resolution, a large number of particles (>1000) were individually characterized to elucidate the shifts in population average mass caused by the deposition on the bead surface. However, the need for high mass resolution and reliable characterization of the sample population causes long analysis time, due to the low sample concentrations required for single-particle analysis and the slow flow rates employed for reducing the acquisition bandwidth (discussed on page 21). By using the MCS approach, sample concentration can be increased with the dual advantage of high mass resolution and reduction in measurement time.

5.2.1 Theoretical calculations of bead-based assay resolution

5.2.1.1 Bead assay procedure

In this section, the theoretical detection range of a bead-based assay for the quantification of a protein of interest in solution is calculated. The assay consists of three steps: firstly, the average mass of polystyrene beads functionalized with antibodies is measured for reference. These antibodies will be referred to as primary antibodies. Secondly, the sample of interest is mixed with the functionalized beads and the protein binds to the immobilized primary antibodies. The last step consist of mixing with secondary antibodies to enhance the bead mass variation caused by the protein binding on the surface and to improve the specificity of the analysis. No washing is required after the last step, as free proteins in solution do not generate a detectable contribution in the correlation analysis unless their concentration exceeds $\sim 10 - 100 \mu\text{g/mL}$.

5.2.1.2 Assumptions

The following conditions are considered for the binding reaction: the protein and the antibodies have molecular weights of $m_P = 10 \text{ kDa}$ and $m_A = 150 \text{ kDa}$ respectively; their density ρ_A is 1.35 g/cm^3 ; the dissociation constant K_d between antibody and protein is 1 nM . Secondary antibodies are present in excess with respect to the analyte concentration and K_d .

The buffer has density ρ_b equal to water (1 g/cm^3); polystyrene beads have density ρ_n

of 1.05 g/cm³ and their surface binding capacity β_C is 250 ng/cm² [125]. The embedded channel resonator is a 50 μ m SNR, with a frequency/mass responsivity of 1 Hz/fg and a detection noise of 200 mHz in a 500 Hz bandwidth. The acquisition time is 200 s.

A list of the main symbols used in the calculations is reported here

Symbol	Definition	Symbol	Definition
d_n	Bead diameter	$[AP]$	Concentration of primary antibody/protein complexes
c_n	Bead concentration	$[X]$	Free concentration
ρ_n	Bead density	$[X_T]$	Total concentration
β_C	Surface capacity of the bead	m_A	Antibody molecular weight
Δm_0	Bead buoyant mass before assay	m_p	Protein molecular weight
Δm_f	Bead buoyant mass after assay	ρ_A	Antibody and protein density
ρ_b	Buffer density	K_d	Protein/antibody dissociation constant
T_{meas}	Acquisition time	V	Channel volume
$\delta f/\delta m$	Mass responsivity of the resonator	f_s	Sampling frequency
[X] refers to antibody (A) or protein (P) concentration			
[A*] refers to the effective primary antibody concentration			

Table 5.2: List of symbols used for the theoretical estimation of the detection capability of a bead-based assay by MCS.

5.2.1.3 MCS signal variation

Detection of protein in solution is obtained by quantifying the mass increase of the beads upon binding of the protein and secondary antibodies to the functionalized surface. The mass increase of the beads causes a relative increase of the correlation amplitude of

$$\frac{G_f(0)}{G_0(0)} = \left(\frac{\Delta m_f}{\Delta m_0} \right)^2 \quad (5.3)$$

where $G(0)$ is the maximum correlation amplitude, Δm denotes the average buoyant mass of the beads, and the subscripts ‘0’ and ‘f’ denote the initial and final values.

The buoyant mass of the functionalized beads at the beginning of the assay is

$$\Delta m_0 = \frac{1}{6} \pi d_n^3 \rho_n \left(1 - \frac{\rho_b}{\rho_n} \right) + \beta_C \pi d_n^2 \left(1 - \frac{\rho_b}{\rho_A} \right) \quad (5.4)$$

The first term is the buoyant mass of the untreated bead, while the second term is the mass added by the functionalization of the bead surface. After binding of the protein

and secondary antibodies to the immobilized primary antibodies, the buoyant mass of the bead corresponds to

$$\Delta m_f = \Delta m_0 + \frac{[AP]}{c_n}(m_P + m_A) \left(1 - \frac{\rho_b}{\rho_A}\right) \quad (5.5)$$

where $[AP]/c_n$ is the average number of complexes per bead, multiplied by the buoyant mass of the protein and secondary antibody. Assuming a 1:1 stoichiometry of the antibody/protein reaction, $K_d = \frac{[A^*][P]}{[AP]}$ (with $[P] = [P_T] - [AP]$ and $[A^*] = [A_T^*] - [AP]$). The concentration of complexes $[AP]$ can be readily calculated as

$$[AP] = \frac{1}{2} \left([P_T] + [A_T^*] + K_d - \sqrt{([P_T] + [A_T^*] + K_d)^2 - 4[P_T][A_T^*]} \right) \quad (5.6)$$

Figure 5.6 shows the variation of MCS signal as a function of protein concentration. The signal variation is shown for three different sizes of beads suspended at their minimum detectable concentrations, as discussed in the next section.

$[A_T^*]$ depends on bead size and concentration and is estimated as

$$[A_T^*] = c_n \frac{\pi d_n^2 \beta_C}{m_A}. \quad (5.7)$$

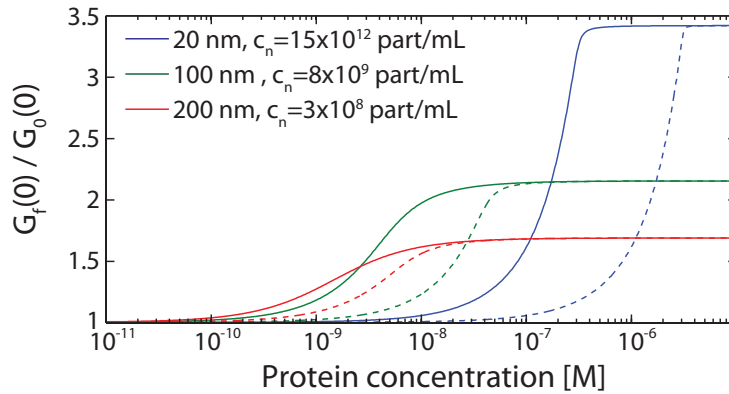


Figure 5.6: The MCS variation as a function of protein concentration for beads of three different sizes. The bead concentrations are calculated from Eq. 5.8. The corresponding effective concentrations of primary antibodies are $0.3 \mu\text{M}$, 4 nM and 0.6 nM for the 20 nm , 100 nm and 200 nm beads, respectively. The dashed lines show the detection ranges for a tenfold increase in bead concentration, corresponding to a tenfold concentration of $[A_T^*]$.

Smaller beads show larger dynamic ranges of mass variation over the detection interval as a result of their lower buoyant mass. However, the high concentrations of beads required to detect their signal in the correlation curve limit the sensitivity of the analysis.

5.2.1.4 Limit of detection

Minimum required bead concentration

From the definition of signal-to-noise (S/N) ratio of the MCS signal (Eq. 3.17), it is possible to calculate the minimum concentration of beads that is required to generate a detectable signal. By requiring a S/N ratio of 3, the minimum concentration is given by

$$c_n = 3 \cdot \frac{5\sigma_n^2}{V\sqrt{T_{meas}f_s}(\Delta m_0 \delta f/\delta m)^2} \quad (5.8)$$

The symbols are defined in Table 5.2 and Δm_0 in Eq. 5.4. The corresponding effective concentration of immobilized antibodies [A_{Tmin}^*] can be calculated by inserting Eq. 5.8 in Eq. 5.7. Figure 5.7 shows the minimum concentration of beads as a function of their size and the resulting [A_{Tmin}^*].

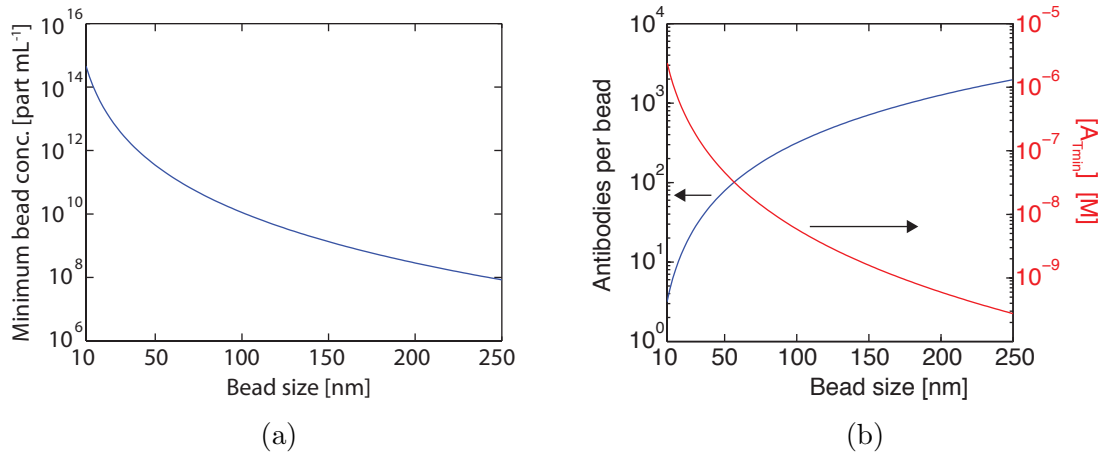


Figure 5.7: a) Concentration of functionalized beads to have a signal-to-noise ratio of 3 in the autocorrelation analysis using a 50 μm SNR device. The concentration scales as the square of the particle mass; b) average number of antibodies per bead, considering a surface binding capacity of 250 ng/cm² and a molecular weight of the antibodies of 150 kDa.

Detection range

Once the effective concentration of immobilized antibodies is known, the limit of detection of protein in solution and the detection range of the assay can be estimated as a function of bead size. The detection limit can be defined as the minimum protein concentration required to induce an increase of 25% of the correlation amplitude, corresponding to a mass increase of $\sim 22\%$. From Eq. 5.5 and Eq. 5.4, the minimum detectable concentration of complexes is

$$[AP_{min}] = 0.22 \cdot \frac{c_n \Delta m_0}{(m_p + m_A) (1 - \rho_b / \rho_A)} \quad (5.9)$$

Therefore, the minimum detectable protein concentration can now be estimated from the dissociation constant, resulting in

$$[P_{Tmin}] = \frac{[AP_{min}](K_d + [A_{Tmin}^*] - [AP_{min}])}{[A_{Tmin}^*] - [AP_{min}]} \quad (5.10)$$

The correlation signal increases linearly with the analyte concentration when the antibody/protein complexes do not exceed $\sim 90\%$ of the immobilized antibody. By imposing $[AP_{max}] = 0.9[A_T^*]$, the maximum limit of detection in the linear range can be estimated from Eq. 5.10 by substituting $[AP_{min}]$ with $[AP_{max}]$. The limit of detection of the assay and the associated detection range as a function of bead size are shown in Fig. 5.8a. The increase in detection range with bead size is caused by the decrease in the effective concentration $[A^*]$ of unbound primary antibodies. This can be clearly noticed for beads larger than 150 nm, where the effective concentration of the primary antibodies is of the same magnitude as K_d .

The variation in correlation amplitude in the detection range is

$$\frac{G_f(0)}{G_0(0)} = \left(1 + \frac{[AP] (m_p + m_A) (1 - \rho_b / \rho_A)}{c_n \Delta m_0} \right)^2 \quad (5.11)$$

where $[AP]$ is given by Eq. 5.6 and varies between $[AP_{min}]$ and $[AP_{max}]$. The saturation level of the MCS variation as a function of bead size is shown in Fig. 5.8b.

With a detection range in the low nM regime and a MCS signal doubling over the detection range of the assay, beads of ~ 100 nm show a good compromise between

detection limit and signal variation. Finally, the curves in Fig. 5.8 show the detection range for the minimum concentration of beads. However, the assay can be extended to detect higher concentrations of protein by increasing the number of beads, as shown in Fig. 5.6.

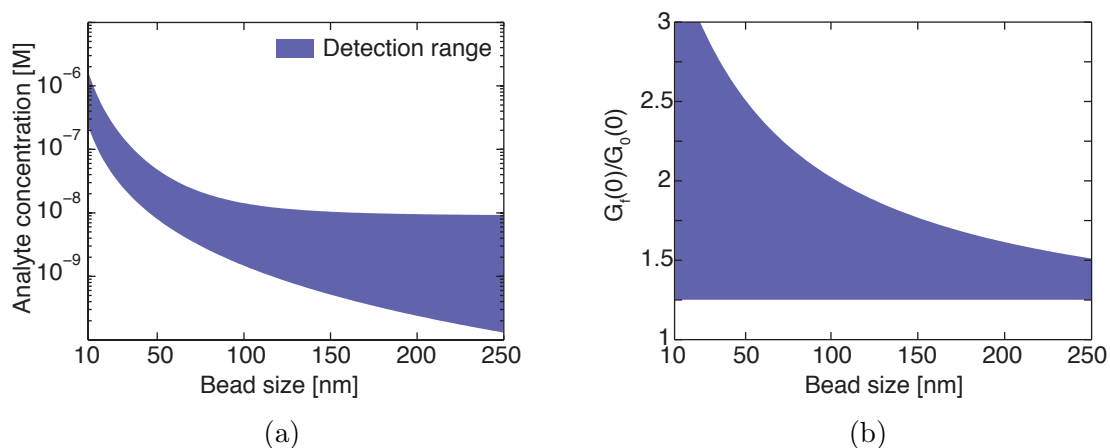


Figure 5.8: a) Theoretical detection ranges of the protein in solution. The minimum concentration is calculated considering a 25% increase in MCS signal caused by the binding of the protein and secondary antibodies on the bead surface. The maximum range corresponds to 90% of the active sites on the bead surface bound to the protein. The blue shaded area shows the detection range considering a bead concentration equal to the minimum detectable one; b) expected MCS signal increase during the assay. The shaded area shows the dynamic range of the correlation increase in the detection range.

5.2.2 Quantification of surface coating of polystyrene beads

The measurements reported here are presented as proof-of-concept of the MCS capability in quantifying surface coatings of suspended beads.

390 nm polystyrene beads suspended in phosphate-buffered saline (PBS) solution and in a 0.5 mg/mL Bovine Serum Albumin (BSA) in PBS solution were measured with a double-paddle SMR device. After 1 hour incubation with the protein solution, the average detected mass of the polystyrene beads showed an increase of $\sim 30\%$ caused by the BSA adsorption on the particle surface. The beads could not be detected in single-particle detection mode and quantification of the protein coating on the bead surface could only be obtained by MCS analysis.

5.2.2.1 Results and discussion

After diluting the 390 nm beads in pure PBS and PBS with BSA solutions, the samples were analyzed with the SMR. No separation or purification of the beads was necessary, as the amount of free protein in solution was too low to be detected by correlation analysis (see Fig. 5.9a). The average induced frequency shift can be calculated with high precision after fitting the MCS signal, as the bead concentration in solution is known. In fact, the beads employed here present a very high monodispersivity and the mean square frequency shift $\langle \Delta f^2 \rangle$ is practically equal to $\langle \Delta f \rangle^2$. From the parameters extracted from the MCS fit, the beads induced an average frequency shift of 31.8 ± 3.1 mHz and of 41.2 ± 0.2 mHz before and after BSA, respectively. This, in turn, can be converted to a buoyant mass of 1.55 ± 0.15 fg (experimental repeatability, statistical error ~ 0.03 fg) and 2.01 ± 0.01 fg before and after protein coating (see Fig. 5.9b). The frequency/mass conversion was calculated by assuming a buffer density of 1.005 g/cm³, because of the presence of the salts and protein in solution, and a polystyrene density of 1.05 g/cm³. According to the reference particle signatures, the mass responsivity corresponded to 20.5 ± 1.0 mHz/fg. Therefore, the average mass increase per bead caused by protein adsorption was 0.46 ± 0.15 fg. Considering a protein density of 1.35 g/cm³ for BSA [105], this value corresponds to $(16 \pm 5) \times 10^3$ BSA monomers per bead or to a surface binding density of 380 ± 120 ng/cm², a value in good accordance with complete monolayer coverage of untreated polystyrene [126]. Finally, it should be noted that knowledge of the absolute bead concentration is not required to characterize the surface coating, if information on the relative increase in bead mass is sufficient. Considering that the bead concentration is conserved during the coupling protocol, the ratio of the correlation magnitudes (see Eq. 3.16) returns $\langle \Delta f_C^2 \rangle / \langle \Delta f_B^2 \rangle$, where Δf_C and Δf_B are the induced frequency shifts for the coated and bare beads, respectively, and ' $\langle \bullet \rangle$ ' denotes the population mean value. Therefore, the relative increase of the buoyant mass of the beads can be readily calculated from the autocorrelation amplitude values, resulting here in a 30% average mass increase of the beads, consistent with the absolute quantification of the bead mass.

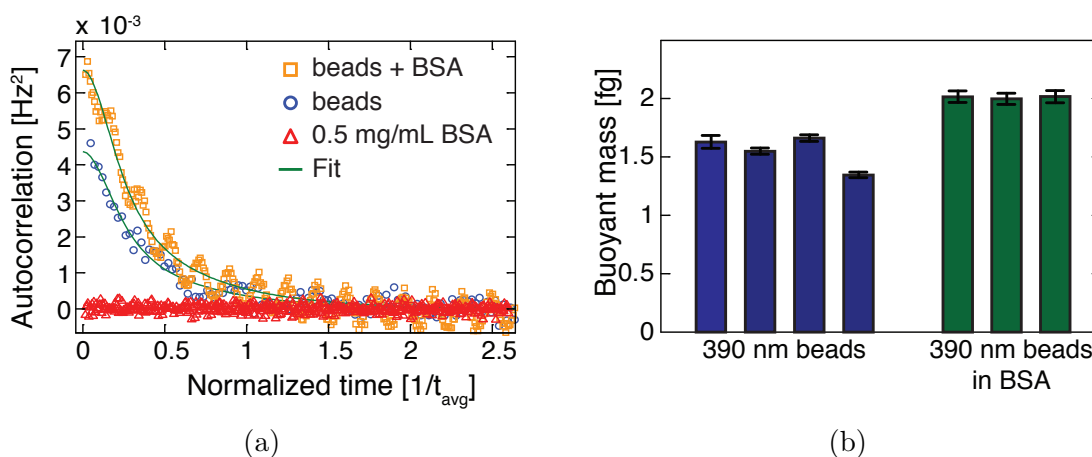


Figure 5.9: a) Comparison between the autocorrelation curve of solutions of bare and protein coated polystyrene beads. Free BSA in solution (0.5 mg/mL) is not sufficient to give a detectable signal; b) average buoyant mass of the beads before and after incubation. Error bars represent the statistical errors from the fit uncertainties.

5.2.2.2 Materials and methods

Sample preparation

390 nm NIST polystyrene beads (Polysciences, Cat# 64017) were initially dissolved in a 50 mM NaCl aqueous buffer together with 1.54 μm NIST polystyrene beads (Polysciences, Cat# 64040), here referred to as reference particles. This solution was then added to a PBS solution (1:1) and to a solution of 1 mg/mL BSA (Carl Roth GmbH) in PBS (1:1), obtaining a concentration of 3×10^9 beads mL^{-1} for the 390 nm particles and of 5×10^6 beads mL^{-1} for the reference particles.

The beads were incubated in the protein solution for 1 hour at room temperature and stirred with a magnetic stirrer, to avoid settling of the particles at the bottom of the vial.

MCS measurements

The bead solutions were measured without any further preparation and purification. Pure solutions without suspended beads were also measured under similar flow rates to quantify the background noise in the time domain signal. Each measurement trace was acquired for ~ 4 minutes, keeping the pressure conditions constant during the measurement. The 1.54 μm particle signatures in the time-domain signal were used to

characterize the mass/frequency response of the SMR and to monitor the stability of the flow.

Time-traces were high pass filtered (cut off frequency 1 Hz) before data analysis, to remove the slow varying noise contributions in the signal and the static component of the frequency measurement.

A double-paddle SMR resonator, as described in Sec. 2.3.1, was used for the detection of the bead mass variation.

5.3 Label-free detection of ribosomes

The ribosome is a macromolecular complex composed of ribonucleic acids (RNAs) and proteins. Present in all cells, ribosomes are in charge of protein synthesis by translating the messenger RNA (mRNA) into polypeptides. Protein synthesis requires several steps of interactions between the two subunits of the ribosome and of the subunits with the mRNA, transport RNA (tRNA) and protein factors, which result in the formation of different translation complexes [5, 127]. Kinetic information on the interactions of the different players involved are therefore of great interest for improving our understanding of protein synthesis. Kinetic measurements are currently obtained using fluorescence-based techniques, such as Förster resonance energy transfer (FRET) measurements [5, 128, 129], or based on the detection of radioactively labeled molecules [130, 131, 132]. Despite the high specificity given by the labeling strategies, labeling presents several disadvantages as it can possibly interfere with the reaction mechanism. The resolution enhancement obtained by correlation analysis might enable the detection of ribosome complexes by SMR, hence providing a label-free alternative for the kinetic measurements.

Here, proof-of-principle measurements of 70S *Escherichia coli* ribosomes by SMR are shown. Firstly, the density of the ribosome is estimated, presenting the capability of the correlation analysis in detecting particle density by using different density solutions. Subsequently, the average mass value calculated from the correlation amplitude is discussed. The mismatch between the detected and the theoretical ribosome mass shows that improvements in detection protocol are needed before proceeding to kinetic studies.

5.3.1 Density characterization

The density of bacterial ribosomes was measured by detecting the variation of correlation amplitude as a function of density of the suspending solution.

5.3.1.1 Detection method

The MCS amplitude scales as the square of the buoyant mass of the particles in solution (see Eq. 3.1 and Eq. 3.16). By explicitly expressing the dependence on the density of the suspending solution, the correlation amplitude at lag zero is given by

$$\beta_1(\rho_b) = \left(\frac{1}{5} c_0 V m_p^2 \left(\frac{\delta f}{\delta m} \right)^2 \right) \cdot \left(1 - \frac{\rho_b}{\rho_p} \right)^2 \quad (5.12)$$

where β_1 represents the correlation amplitude, c_0 is the sample concentration, V the channel volume, m_p the dry mass of the particle, $\delta f/\delta m$ the device responsivity, ρ_p and ρ_b are the particle and buffer densities, respectively. From Eq. 5.12 it can be noticed that the correlation amplitude varies as a parabola with the buffer density, and the amplitude reaches its minimum for $\rho_b = \rho_p$ with $\beta_1(\rho_b = \rho_p) = 0$. Characterization of the sample in at least two solutions of different densities is required to obtain an estimate of the particle density.

5.3.1.2 Ribosome density

70S *E.coli* ribosomes suspended in buffer A (see Materials and methods on page 98) with different concentrations of sucrose content were characterized by MCS. Ribosome concentration was kept constant in all measurements and changes in correlation amplitude are only caused by the buffer density variations, as presented in Eq. 5.12.

Figure 5.10 shows the variation of correlation amplitude for a sample of 2 μM ribosomes suspended in solutions of densities 1.01 and 1.21 g/cm^3 . The trend of the correlation amplitude is fitted by a quadratic function

$$y = K(\rho_p - \rho_b)^2 \quad (5.13)$$

to estimate the density ρ_p of the ribosomes. The parameter K includes the experimental conditions that are constant during the measurements, namely sample concentration, channel volume, ribosome mass and device responsivity (see Eq. 5.12). From the fit of the correlation amplitude variation, a density estimation of $1.37 \pm 0.04 \text{ g}/\text{cm}^3$ is obtained. This value is consistent with an expected value of density ranging between

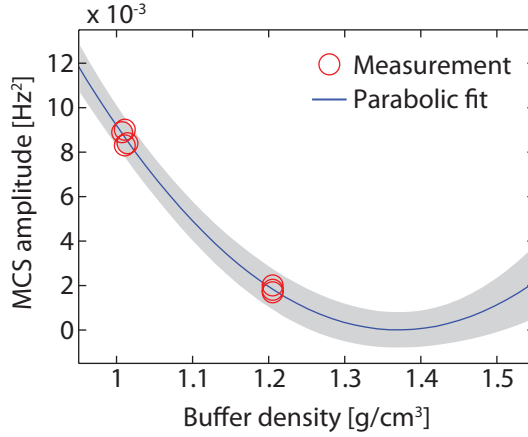


Figure 5.10: Variation of MCS amplitude for a sample of 70S *E.coli* ribosomes as a function of solution density. The ribosomes were suspended in buffers with different sucrose content. The trend of the correlation amplitude is fit by a quadratic function of the form $y = a(b-x)^2$, where a and b are fit parameters (blue solid line). The shaded gray area indicates the 90% confidence interval of the fit. The parameter b is $1.37 \pm 0.04 \text{ g/cm}^3$ and corresponds to the estimated density of the ribosomes.

1.3 and 1.6 g/cm^3 . This interval is calculated from the molecular weight of the ribosome in solution $\sim 2.7 \text{ MDa}$ [133, 134] and its estimated volume from air-dried EM, between 3.0 and $3.6 \times 10^3 \text{ nm}^3$ [135].

5.3.2 Results and discussion

The mass of the ribosomes can be calculated from the correlation amplitude using the density value estimated in the previous section. As both the molar concentration of ribosomes and the solid content in solution are known, the average mass can be calculated from the mean square mass value (Eq. 3.16) as

$$m_1 = \sqrt{\frac{5\beta_1}{c_0 V (1 - \rho_b/\rho_p)^2 (\delta f/\delta m)^2}} \quad (5.14)$$

or from the solid content in solution (Eq. 5.1) as

$$m_2 = \frac{\langle m^2 \rangle}{\langle m \rangle}. \quad (5.15)$$

$m_1 = \sqrt{\langle m^2 \rangle}$ and, for a monodisperse population of particles with concentration c_0 , m_1 and m_2 converge, as $\langle m^2 \rangle \approx \langle m \rangle^2$. The results obtained from the calculations are

Sample	Δm_1 [ag]	m_1 [ag]	Δm_2 [ag]	m_2 [ag]
BufferA 1	2.20 ± 0.21	8.4 ± 0.8	4.44 ± 0.93	17.0 ± 3.6
BufferA 2	2.16 ± 0.20	8.2 ± 0.8	4.29 ± 0.83	16.4 ± 3.2
BufferA 3	2.19 ± 0.17	8.3 ± 0.7	4.40 ± 0.78	16.8 ± 3.0
BufferA 4	2.19 ± 0.14	8.4 ± 0.8	4.41 ± 0.67	16.8 ± 2.7
Sucrose 1	0.96 ± 0.14	8.2 ± 1.3	1.92 ± 0.70	16.4 ± 6.0
Sucrose 2	0.97 ± 0.13	8.3 ± 1.3	1.96 ± 0.68	16.8 ± 5.9
Sucrose 3	1.07 ± 0.11	9.2 ± 1.1	2.36 ± 0.73	20.2 ± 6.4

Table 5.3: Estimates of the buoyant (Δm) and dry (m) mass of the ribosomes. m_1 is calculated according to Eq. 5.14, while m_2 according to Eq. 5.15. The ribosome density is 1.37 g/cm^3

reported in Table 5.3, both for the measurements taken in buffer A and in sucrose-buffer A solution mixture. The large differences between the m_1 and m_2 values show that the ribosome mass cannot be estimated from the acquired measurements, as the sample might present a high degree of polydispersivity or interactions with the channel walls. Furthermore, m_1 and m_2 are, respectively, ~ 1.5 and ~ 3 times larger than the expected ribosome mass ($\sim 2.7 \text{ MDa}$). Non-filtered time-traces of both measurement conditions are shown in Fig. 5.11. The decreasing frequency values are evidence of the interaction between the ribosomes and the silicon walls. Variations of measurement conditions, for example by passivation of the channel walls, need to be investigated to reduce this behavior.

Although the density estimate might also be affected by these interactions, density measurements are not based on absolute quantification of the correlation amplitude. The repeatability of the measurements suggests that the interactions are stable during the acquisition, and, as such, only affect the absolute amplitude of the correlation curve and not the dependence on solution density. However, density measurements need to be repeated once a suitable protocol is developed, to confirm the validity of the assumption.

5.3.3 Materials and methods

Sample preparation

70S *E. coli* ribosomes suspended in buffer A (50 mM Tris-HCl, pH 7.5, 70 mM NH₄Cl, 30 mM KCl and 7 mM MgCl₂) at a concentration of $14.5 \mu\text{M}$ were diluted in buffer

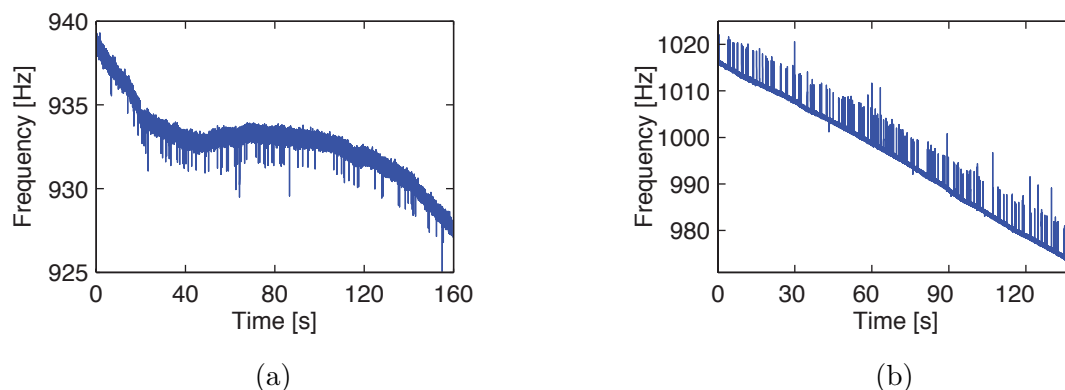


Figure 5.11: Time-traces of the ribosome measurements in buffer A (a) and sucrose-buffer A solution (b). The frequency decrease is evidence on sample interaction with the walls. Note that the reference particles induce a positive shifts in the sucrose solution, as a consequence of the particle density being lower than the solution one.

A or with a solution of sucrose - buffer A, to obtain a ribosome concentration of $2.9 \mu\text{M}$. These solutions were then filtered with a $0.2 \mu\text{m}$ low protein binding filter (Merck Millipore) and sample concentration was checked by absorbance measurement at 260 nm using a NanoDrop 2000c photospectrometer (Thermo Scientific Inc.). Sample solutions were then diluted with buffer A to obtain a final sample concentration of $2 \mu\text{M}$.

$1.54 \mu\text{m}$ polystyrene beads suspended in the sample solutions were added before MCS measurements as standards for density calibration and monitoring of flow conditions during measurement. The bead concentration was $7 \times 10^6 \text{ beads mL}^{-1}$.

Solution density characterization

Sample solution densities were estimated from the magnitude of the frequency shifts induced by the calibration particles, assuming a device responsivity of $\sim 20.5 \times 10^{-3} \text{ Hz/fg}$ and a dry mass of the beads of 2.01 pg . The estimated densities of the suspending solutions were 1.01 g/cm^3 for buffer A and 1.21 g/cm^3 for the 1.5 M sucrose - buffer A mixture.

The histograms of the measured frequency shifts induced by the reference particles in the two solutions are shown in Fig. 5.12. As the density of the sucrose solution was higher than polystyrene density (1.05 g/cm^3), the reference beads induced a positive frequency shift.

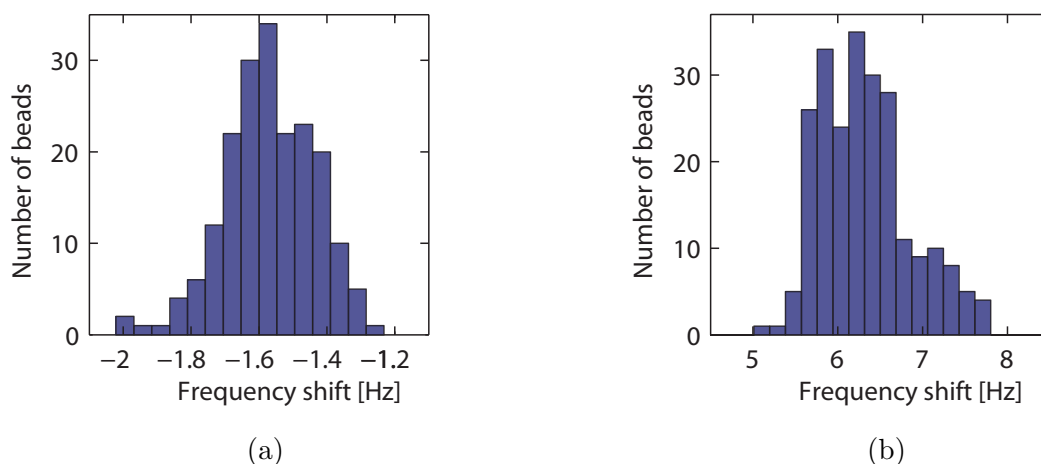


Figure 5.12: The frequency shifts induced by the reference beads in buffer A (a) and in a solution of 1.55 M sucrose - buffer A (b).

Ribosome density estimation

Ribosome density was estimated from the variation of the autocorrelation amplitude as a function of buffer density. Eq. 5.13 was used as fit function for the correlation amplitude trend. A lower boundary of 1.3 g/cm^3 for ρ_b was set to obtain a unique solution to the fit.

MCS measurements

MCS measurements were taken using a double-paddle SMR device, as presented in section 2.3.1. Measurements were acquired at sampling rates of 500 Hz and 1 kHz, with acquisition noise of $\sim 0.1 \text{ Hz}$ and $\sim 0.2 \text{ Hz}$, respectively

5.4 Flow velocity detection in SMR channel

SMR detection in mass accumulation mode requires interaction between the free analyte in solution and the functionalized surfaces of the channel (see page 24). Therefore, depletion of the analyte at the channel walls could hinder the reaction under investigation. Correlation analysis can be used to precisely measure the flow velocity in the channel by adding tracer particles to the solutions, hence providing estimation on the mass transport of the analyte during the detection.

Here, application of the correlation analysis for flow velocimetry is presented in the context of measurements of insulin fibril elongation by mass accumulation mode. These results are part of the doctoral thesis of Y. Wang [136] and have been recently presented in Wang, Modena *et al.* [18].

5.4.1 Label-free detection of amyloid elongation

Several methods have been developed for detecting protein aggregation. Dye-binding assays are commonly used for reporting amyloid formation thanks to their high specificity and sensitivity, as already discussed on page 78 for ThT based assays. However, precise quantitative information on binding rate constants cannot be obtained with such assays. Therefore, label-free methods are usually preferred for measuring the elongation rate of amyloid fibrils [137]. High spatial resolution and real time monitoring of the growth of individual aggregates are possible by AFM detection [138]. However, the limited throughput and the complexity of the analysis renders this method not suitable for quantitative studies. Larger statistics are obtained by using ensemble-based detection methods, such as quartz crystal microbalance (QCM) or surface plasmon resonance (SPR). Here, aggregate growth is measured by detecting the increase in mass of the fibrils immobilized on the sensor surface.

Detection of kinetic rate constants by surface-based methods can be affected by the mass transport of the protein monomers to the immobilized fibrils. This effect can be accounted for during data analysis, however this would introduce large uncertainties on the kinetic rate estimation [139]. To avoid mass transport limitations, fast flows in the detector cells can be used, at the expense of large sample consumption.

Similar to QCM and SPR measurements, SMRs operated in mass accumulation

mode can detect changes of the adsorbed mass on the surface of the embedded microfluidic channel, with femtogram resolution [14]. However, the small channel volume (~ 10 pL) enables the use of fast flows to avoid mass transport limitations, while allowing low sample consumption (less than ~ 1 $\mu\text{L}/\text{min}$).

Human insulin was selected as model protein for the study of the fibril elongation kinetics in the SMR. Elongation was detected at different conditions, such as at different monomer concentrations or ionic strength of the solutions.

5.4.2 Results

All surface preparations and amyloid elongation measurements were done by Y. Wang. Analysis of the flow rates was done by M. Modena and Y. Wang by using the methods developed in this thesis. TEM imaging and sample preparation was done by D. Riedel and G. Heim of the MPI for Biophysical Chemistry. AFM imaging and sample preparation was done by Mitja Platen of the University of Göttingen.

Insulin fibrils of ~ 100 nm length were covalently bound to the aminated surfaces of the 3×8 μm^2 microfluidic channel embedded in the double-paddle SMR. The immobilization of the fibrils resulted in a static frequency shift of $\Delta 71.3 \pm 8.6$ Hz (reproducibility error), corresponding to a mass deposition of $(8.56 \pm 1.03) \times 10^{-16}$ $\text{g}/\mu\text{m}^2$. This can be translated in 734 ± 89 molecules/ μm^2 , estimated from the length of the fibrils (98 ± 20 nm, from TEM characterization) and the mass per length density of the fibrils [109]. As the device resonance frequency settles at a constant value during the functionalization, it is safe to assume that fibrils saturate the channel walls, therefore being uniformly distributed in the resonator. Functionalization was followed by a passivation step to avoid unspecific adsorption of the monomers on the walls. For the complete protocol for surface immobilization and preparation of the seed fibrils, please refer to Wang *et al.* [18].

After immobilization of seed fibrils, a solution of 1 mg/mL insulin monomer was injected in the resonator and continuously flown. Figure 5.13a shows the variation of resonance frequency caused by the elongation of the fibrils. Frequency decrease is linear with time, indicating a constant growth rate of the fibrils. Knowing the density of fibrils on the surface and the buoyant mass of insulin monomers ($\sim 2.9 \times 10^{-3}$ ag),

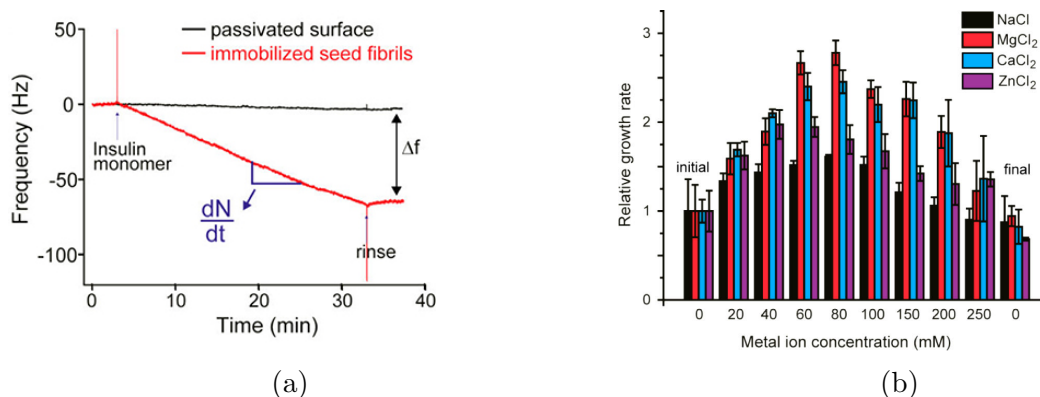


Figure 5.13: a) Frequency shift induced by the elongation of the insulin fibrils immobilized on the channel walls, compared to the non-functionalized/passivated resonator. A solution of 1 mg/mL insulin monomer is flowing in the channel; b) Increase of fibril growth rate as a function of metal ions and of their concentration. Reprinted with permission from Wang *et al.* [18]. Copyright 2015 American Chemical Society.

the elongation rate dN/dt can be calculated and corresponds to 12.2 ± 1.2 monomer molecules per fibril per minute. For linear fibril elongation,

$$\frac{dN}{dt} = k \times N_{fibril} \times c_{monomer} \quad (5.16)$$

with N_{fibril} the bound monomer per fibril and $c_{monomer}$ the concentration of free monomers in solution. The estimated growth reaction rate is $k = (1.2 \pm 0.1) \times 10^3 \text{ M}^{-1}\text{s}^{-1}$.

Immobilized fibrils were exposed to different conditions to detect variations in elongation rate. As an example, Fig. 5.13b shows the results obtained by detecting the fibril growth in the presence of different metal ions in solution. Insulin elongation measurements were taken by Yu Wang.

5.4.2.1 Mass transport estimation

To ensure that the elongation occurs in a reaction-limited regime, it is necessary to estimate the monomer transport to the immobilized fibrils. Flow in the embedded channel is controlled by pressurized inlets and outlets, and estimation of flow velocity has to be done experimentally. Although theoretical calculations regarding the flow resistance of the channel can be made, these might result in large deviations from the

actual value because of tolerances in device dimensions during fabrication. Furthermore, the viscosity of the solution also varies with protein concentration, increasing the uncertainties on theoretical velocity estimations. Solutions containing 1.54 μm polystyrene particles were run through the functionalized channel. Similar to the measurements discussed in the previous sections, these particles were used as references for flow velocity estimation. Although particles are clearly identifiable in the time-trace and individual signatures could be used for the detection of flow velocity, the correlation analysis approach presents multiple advantages. A single fit of the correlation curve is required for the estimation of the flow rate in the channel, regardless of the number of tracer particles. The increase in signal amplitude with particle number also improves the resolution of the estimation. On the contrary, a single-particle approach requires identification of the signatures and their individual fitting, with a signal-to-noise ratio of the signature only dependent on the buoyant mass of the particle.

From the analysis, the slowest flow velocity at experimental conditions was shown to be ~ 14 mm/s. Assuming a diffusivity $D = 1 \times 10^{-10}$ m²/s for the insulin monomer, the Péclet number $\text{Pe} = U_{\text{avg}}h/D$ during the elongation measurements was higher than 200 (h half height of the channel). This indicates that any concentration gradient would only occur in the vicinity of the channel walls, where convection is slow. However, insulin monomers diffuse across the whole cross-section in ~ 20 ms, while the average addition of a monomer to a fibril has a characteristic time of few seconds. The Damkohler number is $\text{Da} \ll 1$ (where $\text{Da} = \text{time}(\text{diffusion})/\text{time}(\text{reaction})$), indicating that the analysis is performed in reaction-limited regime.

5.4.3 Materials and Methods

Insulin seed fibril

Insulin was dissolved in 10 mM HEPES buffer, pH 2.0, at a concentration of 6 mg/mL. The solution was incubated at 37 °C under continuous stirring and amyloid formation was confirmed by ThT fluorescence measurements. At the conclusion of the elongation phase, the solution was diluted to 1 mg/mL and ultrasonicated for 150 min at 4 °C to generate the seed fibrils. Seed fibrils were then characterized by TEM.

SMR measurements

A double-paddle resonator (page 19) was used for the kinetic studies. The mass/frequency response was calibrated using solutions of sodium chloride at different concentrations and measuring the frequency variations induced. Mass accumulation measurements were performed on 0.1 Hz low-pass filtered signals. On the contrary, correlation analysis for flow velocity detection was performed on 1 Hz high-pass filtered traces.

Surface functionalization

Seed fibrils were immobilized on the aminated surfaces of the SMR embedded channels. After immobilization, the channels were passivated by injecting a 50 mM glycine solution, to avoid unspecific binding of monomers to the channel walls.

Chapter 6

Conclusions

In this thesis, the application of suspended microchannel resonators (SMRs) has been extended to the characterization of macromolecular complexes in the sub-MDa mass range, such as protein aggregates or cellular organelles. This has been enabled by the introduction of correlation analysis of the time-domain mass signal as novel method for mass characterization of particles in solution. Discrete particles flowing through the microfluidic channel embedded in the resonator generate a detectable signal in the correlation curve, even when single-particle signatures cannot be individually recognized in the time-trace. Resolution enhancement of over four orders of magnitude in mass detection has been demonstrated by characterizing validated synthetic nanoparticles and samples of biological interest.

First, the theoretical basis of the mass correlation spectroscopy (MCS) method has been presented, elucidating the dependence of the correlation amplitude on the buoyant mass and on the concentration of the particles in solution. It was demonstrated that the detection limit of the analysis does not depend exclusively on the readout noise of the measurement, and it can be improved by increasing sample concentration and acquisition time. Therefore, the resolution attainable is ultimately limited by the sample volume and flow stability. Previously, mass sensitivity increase was achieved by reducing the resonator effective mass, and devices with single-particle resolution approaching the attogram (\sim MDa) level have been recently demonstrated. However, these devices already present sub-micrometer channel dimensions and further scaling of the resonator structure is technologically challenging. Furthermore, the use of small cross-sections poses severe limitations on the sample, as particle size cannot exceed

the cross-section dimensions and the high fluid resistance of the channel limits the viscosity of the solutions that can be injected in the resonator. In contrast, resolution enhancement by correlation analysis does not require modifications of the devices, and sub-attogram resolution has been obtained in this thesis using resonators with $3 \times 8 \mu\text{m}^2$ embedded channels and femtogram single-particle resolution.

Furthermore, a model was built to enable size determination of particles in solution with the SMR devices. The evolution of the concentration fluctuations in the embedded channel was described by developing an approximate model for the transport of finite-size particles in a channel of rectangular cross-section. Including this model into the description of the correlation analysis allows size determination of particles in solution by MCS measurements. As a proof-of-principle, monodisperse samples of particles of different dimensions were measured and their size, mass and density was obtained in a single experiment. Particle size is inferred from the diffusion/dispersion of the sample in the embedded channel. As a result of the dual detection of size and mass, the MCS analysis is significantly more sensitive to small size changes than purely diffusivity-based methods, such as dynamic light scattering. As an example, a 5% increase in diameter, corresponding to an equal decrease in diffusivity, would generate an increase of over 30% in correlation amplitude.

The ability to analyze samples made up of a heterogeneous population of particles has also been discussed, showing that the correlation shape contains information on the mass and size distribution of the particles. However, the deconvolution of the MCS signal for a polydisperse sample is not trivial. The determination of the size distribution might be limited to samples composed of populations with large differences in average velocities and dispersion in the channel. Similar to characterization by light scattering techniques, size determination would be best performed after fractionation of the sample.

Characterization of samples of biological interest in the sub-MDa regime can now be performed by SMRs thanks to the resolution enhancement obtained by correlation analysis. To explore the applicability of the method to different domains of applications, four proof-of-principle measurements have been presented.

First, the kinetics of amyloid formation in solution was monitored by mass using

insulin as a model system, and the MCS method has been compared with the conventional Thioflavin-T fluorescence assay. The MCS method enabled label-free detection of protein aggregation kinetics, by quantifying the increase of the average mass of the aggregates in solution. As a consequence of the purely mass-based detection method, the aggregation kinetics could be monitored from the formation of the early amorphous aggregates, where the fluorescence assay is blind, to the conversion into mature fibrils. In the specific case discussed here, the variation of the average mass of the aggregates was quantified in ~ 100 kDa at the onset of aggregation to 15 MDa at the end of the aggregation study, using a device with single-particle resolution of ~ 1000 MDa.

As another application, quantification of protein coatings on nanoparticles was demonstrated by detecting the mass increase caused by BSA adsorption onto 400 nm polystyrene beads. Correlation analysis for the quantification of surface coatings shows superior performance compared to single-particle detection, as large statistics on the sample population can be obtained with shorter analysis times and higher resolution. Theoretical calculations on the minimum resolvable mass increase for particles of different sizes have been presented. This information was used to estimate the detection limit of protein concentration with SMR devices using a mass-based bead-linked immunosorbent assay, as a function of device responsivity and bead properties. The calculations presented allows predictions on the optimal size of the beads for the immunosorbent assay, providing estimations on minimum detectable protein concentration and detection range of the assay. Although theoretical calculations in this thesis are only presented for the case of bead-based immunoassays, detection of nanoparticles by correlation analysis finds larger application. Nanoparticles ranging from a few to hundreds of nanometers are also emerging as carriers for drug delivery. Mass characterization can therefore be used as a method for direct quantification of the active component encapsulated in or grafted to the nanoparticle carrier.

Application of the MCS method has also been presented in conjunction with SMR measurements by mass accumulation detection mode. As surface-based kinetic measurements might be affected by transport of the analyte to the functionalized surface, precise quantification of the flow rate during acquisition is required to assess whether the characterization is performed in reaction-limited regime. By adding tracer particles to the sample solution, correlation analysis can provide characterization of flow velocity

in situ by measuring the correlation time of the particles in the embedded microfluidic channel.

Finally, proof-of-principle detection of large biomolecular complexes has been presented in the thesis to evaluate the prospects for label-free biochemical interaction studies involving large macromolecular machines and small organelles.

As an example of application, SMRs with 1 Hz/fg mass responsivity should be able to detect ribosome complexes and ribosome subunits at sub-micromolar concentration. This would enable the monitoring of the binding of the ribosome subunits and of the pre-initiation complexes by detecting the mass variations of the complexes in solution. To this end, first proof-of-principle measurements of ribosomes have been presented. However, interactions of the ribosomes with the channel walls currently preclude reliable mass characterization of these complexes. Further investigation is required to overcome such limitation, for example by testing passivation strategies of the channel walls for reducing sample interaction.

To enable detection of reactions in the millisecond/second regime, modifications of the microfluidic platform are required. Currently, the time resolution of kinetic measurements by MCS is limited by the acquisition time of the mass-trace. Integration of the SMRs with continuous flow mixers would improve the temporal resolution of the analysis by decoupling the acquisition time required for the measurement and the time points of the reaction detected by MCS. In continuous flow mixers, the reaction is initiated by the mixing of two or more flowing solutions and the mixture is analyzed at later positions in the channel corresponding to different time points of the kinetics. Using this approach, the temporal resolution of the MCS measurements would ultimately be limited by the time spent by the particles in the resonator, usually in the order of a few tens of milliseconds. The combination of fast microfluidic mixers and the high mass sensitivity obtained with correlation analysis would enable label-free detection of the early phases of biomolecular interactions by looking at mass variations of the complexes in solution. Possible examples of application are the detection of the first oligomeric species at the onset of protein aggregation, or the characterization of transient ribosome complexes during protein synthesis.

Appendices

Appendix A

Computer scripts

Matlab scripts

Each measurement generates two files:

- frequency trace: continuous monitoring of the resonance frequency. Sampling frequency is set by the difference between the device resonance frequency and the reference frequency (see Sec. 2.3)
- measurement intervals: file containing the temporal informations of when the sample solution was in the resonator embedded channel.

The measurement traces are then analyzed as follows:

1. Import data
2. Calibration
3. Fit correlation
4. Calculate mass

To detect particle size, multiple measurements at different flow velocities are required. Steps 1 and 2 of the amplitude analysis are performed on each measurement trace. The subsequent steps are:

1. Prepare pseudo-curves
2. Fit pseudo-curves
3. Estimate size

The main scripts used for the analysis are reported here, written in MATLAB pseudo-code.

MATLAB functions

Import data

Requires: measurement files

```

Load coefficients of low pass filter lpf_filter
Import frequency trace in freq_raw %Raw values of resonance frequency
Fs=mean(freq_raw); %Sampling frequency
time_meas=convert_to_ms(freq_raw); %From frequency to measurement time
extremes=Import measurement intervals %Import file with temporal extremes of when sample was
in the resonator
freq_lpf=filter(lpf_filter, 1, freq_raw); %Low pass filter the measurement trace
freq_hpf=freq_raw - freq_lpf; %Removes slow varying noise terms and baseline drifts. Take only
frequency fluctuations

%Prepare signal for correlation analysis: remove visible particles in the trace
t_approx=find_approx(freq_hpf, Fs); %Find approximate residence time of the particles in the
resonator
(reference, sample, small)=separate(freq_raw, freq_hpf, t_approx, Fs); %reference: only
reference particle signatures; sample no visible particle signature; small small visible particle sig-
natures

%Separate the measurement intervals
for i=1:N %N number of intervals
    interval{i}.freq_raw=freq_raw(extremes(i,1):extremes(i,2));
    interval{i}.freq_hpf=freq_hpf(extremes(i,1):extremes(i,2));
    interval{i}.sample=sample(extremes(i,1):extremes(i,2));
end

```

Calibration

Requires: interval, t_approx Fs

Returns: responsivity, interval

```

npoints=t_approx*Fs; %Average number of points of reference signature
for i=1:length(interval)
    ref_sgolay=sgolayfilt(reference, 3, npoints/10); %Apply a Savitzky-Golay filter of the third
order to find the maximum frequency shift
    locations, shifts=findpeaks(-ref_sgolay, thres_value, 2npoints); %Find locations and
induced frequency shifts of reference particles by detecting peaks higher than thres_value in
ref_sgolay. The minimum peak distance is twice npoints

%Frequency/mass response
ref_buoyant= $\frac{1}{6}\pi d_{ref}^3(\rho_{ref} - \rho_{buff})$ ; %Buoyant mass of reference. d_ref diameter of ref par-
ticle
ref_shift=mean(shifts); %Induced frequency shift by reference
responsivity=ref_shift/ref_buoyant

%Find average time spent by the fluid in the resonator
Rref=xcorr(reference, 2*npoints, 'unbiased'); %Calculate autocorrelation of reference par-
ticle signatures
interval{i}.t_mean=fitXcorrRef(Rref, d_ref, Fs); %Fit autocorrelation of reference particles
knowing the particle diameter. Flow velocity can be estimated from the correlation shape
end
return responsivity, t_mean

```

Fit correlation curve

Requires: interval, Fs

Returns: Beta1 for all intervals

```
for i=1:length(interval) %If all t_mean have similar values, concatenate all interval{i}.sample
to increase signal-to-noise ratio
    nr_lags=interval{i}.t_mean*Fs*1.5; %Number of points for autocorrelation calculation
    Rsample=xcorr(interval{i}.sample, nr_lags, 'unbiased'); %Calc. autocorrelation
    Rsample=Rsample(nr_lags+3: end); %Take one sided autocorrelation and remove 2 points of
max noise
    time_axis=(3:nr_lags)/Fs;
    beta0=[a interval{i}.t_mean]; %Starting point for the fit
    mdl=nonlinearmodel.fit(time_axis, Rsample, autocorr_curve, beta0); %Non linear fitting: au-
tocorr_curve is the compartment autocorrelation model
    %Amplitude value and standard deviation
end
return Beta1
```

Calculate mass

Requires: interval{i}.Beta1, responsivity, ρ_p , ρ_b , c0 or T % ρ_p particle density, ρ_b buffer density, c0 particle concentration, T solid content

Returns: Δm_p , m_p

```
for i=1:length(interval) %If all t_mean have similar values, analyze all intervals together
    %Calculate average induced freq. shift
    if c0 is known then
         $\Delta f_p = \sqrt{\frac{5\text{Beta1}}{c0V}}$ ; %Average frequency shift, V channel volume
    else T is known
        TotT=T*Chann.Volume; %Mass in the channel
        TotF=TotT*(1 -  $\rho_b/\rho_p$ )*responsivity; %Mass in the channel, converted in freq.
         $\Delta f_p = 5V \text{Beta1}/\text{TotF}$ ; %Average frequency shift
    end if
    Returns:  $\Delta m_p$ ,  $m_p$ 
     $\Delta m_p = \Delta f_p/\text{responsivity}$ ; %Average buoyant mass
    if  $\rho_p$  and  $\rho_b$  are known then %Calculate mass of the particle
         $m_p = \Delta m_p / (1 - \rho_b/\rho_p)$ ; %Dry mass of the particle
    end if
end
return  $\Delta m_p$ ,  $m_p$ 
```

Prepare pseudo-curves

Requires: data %Data is a structure with all measurements recorded for one sample

Returns: Rsamples, T %Rsamples contains all generated correlation curves, T the time axis

```
npoints=0; %Total nr of points in the fit curve
for i=1:length(data) data{i}.n_points=data{i}.Fs*data{i}.t_mean*1.5; n_points=n_points+data{i}.n.poi-
2; %Remove points of maximum noise
end
Rsamples=zeros(n_points, 500); %Initialize variables for all generated autocorrelations
start=1;
for i=1:length(data)
    finish=start+data{i}.n_points-3;
```

```

for j=1:500
    temp=[];
    while (length(temp)<length(data{i}.sample)) %Generate pseudo-trace
        temp=[temp random(data{i}.sample)]; %function random takes a block from the trace
sample. The block is concatenated to temp
    end
    Rsample=xcorr(trace, data{i}.n_points, 'unbiased'); %Autocorrelation pseudo-trace;
    Rsample=Rsample(vardata{i}.n_points+3:end); %One sided correlation curve
    Rsamples(start:varfinish, j)=Rsample;
end
T(start:finish, :)=i, (3:vardata{i}.n_points)/Fs; %T contains an index column and the time
axis of the correlation
start=finish+1;
end
return Rsamples T

```

Estimate size

Requires: Rsamples, T, data

Returns: size

```

n=number of flow rate measured
d_test=linspace(..., ...) %Test diameters for particle size identification
ampl=zeros(length(d_test), n*length(Rsample(:,1)));
err=zeros(length(d_test), length(Rsample(:,1)));
for i=1:length(d_test) %For all test diameters
    ampl_temp & err_temp = zeros(n, length(Rsample(:,1)))
    for j=1:n %For all flow rates
        int= points of the correlation recorded at the j-th flow rate
        Rtest=generate_rtest(T, data.t_mean, d_test(i)) %Generates a normalized autocorrelation
with time axis T, average time in the resonator t_mean and particle size d_test(i)
        [ampl_temp(j, :)] = Rsamples(int, :) \ Rtest; %Least-square fit of all the pseudo-curves at
j-th flow rate
        [err_temp(j, :)] = (Rsamples(int, :) - ampl_temp * Rtest).^2; % (Residuals)
    end
    err(i, :) = sum(err_temp); %Save residuals for the i-th test diameter
    ampl(i, :) = mean(ampl_temp); %Take the mean amplitude value per each test curve
end
d_splines=linspace(d_test(1), d_test(end), 200) %Refine the d_test
ps=spline(d_test, err', d_splines); %Fit the residuals with a spline to find particle size that
minimizes the residual for each pseudo-curve
[temp, best]=min(ps, [], 2); %Find minimum residual per each pseudo-curve according to the spline
fitting
sizes=d_splines(best);
delta_size=std(sizes); %Uncertainty size
size=mean(sizes); %Particle size

ampl_xcorr=zeros(length(res), 1);
for i=1:length(res)
    ampl_xcorr(i)=ampl(i, res(i)); %Amplitude of the best fit curve
end
delta_ampl=std(ampl_xcorr); %Uncertainty size
ampl_xcorr(i)=mean(ampl_xcorr(i)); %Curve amplitude, best fit paramters
%From ampl_xcorr the buoyant mass of the particle can be calculated

```

Appendix B

List of scientific contributions

Part of this thesis have been published as follows:

Mario M. Modena, Yu Wang, Dietmar Riedel, and Thomas P. Burg. Resolution enhancement of suspended microchannel resonators for weighing of biomolecular complexes in solution. *Lab on a Chip*, vol. 14, pp. 342–350, 2014.

Yu Wang, **Mario M. Modena**, Mitja Platen, Iwan A. T. Schaap, and Thomas P. Burg. Label-Free Measurement of Amyloid Elongation by Suspended Microchannel Resonators. *Analytical Chemistry*, vol. 87, pp. 1821–1828, 2015.

Published after the submission of the thesis

Mario M. Modena and Thomas P. Burg. Mass correlation spectroscopy for mass- and size-based nanoparticle characterization in fluid. *Journal of Applied Physics*, 118(22):224901, 2015.

Bibliography

- [1] John C. H. Spence. *High-Resolution Electron Microscopy*. Oxford University Press, 2008.
- [2] Scott E. McNeil. Size Measurement of Nanoparticles Using Atomic Force Microscopy, in *Characterization of Nanoparticles Intended for Drug Delivery*. Number 697 in Methods in Molecular Biology. Humana Press, 2011.
- [3] Travis J. Gould, Samuel T. Hess, and Joerg Bewersdorf. Optical Nanoscopy: From Acquisition to Analysis. *Annual Review of Biomedical Engineering*, 14(1):231–254, 2012.
- [4] Tae-Hee Lee, Lisa J. Lapidus, Wei Zhao, Kevin J. Travers, Daniel Herschlag, and Steven Chu. Measuring the Folding Transition Time of Single RNA Molecules. *Biophysical Journal*, 92(9):3275–3283, 2007.
- [5] Pohl Milón, Cristina Maracci, Liudmila Filonava, Claudio O. Gualerzi, and Marina V. Rodnina. Real-time assembly landscape of bacterial 30s translation initiation complex. *Nature Structural & Molecular Biology*, 19(6):609–615, 2012.
- [6] Kerstin Weiß, Andreas Neef, Qui Van, Stefanie Kramer, Ingo Gregor, and Jörg Enderlein. Quantifying the Diffusion of Membrane Proteins and Peptides in Black Lipid Membranes with 2-Focus Fluorescence Correlation Spectroscopy. *Biophysical Journal*, 105(2):455–462, 2013.
- [7] Ingemar Lundström. Real-time biospecific interaction analysis. *Biosensors and Bioelectronics*, 9(9–10):725–736, 1994.
- [8] Voula Kodoyianni. Label-free analysis of biomolecular interactions using SPR imaging. *BioTechniques*, 50(1):32–40, 2011.
- [9] Cathy I. Cheng, Yi-Pin Chang, and Yen-Ho Chu. Biomolecular interactions and tools for their recognition: focus on the quartz crystal microbalance and

- its diverse surface chemistries and applications. *Chemical Society Reviews*, 41(5):1947–1971, 2012.
- [10] R. Pecora. *Dynamic Light Scattering: Applications of Photon Correlation Spectroscopy*. Springer Science & Business Media, 1985.
- [11] Erinc Sahin and Christopher J. Roberts. Size-Exclusion Chromatography with Multi-angle Light Scattering for Elucidating Protein Aggregation Mechanisms. In Vladimir Voynov and Justin A. Caravella, editors, *Therapeutic Proteins*, volume 899 of *Methods in Molecular Biology*, pages 403–423. Humana Press, 2012.
- [12] Philip J. Wyatt. Measurement of Special Nanoparticle Structures by Light Scattering. *Analytical Chemistry*, 2014.
- [13] Atta Ahmad, Vladimir N. Uversky, Dongpyo Hong, and Anthony L. Fink. Early Events in the Fibrillation of Monomeric Insulin. *Journal of Biological Chemistry*, 280(52):42669–42675, 2005.
- [14] Thomas P. Burg, Michel Godin, Scott M. Knudsen, Wenjiang Shen, Greg Carlson, John S. Foster, Ken Babcock, and Scott R. Manalis. Weighing of biomolecules, single cells and single nanoparticles in fluid. *Nature*, 446(7139):1066–1069, 2007.
- [15] Robert A. Barton, B. Ilic, Scott S. Verbridge, Benjamin R. Cipriany, Jeevak M. Parpia, and Harold G. Craighead. Fabrication of a Nanomechanical Mass Sensor Containing a Nanofluidic Channel. *Nano Letters*, 10(6):2058–2063, 2010.
- [16] Jungchul Lee, Wenjiang Shen, Kris Payer, Thomas P. Burg, and Scott R. Manalis. Toward Attogram Mass Measurements in Solution with Suspended Nanochannel Resonators. *Nano Letters*, 10(7):2537–2542, 2010.
- [17] P.S. Waggoner, C.P. Tan, and H.G. Craighead. Microfluidic integration of nanomechanical resonators for protein analysis in serum. *Sensors and Actuators B: Chemical*, 150(2):550–555, 2010.
- [18] Yu Wang, Mario Matteo Modena, Mitja Platen, Iwan Alexander Taco Schaap, and Thomas Peter Burg. Label-Free Measurement of Amyloid Elongation by Suspended Microchannel Resonators. *Analytical Chemistry*, 87(3):1821–1828, 2015.
- [19] Mario M. Modena, Yu Wang, Dietmar Riedel, and Thomas P. Burg. Resolution enhancement of suspended microchannel resonators for weighing of biomolecular

- complexes in solution. *Lab on a Chip*, 14(2):342–350, 2014.
- [20] Selim Olcum, Nathan Cermak, Steven C. Wasserman, Kathleen S. Christine, Hiroshi Atsumi, Kris R. Payer, Wenjiang Shen, Jungchul Lee, Angela M. Belcher, Sangeeta N. Bhatia, and Scott R. Manalis. Weighing nanoparticles in solution at the attogram scale. *Proceedings of the National Academy of Sciences*, page 201318602, 2014.
- [21] Mario M. Modena and Thomas P. Burg. Mass correlation spectroscopy for mass- and size-based nanoparticle characterization in fluid. *Journal of Applied Physics*, 118(22):224901, 2015.
- [22] Michel Godin, Francisco Feijó Delgado, Sungmin Son, William H. Grover, Andrea K. Bryan, Amit Tzur, Paul Jorgensen, Kris Payer, Alan D. Grossman, Marc W. Kirschner, and Scott R. Manalis. Using buoyant mass to measure the growth of single cells. *Nature Methods*, 7(5):387–390, 2010.
- [23] Sungmin Son, Amit Tzur, Yaochung Weng, Paul Jorgensen, Jisoo Kim, Marc W. Kirschner, and Scott R. Manalis. Direct observation of mammalian cell growth and size regulation. *Nature Methods*, 2012.
- [24] Andrea K. Bryan, Vivian C. Hecht, Wenjiang Shen, Kristofor Payer, William H. Grover, and Scott R. Manalis. Measuring single cell mass, volume, and density with dual suspended microchannel resonators. *Lab on a Chip*, 2013.
- [25] E. V. Orlova and H. R. Saibil. Structural Analysis of Macromolecular Assemblies by Electron Microscopy. *Chemical Reviews*, 111(12):7710–7748, 2011.
- [26] Henk G. Merkus. *Particle Size Measurements*, volume 17 of *Particle Technology Series*. Springer Netherlands, Dordrecht, 2009.
- [27] Will Anderson, Darby Kozak, Victoria A. Coleman, Åsa K. Jämting, and Matt Trau. A comparative study of submicron particle sizing platforms: Accuracy, precision and resolution analysis of polydisperse particle size distributions. *Journal of Colloid and Interface Science*, 405:322–330, 2013.
- [28] Jun Liu, James D. Andya, and Steven J. Shire. A critical review of analytical ultracentrifugation and field flow fractionation methods for measuring protein aggregation. *The AAPS Journal*, 8(3):E580–E589, 2006.
- [29] Thomas M. Laue. Analytical Ultracentrifugation. In *Current Protocols in Protein Science*. John Wiley & Sons, Inc., 2001.

- [30] Peter Schuck. Analytical ultracentrifugation as a tool for studying protein interactions. *Biophysical Reviews*, 5(2):159–171, 2013.
- [31] Huaying Zhao, Chad A. Brautigam, Rodolfo Ghirlando, and Peter Schuck. Overview of Current Methods in Sedimentation Velocity and Sedimentation Equilibrium Analytical Ultracentrifugation. In *Current Protocols in Protein Science*. John Wiley & Sons, Inc., 2013.
- [32] Characterizing polymers: Techniques for the measurement of molecular weight, molecular size and branching. Online <http://www.malvern.com/en/pdf/secure/WP150420PolymerCharacterization.pdf>, Accessed on 15-05-2015.
- [33] Philip J. Wyatt. Light scattering and the absolute characterization of macromolecules. *Analytica Chimica Acta*, 272(1):1–40, 1993.
- [34] Tapan K. Das. Protein Particulate Detection Issues in Biotherapeutics Development—Current Status. *AAPS PharmSciTech*, 13(2):732–746, 2012.
- [35] Dennis E. Koppel. Analysis of Macromolecular Polydispersity in Intensity Correlation Spectroscopy: The Method of Cumulants. *The Journal of Chemical Physics*, 57(11):4814–4820, 1972.
- [36] Stephen W. Provencher. A constrained regularization method for inverting data represented by linear algebraic or integral equations. *Computer Physics Communications*, 27(3):213–227, 1982.
- [37] Stephen W. Provencher. CONTIN: A general purpose constrained regularization program for inverting noisy linear algebraic and integral equations. *Computer Physics Communications*, 27(3):229–242, 1982.
- [38] Ian D. Morrison, E. F. Grabowski, and C. A. Herb. Improved techniques for particle size determination by quasi-elastic light scattering. *Langmuir*, 1(4):496–501, 1985.
- [39] Claudia Veigel and Christoph F. Schmidt. Moving into the cell: single-molecule studies of molecular motors in complex environments. *Nature Reviews Molecular Cell Biology*, 12(3):163–176, 2011.
- [40] Irena L. Ivanovska, Roberto Miranda, Jose L. Carrascosa, Gijs J. L. Wuite, and Christoph F. Schmidt. Discrete fracture patterns of virus shells reveal mechanical

- building blocks. *Proceedings of the National Academy of Sciences*, 108(31):12611–12616, 2011.
- [41] Reid C. Van Lehn, Maria Ricci, Paulo H. J. Silva, Patrizia Androozzi, Javier Reguera, Kislun Voitchovsky, Francesco Stellacci, and Alfredo Alexander-Katz. Lipid tail protrusions mediate the insertion of nanoparticles into model cell membranes. *Nature Communications*, 5, 2014.
- [42] Elliot L. Elson and Douglas Magde. Fluorescence correlation spectroscopy. I. Conceptual basis and theory. *Biopolymers*, 13(1):1–27, 1974.
- [43] R. Rigler, Ü Mets, J. Widengren, and P. Kask. Fluorescence correlation spectroscopy with high count rate and low background: analysis of translational diffusion. *European Biophysics Journal*, 22(3):169–175, 1993.
- [44] K M Berland, P T So, and E Gratton. Two-photon fluorescence correlation spectroscopy: method and application to the intracellular environment. *Biophysical Journal*, 68(2):694–701, 1995.
- [45] Kirsten Bacia, Dag Scherfeld, Nicoletta Kahya, and Petra Schwille. Fluorescence Correlation Spectroscopy Relates Rafts in Model and Native Membranes. *Biophysical Journal*, 87(2):1034–1043, 2004.
- [46] Sally A. Kim, Katrin G. Heinze, and Petra Schwille. Fluorescence correlation spectroscopy in living cells. *Nature Methods*, 4(11):963–973, 2007.
- [47] Katrin G. Heinze, Michael Jahnz, and Petra Schwille. Triple-Color Coincidence Analysis: One Step Further in Following Higher Order Molecular Complex Formation. *Biophysical Journal*, 86(1):506–516, 2004.
- [48] H Qian, M P Sheetz, and E L Elson. Single particle tracking. Analysis of diffusion and flow in two-dimensional systems. *Biophysical Journal*, 60(4):910–921, 1991.
- [49] Vasco Filipe, Andrea Hawe, and Wim Jiskoot. Critical Evaluation of Nanoparticle Tracking Analysis (NTA) by NanoSight for the Measurement of Nanoparticles and Protein Aggregates. *Pharmaceutical Research*, 27(5):796–810, 2010.
- [50] Stephen J. Sowerby, Murray F. Broom, and George B. Petersen. Dynamically resizable nanometre-scale apertures for molecular sensing. *Sensors and Actuators B: Chemical*, 123(1):325–330, 2007.
- [51] G. R. Willmott and P. W. Moore. Reversible mechanical actuation of elastomeric nanopores. *Nanotechnology*, 19(47):475504, 2008.

- [52] Eva Weatherall and Geoff R. Willmott. Applications of tunable resistive pulse sensing. *Analyst*, 2015.
- [53] Darby Kozak, Will Anderson, Robert Vogel, Shaun Chen, Fiach Antaw, and Matt Trau. Simultaneous Size and ζ -Potential Measurements of Individual Nanoparticles in Dispersion Using Size-Tunable Pore Sensors. *ACS Nano*, 6(8):6990–6997, 2012.
- [54] Szabolcs Fekete, Alain Beck, Jean-Luc Veuthey, and Davy Guillarme. Theory and practice of size exclusion chromatography for the analysis of protein aggregates. *Journal of Pharmaceutical and Biomedical Analysis*, 101:161–173, 2014.
- [55] Paula Hong, Stephan Koza, and Edouard S. P. Bouvier. Size-Exclusion Chromatography for the Analysis of Protein Biotherapeutics and their Aggregates. *Journal of Liquid Chromatography & Related Technologies*, 35(20):2923–2950, 2012.
- [56] Wanda K. Hartmann, Nirmala Saptharishi, Xiao Yi Yang, Gautam Mitra, and Gopalan Soman. Characterization and analysis of thermal denaturation of antibodies by size exclusion high-performance liquid chromatography with quadruple detection. *Analytical Biochemistry*, 325(2):227–239, 2004.
- [57] Alexander W. Bell, Tommy Nilsson, Robert E. Kearney, and John J. M. Bergeron. The protein microscope: incorporating mass spectrometry into cell biology. *Nature Methods*, 4(10):783–784, 2007.
- [58] John R. Yates, Cristian I. Ruse, and Aleksey Nakorchevsky. Proteomics by Mass Spectrometry: Approaches, Advances, and Applications. *Annual Review of Biomedical Engineering*, 11(1):49–79, 2009.
- [59] Adam R. McKay, Brandon T. Ruotolo, Leopold L. Ilag, and Carol V. Robinson. Mass Measurements of Increased Accuracy Resolve Heterogeneous Populations of Intact Ribosomes. *Journal of the American Chemical Society*, 128(35):11433–11442, 2006.
- [60] Joost Snijder, Rebecca J. Rose, David Veessler, John E. Johnson, and Albert J. R. Heck. Studying 18 mda virus assemblies with native mass spectrometry. *Angewandte Chemie International Edition*, 52(14):4020–4023, 2013.
- [61] Philip Lössl, Joost Snijder, and Albert J. R. Heck. Boundaries of Mass Resolution in Native Mass Spectrometry. *Journal of The American Society for Mass*

- Spectrometry*, 25(6):906–917, 2014.
- [62] Antonio R. Montoro Bustos, Jorge Ruiz Encinar, and Alfredo Sanz-Medel. Mass spectrometry for the characterisation of nanoparticles. *Analytical and Bioanalytical Chemistry*, 405(17):5637–5643, 2013.
- [63] Y. T. Yang, C. Callegari, X. L. Feng, K. L. Ekinici, and M. L. Roukes. Zeptogram-Scale Nanomechanical Mass Sensing. *Nano Letters*, 6(4):583–586, 2006.
- [64] M. S. Hanay, S. Kelber, A. K. Naik, D. Chi, S. Hentz, E. C. Bullard, E. Colinet, L. Duraffourg, and M. L. Roukes. Single-protein nanomechanical mass spectrometry in real time. *Nature Nanotechnology*, 7(9):602–608, 2012.
- [65] J. Chaste, A. Eichler, J. Moser, G. Ceballos, R. Rurali, and A. Bachtold. A nanomechanical mass sensor with yoctogram resolution. *Nature Nanotechnology*, 7(5):301–304, 2012.
- [66] K. L. Ekinici, Y. T. Yang, and M. L. Roukes. Ultimate limits to inertial mass sensing based upon nanoelectromechanical systems. *Journal of Applied Physics*, 95(5):2682–2689, 2004.
- [67] T. S. Biswas, A. Suhel, B. D. Hauer, A. Palomino, K. S. D. Beach, and J. P. Davis. High-Q gold and silicon nitride bilayer nanostrings. *Applied Physics Letters*, 101(9):093105–093105–5, 2012.
- [68] T.P. Burg, A.R. Mirza, N. Milovic, C.H. Tsau, G.A. Popescu, J.S. Foster, and S.R. Manalis. Vacuum-Packaged Suspended Microchannel Resonant Mass Sensor for Biomolecular Detection. *Journal of Microelectromechanical Systems*, 15(6):1466–1476, 2006.
- [69] Thomas P. Burg. *Suspended microchannel resonators for biomolecular detection*. Ph.d. thesis, Massachusetts Institute of Technology, Dept. of Electrical Engineering and Computer Science, 2005.
- [70] Thomas P. Burg, John E. Sader, and Scott R. Manalis. Nonmonotonic Energy Dissipation in Microfluidic Resonators. *Physical Review Letters*, 102(22):228103, 2009.
- [71] J. L. Arlett and M. L. Roukes. Ultimate and practical limits of fluid-based mass detection with suspended microchannel resonators. *Journal of Applied Physics*, 108(8):084701–084701–11, 2010.

- [72] S. Dohn, W. Svendsen, A. Boisen, and O. Hansen. Mass and position determination of attached particles on cantilever based mass sensors. *Review of Scientific Instruments*, 78(10):103303–103303–3, 2007.
- [73] Jungchul Lee, Andrea K. Bryan, and Scott R. Manalis. High precision particle mass sensing using microchannel resonators in the second vibration mode. *Review of Scientific Instruments*, 82(2):023704–023704–4, 2011.
- [74] William H. Grover, Andrea K. Bryan, Monica Diez-Silva, Subra Suresh, John M. Higgins, and Scott R. Manalis. Measuring single-cell density. *Proceedings of the National Academy of Sciences*, 2011.
- [75] Alan V. Oppenheim, Ronald W. Schaffer, and John R. Buck. *Discrete-time Signal Processing (2Nd Ed.)*. Prentice-Hall, Inc., Upper Saddle River, NJ, USA, 1999.
- [76] M.R. Doshi, P.M. Daiya, and W.N. Gill. Three dimensional laminar dispersion in open and closed rectangular conduits. *Chemical Engineering Science*, 33(7):795–804, 1978.
- [77] Scott C. James and Constantinos V. Chrysikopoulos. Effective velocity and effective dispersion coefficient for finite-sized particles flowing in a uniform fracture. *Journal of Colloid and Interface Science*, 263(1):288–295, 2003.
- [78] Heena Khatter, Alexander G. Myasnikov, Leslie Mastio, Isabelle M. L. Billas, Catherine Birck, Stefano Stella, and Bruno P. Klaholz. Purification, characterization and crystallization of the human 80s ribosome. *Nucleic Acids Research*, 2014.
- [79] Geoffrey Taylor. Dispersion of Soluble Matter in Solvent Flowing Slowly through a Tube. *Proceedings of the Royal Society of London. Series A. Mathematical and Physical Sciences*, 219(1137):186–203, 1953.
- [80] R. Aris. On the Dispersion of a Solute in a Fluid Flowing through a Tube. *Proceedings of the Royal Society of London. Series A. Mathematical and Physical Sciences*, 235(1200):67–77, 1956.
- [81] M. S. Bello, R. Rezzonico, and P. G. Righetti. Use of Taylor-Aris dispersion for measurement of a solute diffusion coefficient in thin capillaries. *Science (New York, N.Y.)*, 266(5186):773–776, 1994.
- [82] K. Ekambara and J. B. Joshi. Axial mixing in laminar pipe flows. *Chemical Engineering Science*, 59(18):3929–3944, 2004.

- [83] Octave Levenspiel. *Tracer Technology: Modeling the Flow of Fluids*. Springer, 2011.
- [84] Debashis Dutta, Arun Ramachandran, and David T. Leighton Jr. Effect of channel geometry on solute dispersion in pressure-driven microfluidic systems. *Microfluidics and Nanofluidics*, 2(4):275–290, 2006.
- [85] Ivan C. Christov and Howard A. Stone. Shear dispersion in dense granular flows. *Granular Matter*, 16(4):509–515, 2014.
- [86] Shimon Haber and Roberto Mauri. Lagrangian approach to time-dependent laminar dispersion in rectangular conduits. Part 1. Two-dimensional flows. *Journal of Fluid Mechanics*, 190:201–215, 1988.
- [87] Bradley Efron and Robert J. Tibshirani. *An Introduction to the Bootstrap*. Chapman & Hall, 1994.
- [88] Dimitris N. Politis and Joseph P. Romano. The Stationary Bootstrap. *Journal of the American Statistical Association*, 89(428):1303–1313, 1994.
- [89] Wyatt Technology Corporation. DYNAMICS User’s guide, M1400 Rev. I, 2010.
- [90] Fabrizio Chiti and Christopher M. Dobson. Protein Misfolding, Functional Amyloid, and Human Disease. *Annual Review of Biochemistry*, 75(1):333–366, 2006.
- [91] Fabrizio Chiti and Christopher M. Dobson. Amyloid formation by globular proteins under native conditions. *Nature Chemical Biology*, 5(1):15–22, 2009.
- [92] Christopher M. Dobson. Protein folding and misfolding. *Nature*, 426(6968):884–890, 2003.
- [93] Thomas R. Jahn and Sheena E. Radford. Folding versus aggregation: Polypeptide conformations on competing pathways. *Archives of Biochemistry and Biophysics*, 469(1):100 – 117, 2008. Highlight Issue: Protein Folding.
- [94] Aimee M. Morris, Murielle A. Watzky, and Richard G. Finke. Protein aggregation kinetics, mechanism, and curve-fitting: A review of the literature. *Biochimica et Biophysica Acta (BBA) - Proteins & Proteomics*, 1794(3):375–397, 2009.
- [95] Vladimir N. Uversky, Christopher J. Oldfield, and A. Keith Dunker. Intrinsically disordered proteins in human diseases: Introducing the d2 concept. *Annual Review of Biophysics*, 37(1):215–246, 2008. PMID: 18573080.
- [96] Jean L Whittingham, David J Scott, Karen Chance, Ashley Wilson, John Finch, Jens Brange, and G Guy Dodson. Insulin at pH 2: Structural Analysis of the

- Conditions Promoting Insulin Fibre Formation. *Journal of Molecular Biology*, 318(2):479–490, 2002.
- [97] B. Swift, P. N. Hawkins, C. Richards, and R. Gregory. Examination of insulin injection sites: an unexpected finding of localized amyloidosis. *Diabetic Medicine*, 19(10):881–882, 2002.
- [98] Liza Nielsen, Ritu Khurana, Alisa Coats, Sven Frokjaer, Jens Brange, Sandip Vyas, Vladimir N. Uversky, and Anthony L. Fink. Effect of environmental factors on the kinetics of insulin fibril formation: Elucidation of the molecular mechanism. *Biochemistry*, 40(20):6036–6046, 2001. PMID: 11352739.
- [99] Fabio Librizzi and Christian Rischel. The kinetic behavior of insulin fibrillation is determined by heterogeneous nucleation pathways. *Protein Science : A Publication of the Protein Society*, 14(12):3129–3134, 2005.
- [100] Sarah E. Bondos. Methods for Measuring Protein Aggregation. *Current Analytical Chemistry*, 2(2):157–170, 2006.
- [101] Minna Groenning. Binding mode of Thioflavin T and other molecular probes in the context of amyloid fibrils—current status. *Journal of Chemical Biology*, 3(1):1–18, 2010.
- [102] Matthew Biancalana and Shohei Koide. Molecular mechanism of Thioflavin-T binding to amyloid fibrils. *Biochimica et Biophysica Acta (BBA) - Proteins and Proteomics*, 1804(7):1405–1412, 2010.
- [103] Melanie R Nilsson. Techniques to study amyloid fibril formation in vitro. *Methods*, 34(1):151–160, 2004.
- [104] Bente Vestergaard, Minna Groenning, Manfred Roessle, Jette S Kastrup, Marco van de Weert, James M Flink, Sven Frokjaer, Michael Gajhede, and Dmitri I Svergun. A Helical Structural Nucleus Is the Primary Elongating Unit of Insulin Amyloid Fibrils. *PLoS Biology*, 5(5), 2007.
- [105] Hannes Fischer, Igor Polikarpov, and Aldo F. Craievich. Average protein density is a molecular-weight-dependent function. *Protein Science : A Publication of the Protein Society*, 13(10):2825–2828, 2004.
- [106] E J Nettleton, P Tito, M Sunde, M Bouchard, C M Dobson, and C V Robinson. Characterization of the oligomeric states of insulin in self-assembly and amyloid fibril formation by mass spectrometry. *Biophysical journal*, 79(2):1053–1065,

- 2000.
- [107] Brian O’Nuallain, Angela D. Williams, Per Westermark, and Ronald Wetzel. Seeding Specificity in Amyloid Growth Induced by Heterologous Fibrils. *Journal of Biological Chemistry*, 279(17):17490–17499, 2004.
- [108] Eri Chatani, Young-Ho Lee, Hisashi Yagi, Yuichi Yoshimura, Hironobu Naiki, and Yuji Goto. Ultrasonication-dependent production and breakdown lead to minimum-sized amyloid fibrils. *Proceedings of the National Academy of Sciences*, 106(27):11119–11124, 2009.
- [109] Magdalena I. Ivanova, Stuart A. Sievers, Michael R. Sawaya, Joseph S. Wall, and David Eisenberg. Molecular basis for insulin fibril assembly. *Proceedings of the National Academy of Sciences*, 2009.
- [110] Keisuke Nakayama, Katsuaki Tanabe, and Harry A. Atwater. Plasmonic nanoparticle enhanced light absorption in GaAs solar cells. *Applied Physics Letters*, 93(12):121904, 2008.
- [111] Yu A. Akimov, W. S. Koh, S. Y. Sian, and S. Ren. Nanoparticle-enhanced thin film solar cells: Metallic or dielectric nanoparticles? *Applied Physics Letters*, 96(7):073111, 2010.
- [112] Siti M. Janib, Ara S. Moses, and J. Andrew MacKay. Imaging and drug delivery using theranostic nanoparticles. *Advanced Drug Delivery Reviews*, 62(11):1052–1063, 2010.
- [113] P. Couvreur. Nanoparticles in drug delivery: Past, present and future. *Advanced Drug Delivery Reviews*, 65(1):21–23, 2013.
- [114] Josep Villanueva, Kevin Lawlor, Ricardo Toledo-Crow, and Paul Tempst. Automated serum peptide profiling. *Nature Protocols*, 1(2):880–891, 2006.
- [115] Grace Dongqing Chen, Catharina Johanna Alberts, William Rodriguez, and Mehmet Toner. Concentration and purification of HIV-1 virions by microfluidic separation of superparamagnetic nanoparticles. *Analytical chemistry*, 82(2):723, 2010.
- [116] Mohamed F. Elshal and J. Philip McCoy. Multiplex Bead Array Assays: Performance Evaluation and Comparison of Sensitivity to ELISA. *Methods (San Diego, Calif.)*, 38(4):317–323, 2006.
- [117] C. T. Lim and Y. Zhang. Bead-based microfluidic immunoassays: The next

- generation. *Biosensors and Bioelectronics*, 22(7):1197–1204, 2010.
- [118] V. V Krishhan, Imran H. Khan, and Paul A. Luciw. Multiplexed microbead immunoassays by flow cytometry for molecular profiling: Basic concepts and proteomics applications. *Critical Reviews in Biotechnology*, 29(1):29–43, 2009. PMID: 19514901.
- [119] Huiyan Li, Rym Ferial Leulmi, and David Juncker. Hydrogel droplet microarrays with trapped antibody-functionalized beads for multiplexed protein analysis. *Lab on a Chip*, 11(3):528–534, 2011.
- [120] Jie Chou, Jorge Wong, Nicolaos Christodoulides, Pierre N. Floriano, Ximena Sanchez, and John McDevitt. Porous Bead-Based Diagnostic Platforms: Bridging the Gaps in Healthcare. *Sensors (Basel, Switzerland)*, 12(11):15467–15499, 2012.
- [121] Matteo Cornaglia, Raphaël Trouillon, H. Cumhur Tekin, Thomas Lehnert, and Martin A. M. Gijs. Magnetic Particle-Scanning for Ultrasensitive Immunodetection On-Chip. *Analytical Chemistry*, 86(16):8213–8223, 2014.
- [122] Polysciences Inc. Polylink Protein Coupling Kit, Rev. 8, *Technical Data Sheet*, 23/05/2013.
- [123] Scott M. Knudsen, Marcio G. von Muhlen, and Scott R. Manalis. Quantifying Particle Coatings Using High-Precision Mass Measurements. *Analytical Chemistry*, 84(3):1240–1242, 2012.
- [124] M. Reza Nejadnik and Wim Jiskoot. Measurement of the average mass of proteins adsorbed to a nanoparticle by using a suspended microchannel resonator. *Journal of Pharmaceutical Sciences*, 104(2):698–704, 2015.
- [125] Corning assay surfaces: Medium binding (untreated) polystyrene surface. Online http://www.corning.com/lifesciences/us_canada/en/technical_resources/surfaces/assay/medium... Accessed on 24-04-2015.
- [126] P.W. Stevens, M.R. Hansberry, and D.M. Kelso. Assessment of adsorption and adhesion of proteins to polystyrene microwells by sequential enzyme-linked-immunosorbent assay analysis. *Analytical Biochemistry*, 225(2):197 – 205, 1995.
- [127] Joachim Frank, Rajendra K Agrawal, and Adriana Verschoor. Ribosome Structure and Shape. In *eLS*. John Wiley & Sons, Ltd, 2001.

- [128] Thomas Bornemann, Wolf Holtkamp, and Wolfgang Wintermeyer. Interplay between trigger factor and other protein biogenesis factors on the ribosome. *Nature Communications*, 5, 2014.
- [129] Gabriele Fuchs, Alexey N. Petrov, Caleb D. Marceau, Lauren M. Popov, Jin Chen, Seán E. O’Leary, Richard Wang, Jan E. Carette, Peter Sarnow, and Joseph D. Puglisi. Kinetic pathway of 40s ribosomal subunit recruitment to hepatitis c virus internal ribosome entry site. *Proceedings of the National Academy of Sciences*, 112(2):319–325, 2015.
- [130] Alexandros D. Petropoulos, Ekaterini C. Kouvela, Agata L. Starosta, Daniel N. Wilson, George P. Dinos, and Dimitrios L. Kalpaxis. Time-resolved binding of azithromycin to escherichia coli ribosomes. *Journal of Molecular Biology*, 385(4):1179–1192, 2009.
- [131] Anne E. Bunner, Andrea H. Beck, and James R. Williamson. Kinetic cooperativity in escherichia coli 30s ribosomal subunit reconstitution reveals additional complexity in the assembly landscape. *Proceedings of the National Academy of Sciences*, 107(12):5417–5422, 2010.
- [132] Anne E. Bunner, Stefan Nord, P. Mikael Wikström, and James R. Williamson. The effect of ribosome assembly cofactors on in vitro 30s subunit reconstitution. *Journal of Molecular Biology*, 398(1):1–7, 2010.
- [133] H G Wittmann. Components of bacterial ribosomes. *Annual Review of Biochemistry*, 51(1):155–183, 1982.
- [134] Tatsuya Yamamoto, Shunsuke Izumi, and Kunihiko Gekko. Mass spectrometry of hydrogen/deuterium exchange in 70s ribosomal proteins from e. coli. *FEBS Letters*, 580(15):3638–3642, 2006.
- [135] Jun Zhu, Pawel A. Penczek, Rasmus Schröder, and Joachim Frank. Three-dimensional reconstruction with contrast transfer function correction from energy-filtered cryoelectron micrographs: Procedure and application to the 70sescherichia coliRibosome. *Journal of Structural Biology*, 118(3):197–219, 2010.
- [136] Yu Wang. *Label-Free Measurements of Amyloid Formation by Suspended Microchannel Resonators*. Ph.d. thesis, Göttingen University, Faculty of Physics, 2014.

- [137] Tuomas P. J. Knowles, Wenmiao Shu, Glyn L. Devlin, Sarah Meehan, Stefan Auer, Christopher M. Dobson, and Mark E. Welland. Kinetics and thermodynamics of amyloid formation from direct measurements of fluctuations in fibril mass. *Proceedings of the National Academy of Sciences*, 104(24):10016–10021, 2007.
- [138] Jozef Adamcik and Raffaele Mezzenga. Study of amyloid fibrils via atomic force microscopy. *Current Opinion in Colloid & Interface Science*, 17(6):369–376, 2012.
- [139] Thomas Gervais and Klavs F. Jensen. Mass transport and surface reactions in microfluidic systems. *Chemical Engineering Science*, 61(4):1102–1121, 2006.

Mario Matteo Modena

Curriculum Vitæ

Personal Information

Date of birth 16th November 1986
Nationality Italian
Mobile +49 (0)176 86877638
Email mariomatteo.modena@gmail.com

Education

- 2011–2015 **Ph.D. student at the IMPRS - Physics of Biological and Complex Systems,**
Max Planck Institute for Biophysical Chemistry, Göttingen,
Thesis: *Micromechanical Mass Correlation Spectroscopy for the Characterization of Nanoparticles and Biomolecular Complexes in Fluid*
Supervisor: Dr. T. Burg (MPI for Biophysical Chemistry).
- 2008–2010 **Masters of Nanotechnology for Integrated Systems,**
Politecnico di Torino - INP Grenoble - Ecole Fédérale de Lausanne,
Graduation Mark: 110/110 Magna cum Laude
Master Thesis: *Medical Devices for Developing Countries*
Supervisors: Prof. S. Sia (Columbia University) and Prof. M. Cocuzza (Politecnico di Torino).
- 2005–2008 **Bachelor of Physics Engineering,**
Politecnico di Torino,
Graduation Mark: 110/110
Thesis: *Characterization of III-V Lasers for 10 GHz Optical Fiber Communication.*

Professional Experiences

- 2015–Present **Postdoctoral Fellow in the Micro- and Nanotechnologies Laboratory,**
Max Planck Institute for Biophysical Chemistry, Göttingen,
Mass and size characterization of nanoparticles and biomolecular complexes in solution.
- 2010–2011 **Research Assistant in Sia Lab,**
Biomedical Engineering Dept., Columbia University, New York,
Design and Characterization of Point-of-Care Medical Devices for the Detection of Infectious Diseases in Resource-Limited Settings.
- Summer 2009 **Internship at the International Centre for Advanced Materials, KTH, Stockholm,**
Photoluminescence characterization of ZnO defects.

Publications

Micromechanical Mass Correlation Spectroscopy for Nanoparticle Characterization in Fluid
Modena MM and Burg TP, *Journal of Applied Physics*, J. Appl. Phys. 118, 224901, 2015

Label-Free Measurement of Amyloid Elongation by Suspended Microchannel Resonators
Wang Y, **Modena MM**, Platen M, Schaap IAT, Burg TP, *Analytical Chemistry*, vol. 87, pp. 1821-1828, 2015

Resolution Enhancement of Suspended Microchannel Resonators for Weighing of Biomolecular Complexes in Solution

Modena MM, Wang Y, Riedel D, Burg TP, *Lab on a Chip*, vol. 14, pp. 342-350, 2014

Mobile Device for Disease Diagnosis and Data Tracking in Resource-Limited Settings

Chin CD, Cheung YK, Laksanasopin T, **Modena MM et al.**, *Clinical Chemistry*, vol. 59, pp. 629-640, 2013

Conference papers

Mass and Size Characterization of Particles in Solution by Mass Correlation Spectroscopy,
Modena MM, Wang Y, Burg TP, *microTAS 2015*, Gyeongju 2015

Resolution Enhancement of Suspended Microchannel Resonators by Mass Correlation Analysis,
Modena MM, Wang Y, Burg TP, *microTAS 2013*, Freiburg 2013

Mass Correlation Spectroscopy,

Modena MM and Burg TP, *Microfluidics*, EMBL Heidelberg 2012

Skills

Computer skills

- 3D CAD and modeling - Autodesk Inventor, Comsol Multiphysics
- Automation and control -NI Labview
- Data treatment and analysis - MATLAB and Wolfram Mathematica
- Programming - C, C++, AtMega microcontrollers, Arduino
- Analog and digital circuit design - Altium Design, Eagle
- Graphic and word processing - Adobe Illustrator, Photoshop, Microsoft Office, L^AT_EX

Languages

- Italian - Native
- English - Full professional proficiency
- French - Professional working proficiency
- German - Basic

Hobbies and interests

- Italian scout association, from 1994 to 2008
- Volunteer in ambulance service, from 2004 to 2008
- Biking, both on- and off- road
- Analog photography